AIX-MARSEILLE UNIVERSITÉ
ED 352- PHYSIQUE ET SCIENCES DE LA MATIÈRE
CENTRE DE PHYSIQUE THÉORIQUE

Thèse présentée pour obtenir le grade universitaire de docteur

Discipline: Physique Théorique

Claire WAHL

DÉCOHÉRENCE ET INTERACTIONS DANS LES DISPOSITIFS D'OPTIQUE QUANTIQUE ÉLECTRONIQUE

Soutenance le 23/09/2014 devant le jury:

Alberto VERGA	Aix-Marseille Université	Président du jury
Gwendal FÈVE	École Normale Supérieure	Rapporteur
Maura SASSETTI	Universita di Genova	Rapporteur
Thierry MARTIN	Aix-Marseille Université	Directeur de thèse
Jérôme RECH	Centre de Physique Théorique	Invité
Thibaut JONCKHEERE	Centre de Physique Théorique	Invité

Claire WAHL

DECOHERENCE AND INTERACTIONS IN ELECTRON QUANTUM OPTICS SETUPS

Doctoral thesis

Field: Theoretical Physics

September 23, 2014

1st version

Supervisor:
Thierry MARTIN

in close collaboration with:
Jérôme RECH
Thibaut JONCKHEERE

PUBLICATIONS

[1] D. Chevallier, J. Rech, T. Jonckheere, C. Wahl, and T. Martin. Poissonian tunneling through an extended impurity in the quantum Hall effect. *Phys. Rev. B*, 82:155318, 2010.

[2] T. Jonckheere, J. Rech, C. Wahl, and T. Martin. Electron and hole Hong-Ou-Mandel interferometry. *Phys. Rev. B*, 86:125425, 2012.

[3] E. Bocquillon, V. Freulon, F.D. Parmentier, J.-M Berroir, B. Plaçais, C. Wahl, J. Rech, T. Jonckheere, T. Martin, C. Grenier, D. Ferraro, P. Degiovanni, and G. Fève. Electron quantum optics in quantum Hall edge channels. *Annalen der Physik*, 526:1, 2014.

[4] D. Ferraro, C. Wahl, J. Rech, T. Jonckheere, and T. Martin. Electronic hong-ou-mandel interferometry in two-dimensional topological insulators. *Phys. Rev. B*, 89:075407, 2014.

[5] C. Wahl, J. Rech, T. Jonckheere, and T. Martin. Interactions and charge fractionalization in an electronic hong-ou-mandel interferometer. *Phys. Rev. Lett.*, 112:046802, 2014.

CONTENTS

Introduction 1

1 Introduction to electron quantum optics 3
- 1.1 The quantum Hall effect . . . 6
- 1.2 Quantum Point Contact . . . 8
- 1.3 Noise in mesoscopic physics . . . 10
  - 1.3.1 Origin and definition . . . 10
  - 1.3.2 Thermal noise . . . 12
  - 1.3.3 Shot noise . . . 12

I Electronic Hong-Ou-Mandel interferometry in non-interacting quantum Hall regimes 15

2 Electron quantum optics at filling factor $\nu = 1$ 19
- 2.1 Context . . . 19
  - 2.1.1 Single electron source . . . 19
  - 2.1.2 Setups and measurement . . . 24
- 2.2 Theoretical model . . . 28
  - 2.2.1 Outgoing cross-correlations . . . 28
  - 2.2.2 Mixed term . . . 30
  - 2.2.3 Auto-correlations . . . 31
- 2.3 Results . . . 33
  - 2.3.1 Electron-electron collisions . . . 33
  - 2.3.2 Electron-hole collisions . . . 37
  - 2.3.3 Conclusion . . . 41

II Switching on interactions 43

3 Electrons in one dimension 47
- 3.1 Introduction . . . 47
- 3.2 Tomonaga Luttinger liquid theory . . . 49
- 3.3 Bosonization . . . 52
  - 3.3.1 Bosonization identity . . . 52
  - 3.3.2 Kinetic Hamiltonian . . . 54
  - 3.3.3 Interaction Hamiltonian . . . 54
- 3.4 Hydrodynamical Wen model . . . 56
  - 3.4.1 Hydrodynamical approach . . . 56
  - 3.4.2 Quantification . . . 57

4 Theoretical model for filling factor $\nu = 2$ 59
- 4.1 Setups . . . 60
- 4.2 Bosonization framework . . . 61

4.2.1 Definitions . . . 61
4.2.2 Diagonalization . . . 62
4.2.3 In the rotated basis . . . 64
4.3 On a single edge . . . 66
4.3.1 Bosonic Green's functions . . . 66
4.3.2 Normalization . . . 66
4.3.3 Charge density . . . 67
4.3.4 Noise . . . 69
4.4 Hanbury Brown and Twiss experiment . . . 72
4.4.1 Scattering matrix . . . 72
4.4.2 Mixed term . . . 73
4.5 Hong-Ou-Mandel experiment . . . 75
4.6 Conclusion . . . 78

III ELECTRON QUANTUM OPTICS AT FILLING FACTOR $\nu = 2$ 79
5 FINITE TEMPERATURE 83
5.1 Preliminaries . . . 84
5.1.1 Green's functions . . . 84
5.1.2 Normalization . . . 84
5.1.3 Charge fractionalization . . . 85
5.1.4 Incoming noise . . . 88
5.2 Hanbury Brown and Twiss experiment . . . 89
5.3 Hong-Ou-Mandel experiment . . . 93
5.4 Conclusion . . . 100
6 FINITE INTERACTION REGION 103
6.1 Toy model . . . 105
6.2 Preliminaries . . . 108
6.2.1 Intra-channel interactions . . . 108
6.2.2 Green's functions . . . 109
6.2.3 Normalization . . . 110
6.2.4 Charge fractionalization . . . 110
6.2.5 Incoming noise . . . 111
6.3 Hanbury Brown and Twiss experiment . . . 113
6.4 Hong-Ou-Mandel experiment . . . 116
6.5 Conclusion . . . 121
7 ZERO TEMPERATURE 123
7.1 Preliminaries . . . 124
7.1.1 Green's functions . . . 124
7.1.2 Normalization . . . 124
7.1.3 Charge fractionalization . . . 124
7.1.4 Incoming noise . . . 125
7.2 Hanbury Brown and Twiss experiment . . . 127
7.3 Hong-Ou-Mandel experiment . . . 130
7.4 Conclusion . . . 135

CONCLUSION 137
8 OUTLOOK 139

8.1 Summary 140
8.2 Perspectives 144
8.2.1 HOM interferometry in a quantum spin Hall bar 144
8.2.2 Adding interactions 145

IV APPENDIX 147

A CONVERSION FROM OUR SYSTEM OF ARBITRARY UNITS TO REALITY 149
A.1 Conversion 149
A.2 Relation between escape time and energy width 150

BIBLIOGRAPHY 151

LIST OF FIGURES

Figure 1.1 Semi-classical view of the IQHE: electrons move in cyclotrons orbits. These orbits are interrupted on the edges and electrons bounce forward, all in the same direction. Transport is therefore chiral. 6

Figure 1.2 A high magnetic field is applied perpendicular to a 2DEG (purple), reaching the IQHE. Edge states (orange, plain) are formed at the intersection between the Fermi energy (orange, dashed) and the Landau levels (gray). Here, the filling factor is $\nu = 2$: 1 Landau level $\times$ 2 spins (Zeeman splitting is not shown here). 7

Figure 1.3 (Left) Setup 1: the inner channels are fully reflected, and the outer ones are partially transmitted or reflected. (Right) Setup 2: because of the smaller gate voltage, the outer channels are fully transmitted and the inner ones are partially transmitted or reflected. 8

Figure 1.4 Taken from [91]. Conductance of a QPC as a function of gate voltage: it exhibits steps of value $2e^2/h$, corresponding to the progressive transmission of spin-degenerate edge-states. As the magnetic field is increased, the number ν of edge states decreases. For high fields, steps at e^2/h start appearing as the spin-degeneracy of Landau levels is lifted. 9

Figure 1.5 A mesoscopic sample (gray) characterized by its scattering matrix S connects two leads. Each lead is at temperature Θ and at chemical potential $\mu_{L,R}$. Electrons are transported through one channel of conduction, with transmission probability $\mathcal{T}$ and reflexion probability $\mathcal{R}$. 10

Figure 1.6 Taken from [19]. Noise as a function of conductance. It vanishes when the conductance is then a multiple of $2e^2/h$. In dashed, theoretical predictions including thermal noise are plotted. 13

Figure 2.1 Sketch of the mesoscopic capacitor. A time dependent voltage $V_{exc}(t)$ is applied to the metallic top gate (magenta) capacitively coupled to the dot (circular edge state). The strength of the tunnel coupling between the circular and linear edge channels (blue) is controlled by the gate voltage V_g, and thus the QPC transparency $\mathcal{T}$. The current $I(t)$ is measured at the output. 20

Figure 2.2 (Top panel) In the optimal emission regime, the highest occupied level in the dot ϵ is originally at resonance with Fermi energy E_F. A periodic step voltage $V_{exc}(t)$ is then applied, resulting in ϵ varying from $E_F + \Delta/2$ to $E_F - \Delta/2$. (Bottom panel) In the first half period (labeled ②), an electron is emitted, and in the second half period (labeled ③), a hole is emitted. 21

Figure 2.3 (Top panel) Applied step voltage in the resonant emission regime. (Bottom panel) Initially, the Fermi energy is in between two energy levels of the dot (step ①). When applying the excitation voltage, one level of the dot is always at resonance with the Fermi energy (steps ② and ③). Thus, both the electron and hole emissions occur for some part at resonance with E_F. 22

Figure 2.4 Sketch of the experiment. Two indistinguishable particles are partitioned on a splitter. Coincidence counts $\langle N_1 N_2 \rangle$ and number of particles fluctuations $\langle \delta N_1^2 \rangle$ are recorded as a function of the tunable delay δT. Indistinguishable bosons always exit in the same output, which results in the suppression of the coincidence rate (HOM dip) and the doubling of the fluctuations. An opposite behavior is expected for indistinguishable fermions: anti-bunching results in the doubling of the coincidence counts and the suppression of the number of particles fluctuations (Pauli dip). 25

Figure 2.5 The device for electron HOM interferometry. Two chiral edge states meet at a quantum point contact. In each edge state, a single electron source injects an electron when a time-dependent voltage $V(t)$ is applied at the source. Cross-correlations at the two outputs are measured as a function of the time difference between the emitted electrons by each source. 26

Figure 2.6 Taken from [15]. Sketch of the sample based on a SEM picture. The electron gas is represented in blue. Two single electron emitters are located at inputs 1 and 2 of a QPC used as a single electron beam-splitter. Each emitter can be switched on or off, in order to implement either the HBT or the HOM experiment. 27

Figure 2.7 The positions are defined on an axis oriented towards the right. The QPC, whose transparency is tuned by varying the voltage V_{QPC}, is located at $x = 0$. 29
Figure 2.8 HOM dips as a function of the time difference δT (in units of $\hbar/\Delta$), obtained from Floquet scattering matrix formalism in the optimal emission regime (full) and analytical predictions of eq. (2.29) for exponential wave-packets (dot-dashed). Upper panel: symmetric case, with emitter transparencies $\mathcal{T} = 0.2$, 0.5 and 0.8 (from outer to inner curve). Inset: dips for $\mathcal{T} = 0.2$ on two periods of the applied voltage. Lower panel: asymmetric case, with transparencies $\mathcal{T}_1 = 0.2$, $\mathcal{T}_2 = 0.5$ (bottom curve) and $\mathcal{T}_1 = 0.1$, $\mathcal{T}_2 = 0.8$ (top curve). . 36
Figure 2.9 Top panel: HOM peak for electron-hole collision, for a square voltage drive at different level positions. Inset: electron and hole emission process for the two positions of the dot level, with level position parametrized by ϵ with respect to E_F. The curves correspond to $\epsilon = 0.5, 0.4, 0.25$ and 0 (in units of Δ) from the smallest to the largest peak. Bottom panel: same for a sinusoidal voltage drive at different transparencies, $\mathcal{T} = 0.2, 0.5, 0.7$ and 1.0 (smaller to larger peak). $\Theta = 0.1\Delta$ in both panels. 40
Figure 2.10 Taken from [15]. Excess HOM noise, normalized by the HBT noise: $\Delta\bar{q} = S_{HOM}(\tau)/(2S_{HBT})$. The blurry blue line represents the sum of the partition noise of both sources. The blue trace is an exponential fit by $\Delta q = 1 - \gamma e^{-|t-\tau_0|}$. The red trace is obtained using Floquet scattering theory, with an ad hoc fitting parameter. . . 46
Figure 3.1 One-dimensional tight-binding lattice. μ is each site chemical potential, a is the lattice constant and t is the nearest neighbor hopping amplitude. 49
Figure 3.2 Spectrum of the one-dimensional tight-binding model defined by eq. (3.1) with $\mu = E_F$ (plain), and its linearized version near the Fermi energy (dashed). The gray part, corresponding to the negative energy states, is non-physical. 50
Figure 3.3 A quantum Hall fluid droplet. It undergoes deformations which propagate towards one direction. 56
Figure 4.1 The setups: two opposite edge states, each made out of two interacting co-propagating channels, meet at a QPC. (Left) Setup 1: backscattering occurs for outer channels. (Right) Setup 2: backscattering occurs for inner channels. 60

Figure 4.2 Wave-packets envelopes in real space (top) and energy space (bottom). The plain curves are for the packet wide in energy, and the dashed ones for the energy-resolved packet. The energy-resolved packet is injected higher above the FS and is wider in real space. 68

Figure 5.1 Charge density on the outer channel (plain blue at finite temperature, dotted red at zero temperature) and inner channel (dashed blue at finite temperature, dash-dotted red at zero temperature), at the injection time $t = 0$, for wide packets in energy (top panel) and energy resolved packets (bottom panel). The injection position is $l = 5\mu m$. 86

Figure 5.2 Charge density on the outer (bottom panel) and inner (top panel) left moving channels, for energy resolved packets and $u = 0.5v_F$. The injection position is $l = 5\mu m$, and the charge density is imaged after a propagation time $t = 0, 1$ or 2ns. As the modes propagate, they get more and more apart. 87

Figure 5.3 $|S_{HBT}|$ at $\Theta = 0.1K$ as a function of the propagation length l for wave-packets large in energy (top panel) and energy resolved wave-packets (bottom panel), for several interaction strengths. The plain curves stand for setup 1 and the dashed ones setup 2. The noise (in absolute value) rises with the interaction strength, the injection energy and the energy resolution of the wave-packet. In setup 1, it is decreased from its $l = 0$ value to its steady value. In setup 2, the noise rises until it reaches its final value. The length from which the noise is constant decreases with u. 92

Figure 5.4 An electronic wave-packet is injected on both incoming outer channels. (Right insets) Electron density as a function of position for an energy-resolved packet imaged after propagating on a $5\mu m$ length, revealing the presence of two modes composed each of two $\oplus/\ominus$ excitations. (Top) Setup 1: backscattering occurs for the outer channels. (Bottom) Setup 2: backscattering occurs for the inner channels. 94

Figure 5.5 Modulus of S_{HOM} in units of $e^2\mathcal{R}\mathcal{T}$ as a function of the time delay δT, for setup 1 (top panel) and setup 2 (bottom panel), with $u = 0.5v_F$ and $\Theta = 0.1K$, for packets wide in energy. The contrast is quite good and the central dip depth does not depend on the setup. Results for setup 1 reveal a triple dip structure, with the lateral dips being less than half the central one. For setup 2 we obtain a peak-dip-peak structure. All the lateral dips and peaks are asymmetric. 96

Figure 5.6 Same as figure 5.5, for energy-resolved packets. The loss of contrast of the central dip is dramatic. Three dips are still observed for setup 1, with an additional loss of contrast and an asymmetry for the lateral ones, but no peak is observed for setup 2. 97

Figure 5.7 Modulus of S_{HOM} in units of $e^2\mathcal{R}\mathcal{T}$ as a function of the time delay δT, for setups 1 and 2, with $u = 0.5v_F$ and $\Theta = 0.1\mathrm{K}$. Electron-hole interference: an electron has been injected on the right moving arm and a hole on the left moving one. Constructive interference is weaker than destructive interference. 99

Figure 5.8 Modulus of $S_{\mathrm{HOM}}(0)$ and $2S_{\mathrm{HBT}}$ in units of $e^2\mathcal{R}\mathcal{T}$ as a function of Γ, for $\epsilon_0 = 0.7\mathrm{K}$. $u = 0.5$ and $\Theta = 0.1\mathrm{K}$. The larger the wave-packet, the better the contrast. . . 99

Figure 6.1 Setup 1. Inter-channel interaction is switched on in the green region only, ranging from $-l$ to l. 103

Figure 6.2 On a right-moving channel, a wave-packet propagates at velocity v in regions 1 and 3, and w in region 2. The packet envelope is a piecewise function $\Psi = \Psi_j$ in region j. 105

Figure 6.3 Envelopes of a Gaussian (top panel) and an exponential (bottom panel) wave-packets, which propagate toward the right at velocities $w = 3$ in the interaction region (from $-l$ to l) and $v = 2$ elsewhere. The injection position is $x = -10$ and $l = 5$. The envelope is wider when the packet travels faster, but the area under the curve remains unchanged. 107

Figure 6.4 Charge density of a large wave-packet in energy on the left-moving outer channel (bottom panel) and inner channel (top panel), for an injection at $\alpha = 20\mu\mathrm{m}$ and $t = 0$. The interaction region ranges from $-l$ to l, with $l = 10\mu\mathrm{m}$. In this region, the fast and slow excitations have different shapes because of the velocity mismatch at the boundary $x = l$. At the interaction region output, the excitations are halves of the initial wave-packet, propagating at v again, but they have acquired a time delay. 112

Figure 6.5 $|S_{\mathrm{HBT}}|$ as a function of the propagation length under inter-channel interactions, for large packets in energy (top panel) and energy-resolved packets (bottom panel). For both setups, the blue curves stand for $w_+ = 2w_-$ ($u = 0.33v$) and the red ones for $w_+ = 8w_-$ ($u = 0.78v$). Typically, for $l > 7\mu\mathrm{m}$ a steady value independent of u is reached. At $l = 0$, the noise is zero for setup 2, and reduced from one for setup 1 because of anti-bunching with thermal excitations, leading to the same value as the $\nu = 1$ case. 115

Figure 6.6 Setup 1. An electronic wave-packet is injected on both incoming outer channels. It is fractionalized when entering the interaction region (colored in green). (Right inset) Electron density as a function of position for an energy-resolved packet, injected in the non-interacting region. Inter-channel interactions are switched on between −20 and 20μm. $w_+ = 2w_-$ and the time of propagation is $t = 0.2$ns. The fast excitations are spread whereas the slow ones are narrowed. 116

Figure 6.7 Normalized HOM noise at zero-time delay as a function of the escape time of energy-resolved wave-packets, in setup 1. $w_+ = 2w_-$, $l = 2.4$μm and the injection energy is $\epsilon_0 = 0.7$K. The finite interaction region model is in excellent agreement with the experimental data. The bottom of the dip rises with the escape time, or equivalently the energy-resolution of the wave-packets. The higher the escape time, the wider the packets in real space, and the more pronounced the difference between the infinite and finite interaction region cases. 118

Figure 6.8 Normalized HOM noise as a function of the time delay, for packets large in energy (top panel) and energy-resolved (bottom panel). The plain curves stand for setup 1, and the dashed ones fro setup 2. The dip-dip-dip and peak-dip-peak patterns are recovered for setups 1 and 2 respectively, though the lateral structures melt into the central dip. In the end, a widened dip is observed for setup 1, and a narrowed one for setup 2. . 120

Figure 7.1 Charge density on the outer (bottom panel) and inner (top panel) left-moving channels, after a propagation time $t = 1$ns, for wide packets in energy, and for different interaction strengths u. The injection position is $l = 5$μm. As the interaction strength between co-propagating channels is increased, the fast excitations travel faster and the slow ones travel slower, leading to an increased spatial splitting between the modes. . . . 126

Figure 7.2 Plots of the HBT noise at zero temperature as a function of the propagation length l, for energy-resolved (top panel) and large in energy (bottom panel) exponential wave-packets, for the interaction strengths $u = 0.3v_F, 0.5v_F, 0.7v_F$. The plain curves stand for setup 1, the dashed ones for setup 2, and the dotted ones for the logarithmic fits. The log fits show the divergence of S_{HBT} when $l \to \infty$. The divergence is faster for a higher interaction strength, and does not depend on the parameters of the packets. 129

Figure 7.3 Plots of the HBT noise as well as the bottom of the HOM dip at zero temperature as a function of the propagation length l for $u = 0.5v_F$, for a wide packet in energy ($\epsilon_0 = 175\text{mK}, \gamma = 1$) and an energy-resolved exponential wave-packet ($\epsilon_0 = 0.7\text{K}, \gamma = 8$), for setup 1. The log fits show the divergence of S_{HBT} when $l \to \infty$, while for large enough l, the bottom of the HOM central dip is unchanged when l is increased. 131

Figure 7.4 Plots of the HOM noise at zero temperature as a function of the time delay δT for energy-resolved wave-packets, and $\delta T \geq 0$ (the figure is symmetric for $\delta T < 0$). The depth of the central dip depends neither on l, nor on the considered setup. For both setups, lateral asymmetric dips are obtained, at a position scaling like l.133

Figure 7.5 Plots of the HOM noise at zero temperature as a function of the time delay δT for wide wave-packets in energy, and $\delta T \geq 0$. The depth of the central dip is l- and setup-independent, and lateral dips are obtained for both setups. The noise is lower than for energy-resolved packets, and the contrast of the central dip is better. 134

Figure 8.1 Schematic view of a quantum spin Hall bar. Electrons with opposite spin counter-propagate along each edge. Incoming and outgoing channels are connected through a scattering region Σ (shaded yellow square), typically given by a QPC. pair-electrons sources (PESs) are placed along the various edges of the sample: PES1 (green) inject excitations in the $(R\uparrow)$ incoming and $(L\downarrow)$ outgoing channels, PES2 (magenta) in the $(R\downarrow)$ incoming and $(L\uparrow)$ outgoing channels and PESS3 (orange) in the $(L\uparrow)$ incoming and $(R\downarrow)$ outgoing channels. 144

ACRONYMS

2DEG two-dimensional electron gas

FQHE fractional quantum Hall effect

FS Fermi sea

HBT Hanbury Brown and Twiss

HOM Hong-Ou-Mandel

IQHE integer quantum Hall effect

PES pair-electrons source

QPC quantum point contact

QSHE quantum spin Hall effect

SEM single electron microscope

TLL Tomonaga Luttinger liquid

TRS time-reversal symmetry

INTRODUCTION

1

INTRODUCTION TO ELECTRON QUANTUM OPTICS

Quantum mesoscopic physics, or quantum nanophysics, aim at describing electronic transport through systems which are smaller than the quantum mechanical coherence length. In such systems, the wave like character of electrons gives rise to interference effects, and is crucial to determine the transport properties of nanoscale systems.

Since the birth of mesoscopic physics in the early eighties, scientists in this exciting field were drawn to make parallels between electron flow and photon beams in quantum optics. By imposing a constant bias voltage between electrodes connected to a mesoscopic device, steady state currents were generated and analyzed through interferometric setups in close analogy with the propagation of light.

In the late eighties/early nineties people realized that while current measurements provided useful information, additional data could be gained by the measurement of temporal fluctuations of the current, called noise. In contrast to the current, noise measurements bear a direct signature of the statistics of the carriers which propagate through the sample. Experiments performing the fermionic analog of well-known quantum optics experiments, such as the Hanbury Brown and Twiss (HBT) experiment, were performed in the mid nineties: in particular, noise correlation measurements, where the signal of two outputs from the same source were combined, were able to show that the incoming electron beam consisted of a degenerate Fermi sea (FS). Since this time, noise measurements have become an accepted tool for analyzing the transport properties of a variety of mesoscopic samples (quantum Hall Bars, normal superconducting junctions, and so on...).

Yet quantum optics has always been a step ahead of the game: rather than using photon beams, experimentalists were able to build single photon sources, and therefore to prove the coherence of single photon wave packets. The famed Hong-Ou-Mandel (HOM) experiment did precisely this, as it probed the bunching behavior of two photons impinging on a half silvered mirror, as a function of the time delay between the two photonic pulses. This HOM

experiment has now become a paradigm of modern quantum mechanics.

On the mesoscopic physics front, no such experiments were performed. However, honed experimentalists managed to go beyond DC measurements by applying AC voltages to the leads connected to their samples, a field labeled as photo-assisted transport [90] because the AC signal was often generated by microwave sources. Progress on AC transport gained its importance through the beginning of the eighties.

In the mid two-thousands, a major breakthrough was achieved in mesoscopic physics with the completion of single electron sources. One of such was called the mesoscopic capacitor. In order to mimic the propagation of light through vacuum, electron wave guides consisting of quantum edge channels of the integer quantum Hall effect (IQHE) were employed (this system bears the advantage that electrons suffer very weak backscattering). A quantum dot, separated from an edge channel by a quantum point contact (QPC), was subject to an AC gate voltage in order to inject a train of individual electrons and holes. This particular device has been used recently to perform the electronic analog of the HOM experiment, yet in a condensed matter setting, giving rise to the new field of electron quantum optics, which is the main topic of this thesis.

Several differences can be identified when comparing this new physics to that of quantum optics with single photon sources. Photons bear no charge and propagate in vacuum: they interact via their statistics at the location of a half silvered mirror or in the medium of a non-linear crystal. They are bosonic particles with bunching behavior: several identical photons can be stacked in the same quantum state. In contrast, electrons are fermions and thus obey the Pauli principle: each electron can only occupy a single quantum state. The fact that they are charged also leads to Coulomb repulsion. In a condensed matter setup, the ground state of an electron system consists of a FS: at zero temperature, all electronic states below the Fermi level are occupied, while all states above this energy are empty. In the experiments on the single electron source, single electron excitations are generated above this FS (single hole excitations are generated below this sea). Theoretical modeling of the transport properties of this single electron source can therefore not avoid taking into account the presence of this FS. Moreover, Coulomb interactions are likely to give rise to energy exchange, causing a relaxation of the electronic wave packets. Coulomb interactions occur because the electronic wave guide is surrounded by electromagnetic gates, which constitute a source of decoherence for the electrons on the quantum edge channel. Alternatively, if the filling factor for electrons in the quantum Hall bar is larger than one, electrons between neighboring edge channels may interact, also allowing for energy exchange.

The present thesis is devoted toward making theoretical predictions in this new field of electron quantum optics. After introducing the main ingredients (IQHE, QPC...), we will predict the so called HOM dip for a system of non-

interacting electrons, yet taking into account the presence of the FS, and thus the statistics. The quantity which is necessary to quantify the anti-bunching properties of electrons is the noise auto- or cross-correlations, which play the role of a photon coincidence measurement in quantum optics.

Then, Coulomb interactions will be switched on and theoretical modeling will be entirely reviewed as the physics is dramatically changed. Nonetheless, we will attempt to model an experiment measuring the HOM dip at filling factor two, when two edge states are present. The striking result of this experiment is that the HOM dip does NOT vanish when the two electrons are injected simultaneously, which would constitute the result of a single electron prediction. We propose in this work that the role of the Coulomb interaction between neighboring edge channels is to constitute a source of decoherence.

Finally, predictions for the HOM experiment will be provided in this interacting framework, proving that the loss of quantum information in the neighboring channel indeed leads to a non-zero dip. The role of the temperature and of the length of the interaction region will be discussed in details, and quantitative comparisons will be established.

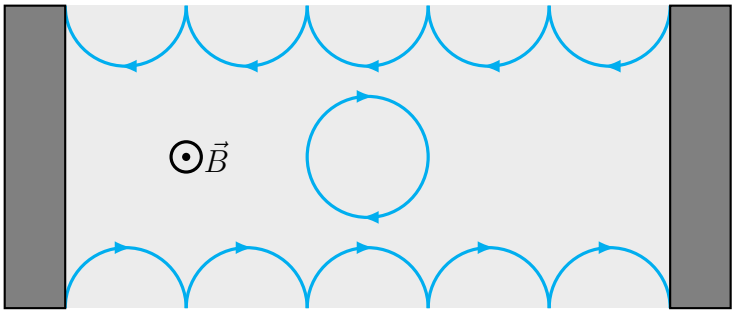

Figure 1.1: Semi-classical view of the IQHE: electrons move in cyclotrons orbits. These orbits are interrupted on the edges and electrons bounce forward, all in the same direction. Transport is therefore chiral.

1.1 THE QUANTUM HALL EFFECT

When a strong perpendicular magnetic field ($\sim$ 10T) is applied to a two-dimensional electron gas (2DEG) at low enough temperatures (below 1K), it enters the quantum Hall regime. The most striking phenomenon is that the transverse conductance of the sample becomes quantized in units of e^2/h, equal to the inverse of the resistance quantum $R_k \sim 25.8\text{k}\Omega$, and the longitudinal resistance vanishes. Furthermore, the bulk of the 2DEG becomes insulating and electronic transport occurs along one-dimensional channels located at the edges of the sample. This so-called IQHE was discovered by K. von Klitzing in 1980 [45], who was awarded the Nobel prize five years later.

Transport in the IQHE can be described in a semi-classical view by considering the cyclotron motion of electrons in the 2DEG in presence of a perpendicular magnetic field. The semi-classical motion of electrons is depicted in fig. 1.1: electrons in the bulk move in closed cyclotron orbits with a fixed center of motion, and therefore cannot travel from one end of the sample to the other. The cyclotron orbits of electrons near the edges, on the other hand, are interrupted by the edges, so that electrons "bounce" forward along skipping orbits. Because of the fixed direction of rotation, all electrons on one edge propagate in the same direction (in fig. 1.1, electrons in the upper edge propagate from left to right), whereas electrons near the other edge propagate in the opposite direction: electronic transport in the IQHE regime is therefore chiral.

The quantized value of the conductance can be explained by considering the energy spectrum of electrons in the 2DEG: electrons in the bulk are distributed on Landau levels with an energy $E_n = \hbar\omega_c(n + 1/2)$, where $\omega_c = |eB/m^*|$ is the cyclotron pulsation (the effective mass m^* of electrons in 2DEGs is equal to $0.067m_e$ with m_e the bare electron mass) [93]. These Landau levels are bent near the potential barriers constituting the edges of the sample (see

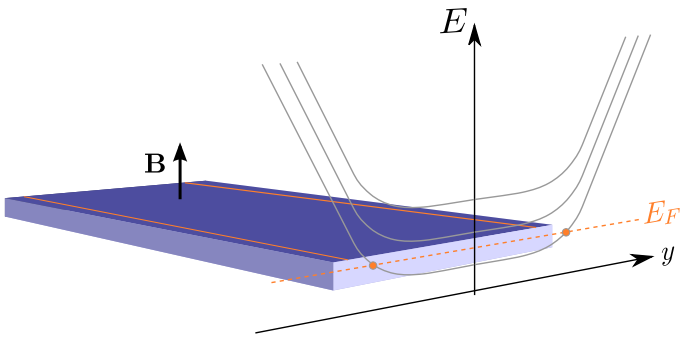

Figure 1.2: A high magnetic field is applied perpendicular to a 2DEG (purple), reaching the IQHE. Edge states (orange, plain) are formed at the intersection between the Fermi energy (orange, dashed) and the Landau levels (gray). Here, the filling factor is $\nu = 2$: 1 Landau level × 2 spins (Zeeman splitting is not shown here).

fig. 1.2). The finite number of electrons in the 2DEG defines the Fermi energy, which, for given values of the magnetic field, only crosses the Zeeman-split Landau levels near the edges, thus defining a finite number of chiral edge channels. This number depends on the magnetic field: as B increases, the Landau levels are shifted upward with respect to the Fermi energy, so that the number of Zeeman-split Landau levels crossing the Fermi level (that is, the number of filled Landau levels, called filling factor ν) decreases. In particular, at filling factor $\nu = 2$, electronic transport occurs on two edge channels, which are spin-polarized (the first Landau level is completely filled, spin up and spin down).

Finally, the absence of backscattering in the edge channels [10] dramatically increases the mean free path ($\sim 100\mu$m) of electrons; large phase coherence lengths have also been measured ($\sim 20\mu$m at 20mK [83]). In the quantum Hall regime, electrons thus propagate along one-dimensional, phase coherent, chiral edge channels without backscattering, that can be used as quantum rails in the realization of electron quantum optics experiments. In this respect, many studies (experimental as well as theoretical) have been performed in order to fully characterize the properties of electronic transport in edge channels: among others, the noiseless character of transport in edge channels has been demonstrated [81, 85]; an electronic Mach-Zehnder interferometer was used to measure the value of the phase coherence length given above, and the study of energy relaxation between adjacent edge channels was recently realized [6, 87, 24]. More generally, theoretical predictions were made regarding the relaxation and decoherence of electronic excitations in an edge channel in the presence of a FS [23].

1.2 QUANTUM POINT CONTACT

The electronic analog of a beam splitter can be implemented in a 2DEG in the form of a QPC which consists of a pair of electrostatic gates deposited on the surface of the sample. When a negative gate voltage is applied on the gates, a constriction is created in the 2DEG between the gates because of electrostatic repulsion (see fig. 2.1: the metallic gates (brown) are polarized by the gate voltage V_g). This constriction gives rise to a potential barrier, the shape of which can be determined from the geometry of the gates [9]. By tuning the gate voltage, one can selectively transmit or reflect each edge channel. In particular, when large negative gate voltages are applied, the potential barrier becomes very large, and no electron can be transmitted. The influence of the gate voltage is well illustrated by fig. 1.3, at filling factor $\nu = 2$. In setup 1, the inner channels are totally reflected, while the outer ones are partially transmitted or reflected. In setup 2, the outer channels are totally transmitted and the inner ones are partially transmitted or reflected.

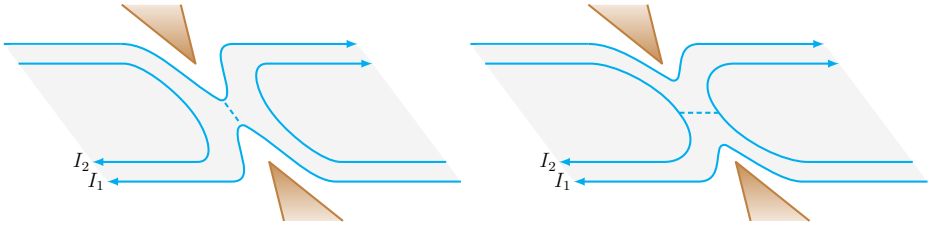

Figure 1.3: (Left) Setup 1: the inner channels are fully reflected, and the outer ones are partially transmitted or reflected. (Right) Setup 2: because of the smaller gate voltage, the outer channels are fully transmitted and the inner ones are partially transmitted or reflected.

At high magnetic field, the description of the transmission through the QPC in terms of spin-degenerate electronic modes is replaced by the description in terms of edge channels following equipotential lines, which are reflected one by one as the QPC gate voltage is swept towards large negative values. This effect was first experimentally demonstrated in [91], see fig. 1.4: the conductance at magnetic fields below $B = 1\mathrm{T}$ presents steps in units of $2e^2/h$. At high magnetic field, the height of the conductance steps is equal to e^2/h, reflecting the removal of spin-degeneracy. The number of conductance steps n decreases with the magnetic field, and corresponds to the number of edge channels (given by the filling factor ν). Between two conductance plateaus, the conductance G of the QPC is proportional to the transmission probability $\mathcal{T}$:

$$G = \mathcal{T} e^2/h \tag{1.1}$$

This equation is known as Landauer's formula [53]. R. Landauer has been a pioneer in mesoscopic transport, since he has developed a theory based on

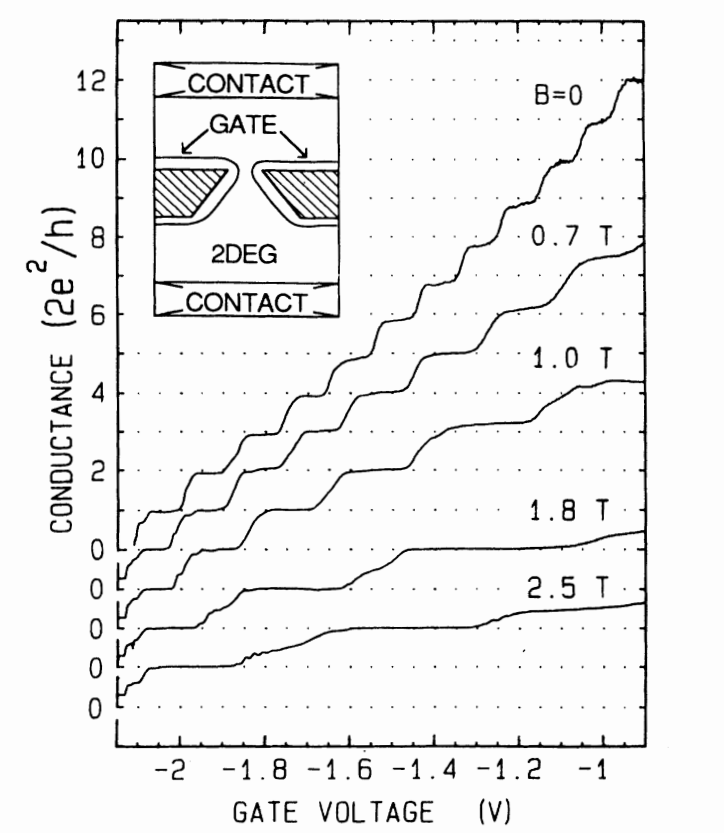

Figure 1.4: Taken from [91]. Conductance of a QPC as a function of gate voltage: it exhibits steps of value $2e^2/h$, corresponding to the progressive transmission of spin-degenerate edge-states. As the magnetic field is increased, the number ν of edge states decreases. For high fields, steps at e^2/h start appearing as the spin-degeneracy of Landau levels is lifted.

the scattering properties of the sample only. This relation can be generalized for a finite number of edge channels ν [11]:

$$G = \sum_{i=1}^{\nu} \mathcal{T}_i e^2/h \tag{1.2}$$

where $\mathcal{T}_i$ is the transmission of the ith edge channel. Fig. 1.4 therefore demonstrates that one can tune the transmission of a QPC by changing its gate voltage; in particular, when set at the exact half of the opening of the first conductance plateau, the outer edge channel is partially transmitted with a probability $|t|^2 = \mathcal{T} = 0.5$, while all other edge channels are fully reflected. The QPC therefore acts as a tunable, channel-selective beam splitter.

QPCs are crucial elements in electron quantum optics experiments, such as the electronic Mach-Zehnder interferometer, as they allow to put into evidence striking phenomena through noise measurements.

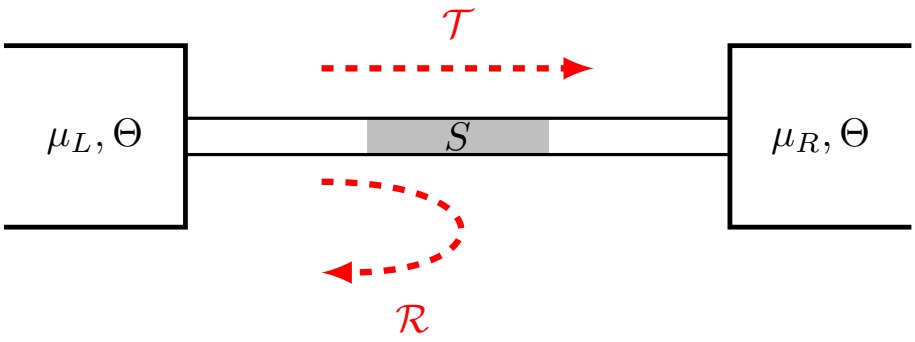

Figure 1.5: A mesoscopic sample (gray) characterized by its scattering matrix S connects two leads. Each lead is at temperature Θ and at chemical potential $\mu_{L,R}$. Electrons are transported through one channel of conduction, with transmission probability $\mathcal{T}$ and reflexion probability $\mathcal{R}$.

1.3 NOISE IN MESOSCOPIC PHYSICS

The conductance G of a sample is a crucial property, however, it is only related to the average character of electronic transport. The Landauer's formula (eq. (1.1)) is indeed obtained by computing the average current. So the current time-fluctuations around its average value have been totally ignored. These fluctuations are quantified by a quantity called *noise*, which is physically very rich, as it encodes properties about the particles correlations and statistics [67].

Let us consider a mesoscopic sample connecting two macroscopic leads at thermal equilibrium. They are characterized by their temperature Θ and their chemical potential $\mu_{L,R}$. In fig. 1.5, electronic transport occurs through one channel of conduction only, but this can be generalized to any number of channels. For each channel α, scattering through the sample is characterized by a transmission probability $\mathcal{T}_\alpha$ and a reflexion probability $\mathcal{R}_\alpha$.

1.3.1 *Origin and definition*

The noise has always aroused a lot of interest, as it was aimed to be suppressed for technological purposes. There are three main sources of noise: the $1/f$ noise, the thermal noise and shot noise. The $1/f$ noise has various origins, as disorder or defects in the crystalline network. It is proportional to the inverse of the signal frequency, hence the name, and to the applied voltage squared [31, 47]. This noise has been a limiting factor in the first experiments in mesoscopic physics, performed at low frequencies. Moreover, a non-zero temperature makes the occupation number of an energy level of a system fluctuate, which creates thermal noise. Finally, shot noise is directly

due to the electric charge quantization. It can only be measured when a voltage bias applied to the system forces it out of equilibrium ($\mu_L \neq \mu_R$). It is thus directly linked to electronic transport.

In the setup depicted in fig. 1.5, the incoming particles are either transmitted with the probability $\mathcal{T}$, or reflected with the probability $\mathcal{R}$. Even if the incoming particle beam is noiseless, the outgoing reflected and transmitted beams will be noisy [56]. Indeed, shot noise is due to the random character of partitioning on the scatterer.

Let us note n_I the occupation number of the incoming beam, n_T the occupation number of the transmitted beam, and n_R the occupation number of the reflected beam. If we suppose that the incoming beam is occupied with a probability 1, then the occupation number average value is $\langle n_I \rangle = 1$, and the fluctuations vanish: $\Delta n_I = n_I - \langle n_I \rangle = 0$. The impinging particle is either transmitted or reflected, with probabilities $\mathcal{T}$ and $\mathcal{R}$ respectively. Thus, either $n_T = 1$ and $n_R = 0$ in the first case, or $n_T = 0$ and $n_R = 1$ in the second case. Consequently the occupation numbers average values are given by: $\langle n_T \rangle = \mathcal{T}$ and $\langle n_R \rangle = \mathcal{R}$. Furthermore, as the occupation numbers are either zero or one, one still has: $\langle n_T^2 \rangle = \mathcal{T}$ and $\langle n_R^2 \rangle = \mathcal{R}$. Moreover, in any case, the product $\langle n_T n_R \rangle$ is zero. Finally, the outgoing beams occupation number fluctuations read:

$$\begin{aligned} \langle (\Delta n_T)^2 \rangle &= \langle (\Delta n_R)^2 \rangle = \mathcal{T}(1-\mathcal{T}) \\ \langle \Delta n_T \Delta n_R \rangle &= -\mathcal{T}(1-\mathcal{T}) \end{aligned} \tag{1.3}$$

These classical results will appear later as prefactors in noise calculations, testifying that it is associated with partitioning of the impinging particles.

These heuristic arguments are well suited for single particles. But electrons cannot be taken apart from the FS, and a many-particle approach has to be considered instead. Consequently, one has to define the noise [66] in a more rigorous way. Rather than the occupation numbers, we focus on the outgoing currents, which are measured experimentally. The noise -or current correlations- between terminals m and n is defined as:

$$\begin{aligned} S_{mn}(\omega) &= \lim_{T\to+\infty} \frac{2}{T} \int_{-T/2}^{T/2} dt \int dt' e^{i\omega t'} \langle \Delta I_m(t) \Delta I_n(t+t') \rangle \\ &= \lim_{T\to+\infty} \frac{2}{T} \int_{-T/2}^{T/2} dt \int dt' e^{i\omega t'} \langle I_m(t) I_n(t+t') \rangle - \langle I_m \rangle \langle I_n \rangle \end{aligned} \tag{1.4}$$

with $\Delta I_m(t) = I_m(t) - \langle I_m \rangle$ the current fluctuations with respect to its average value. All along this thesis, when not specified, the domain of integration is the whole real axis. For $n = m$, S_{mm} is called the auto-correlation noise on channel m, or current auto-correlations. For $n \neq m$, it is sometimes called cross-correlations.

From now on, we restrict our study to zero-frequency noise, as its computation in several electron quantum optics setups is the main topic of this thesis.

1.3.2 *Thermal noise*

At finite temperature, the occupation numbers of the energy levels are subject to thermal fluctuations, caused by thermal agitation. Consequently, an equilibrium noise arises, as established by J. B. Johnson [42] and H. Nyquist [75] in 1928. It is observed for a zero voltage between the leads ($\mu_L = \mu_R$) and a non-zero temperature ($\Theta \neq 0$), or as long as the voltage is much lower than the temperature ($eV \ll k_B\Theta$).

We make the assumption that the transmission and reflexion probabilities are independent of the energy. The average occupation number $\langle n \rangle$ is equal to the Fermi distribution f. Thus, the probability for a state not to be occupied is given by $(1-f)$, and the average occupation number fluctuations equal: $\langle (\Delta n)^2 \rangle = f(1-f)$, with $\Delta n = n - \langle n \rangle$. Using the identity $f(1-f) = -k_B\Theta \partial f / \partial E$, one finds the Johnson-Nyquist noise:

$$S(\omega = 0) = 4k_B\Theta G\,. \tag{1.5}$$

This result could be obtained using the fluctuation-dissipation theorem, as it shows that the fluctuations at equilibrium are proportional to the generalized susceptibility, given by the conductance.

Eq. (1.5) is equivalent to the knowledge of the conductance, and does not bring additional information about the current time-fluctuations. Such information are obtained out of equilibrium.

1.3.3 *Shot noise*

Contrary to the Johnson-Nyquist noise, shot-noise is due to an out of equilibrium situation. It can only be probed when a voltage bias is applied between the leads: $\mu_L - \mu_R = eV$. At zero temperature, the auto-correlation noise reads [67, 8, 7]:

$$S_{LL}(0) = S_{RR}(0) = \frac{4e^2}{h} eV \sum_\alpha \mathcal{T}_\alpha (1 - \mathcal{T}_\alpha) \tag{1.6}$$

In section 1.2, we have seen that the conductance is quantized and exhibits steps when all the conduction channels have a transmission probability around either 0 or 1 (see fig. 1.4). For spin-degenerate levels, the conductance is then a multiple of $2e^2/h$. In such a case, the term $\sum_\alpha \mathcal{T}_\alpha(1-\mathcal{T}_\alpha)$ appearing in eq. (1.6) vanishes. Measurements have confirmed this noise cancellation [59, 81, 50, 19] for the conductance being a multiple of $2e^2/h$ (see fig. 1.6).

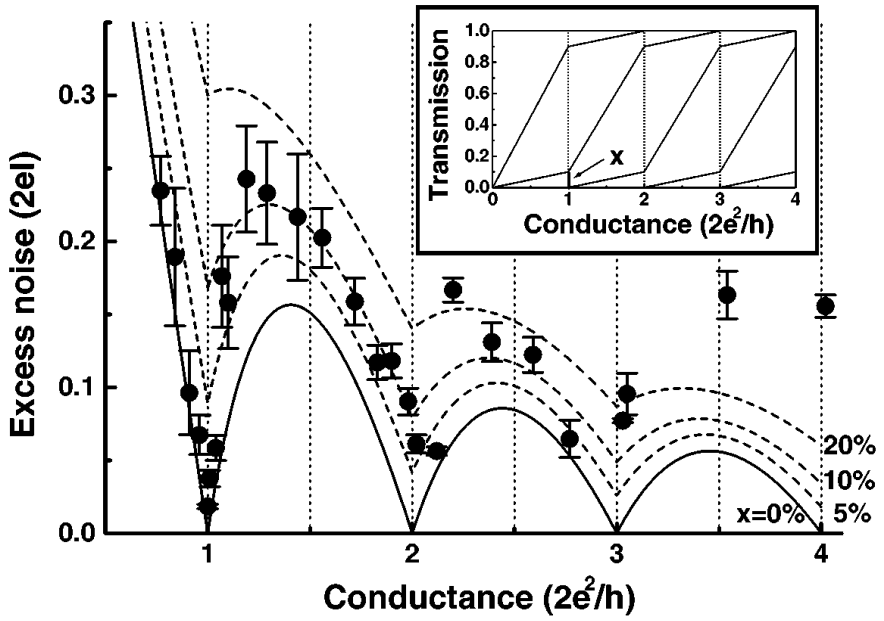

Figure 1.6: Taken from [19]. Noise as a function of conductance. It vanishes when the conductance is then a multiple of $2e^2/h$. In dashed, theoretical predictions including thermal noise are plotted.

When considering a single channel at zero temperature, the average current reads: $\langle I \rangle = (2e/h)eV\mathcal{T}$. Thus, eq. (1.6) can be written:

$$S_{LL}(0) = 2e\langle I \rangle(1-\mathcal{T}) \tag{1.7}$$

The noise is reduced by the $(1-\mathcal{T})$ factor, compared to the classical Poissonian case in which $S = 2e\langle I \rangle$. The noise is then called sub-Poissonian.

Furthermore, the noise is proportional to the average current and to the charge of the tunneling excitations. Consequently, knowing both the current and the zero-frequency noise gives access to the charge of the carriers. In this way, the fractional charge of the quasi-particles in the fractional quantum Hall effect (FQHE) was measured [85, 79].

Part I

ELECTRONIC HONG-OU-MANDEL INTERFEROMETRY IN NON-INTERACTING QUANTUM HALL REGIMES

The HOM interferometer is a celebrated tool of quantum optics, where two photons are sent on the two input channels of a beam splitter, while measuring the coincidence rate at the two outputs. A dip is observed when the photons are identical and arrive simultaneously at the splitter, as they necessarily go to the same output because of bosonic statistics. Measuring this dip can give access to the time difference between the photons, and to the length of the photon wave-packet [40]. Since the first HOM experiments, many works have used this interferometer, e.g. to characterize single photon sources and photon indistinguishability [78, 41], to demonstrate the control of interferences with a resonant cavity [84, 94], to perform interference between two photon pairs [20], etc.

In order to perform the electronic analog of the HOM experiment, two electrons must propagate ballistically and in a coherent way toward each other, and then collide. These conditions are precisely fulfilled in the IQHE (see section 1.1): electrons propagate along one-dimensional, phase coherent, chiral edge channels without backscattering. This regime is the most suitable to implement electron optics experiments. Firstly, because electrons can be guided along one dimensional quantum rails, secondly because chirality prevents interferences between the electron sources and the optics-like setup used to characterize it.

Thus, the most simple framework to perform electronic HOM interferometry is the IQHE at filling factor $\nu = 1$ in the absence of interactions. This situation is described in the present part.

2

ELECTRON QUANTUM OPTICS AT FILLING FACTOR $\nu = 1$

2.1 CONTEXT

First, the on-demand single electron injection process required to perform interferometry is described, both from a practical and a theoretical points of view. Then, we turn to the single-particle and two-particle interferometry: how is it implemented and what is the quantity of interest?

2.1.1 *Single electron source*

2.1.1.1 *Principle*

The first manipulations of electrical currents at the single charge scale have been implemented in metallic electron boxes. These single electron pumps take advantage of the charge quantization to generate quantized currents [33, 35, 55]. Another route for quantized current generation is to trap a single electron in the electrostatic potential generated by a surface acoustic wave propagating through the sample. This technique has recently enabled the transfer of single charges between two distant quantum dots [39]. Single particle states in ballistic conductors can also be generated by replacing the DC bias applied to an ohmic contact, by a pulsed time-dependent excitation $V_{\mathrm{exc}}(t)$ [27]. For an arbitrary time dependence and amplitude of the excitation, such a time-dependent bias generates an arbitrary state that, in general, is not an eigenstate of the particle number but is the superposition of various numbers of electron and hole excitations.

However, the electron source we will focus on follows a different route to generate single particle states. The emitter, called a mesoscopic capacitor, con-

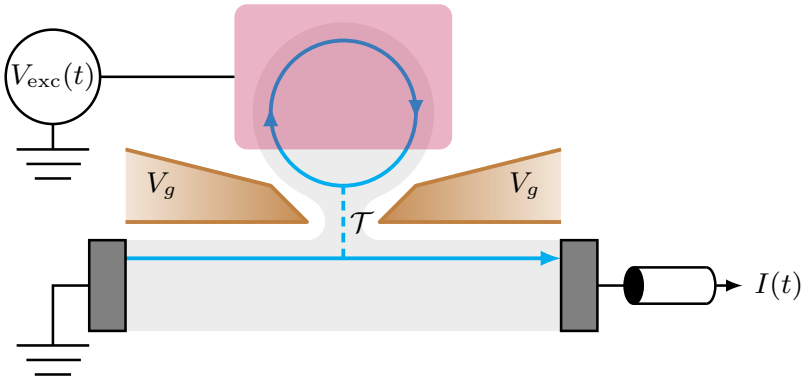

Figure 2.1: Sketch of the mesoscopic capacitor. A time dependent voltage $V_{\mathrm{exc}}(t)$ is applied to the metallic top gate (magenta) capacitively coupled to the dot (circular edge state). The strength of the tunnel coupling between the circular and linear edge channels (blue) is controlled by the gate voltage V_g, and thus the QPC transparency $\mathcal{T}$. The current $I(t)$ is measured at the output.

sists in a quantum dot capacitively coupled to a metallic top gate and tunnel coupled to the conductor. A fundamental difference with the aforementioned pumps is that the source is AC driven and thus generates a quantized AC current.

The mesoscopic capacitor is depicted in Fig. 2.1. It consists in a submicron-sized cavity -or quantum dot- made of a circular edge channel of the IQHE, tunnel coupled to a two-dimensional electron gas through a QPC. The QPC transparency $\mathcal{T}$ is controlled by the gate voltage V_g, which makes the constriction more or less narrow by depleting the electron gas below it. The potential of the dot is controlled by a metallic top gate deposited on top of it and capacitively coupled to it (in magenta in Fig. 2.1).This conductor realizes the quantum version of a RC circuit, where the dot and electrode define the two plates of a capacitor while the QPC plays the role of the resistor. A large perpendicular magnetic field is applied to the sample in order to reach the integer quantum Hall regime at filling factor one, where a single edge channel is coupled to the dot. Electronic transport can thus be described by the propagation of spinless electronic waves in a one-dimensional conductor. Electrons in the incoming edge channel can tunnel onto the quantum dot, perform several round-trips inside the cavity, each taking the finite time $\tau_0 = l/v$ -l is the dot circumference-, before finally tunneling back out into the outgoing edge state. For a micron-sized cavity, τ_0 typically equals a few tens of picoseconds. As a result of these coherent oscillations inside the electronic cavity, the propagation in the quantum dot can be described by a discrete energy spectrum with energy levels that are separated by a constant level spacing Δ related to the time of one round-trip: $\Delta = h/\tau_0$. The levels are broadened by the finite coupling between the quantum dot and the electron gas, determined by the QPC transmission $\mathcal{T}$. This discrete spectrum can be shifted compared to the

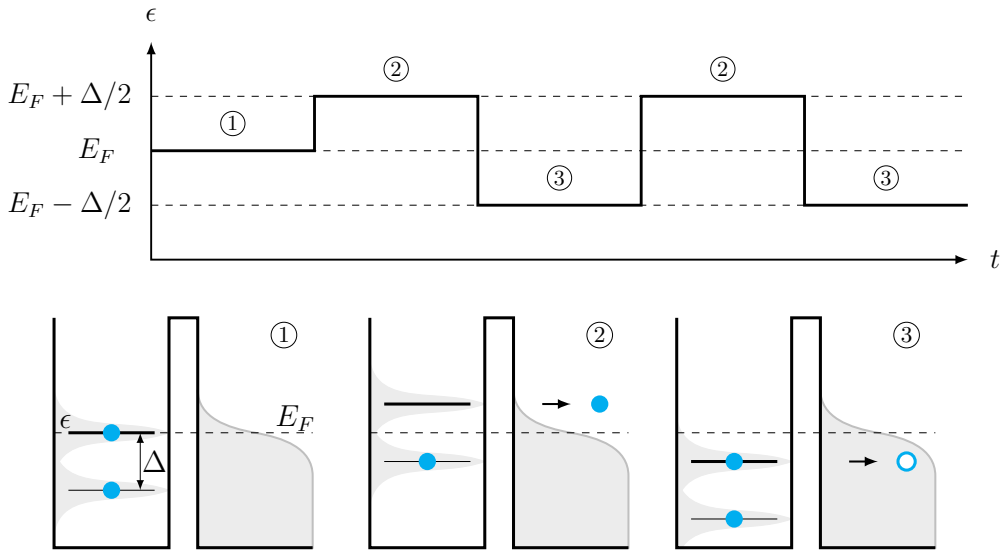

Figure 2.2: (Top panel) In the optimal emission regime, the highest occupied level in the dot ϵ is originally at resonance with Fermi energy E_F. A periodic step voltage $V_{\text{exc}}(t)$ is then applied, resulting in ϵ varying from $E_F + \Delta/2$ to $E_F - \Delta/2$. (Bottom panel) In the first half period (labeled ②), an electron is emitted, and in the second half period (labeled ③), a hole is emitted.

Fermi energy first in a static manner, when a static potential V_0 is applied to the top gate, but also dynamically, when a time dependent excitation $V_{\text{exc}}(t)$ is applied. A square shape excitation causes a sudden shift of the quantum dot energy spectrum. The mesoscopic capacitor takes advantage of this property to emit periodically a single electron followed by a single hole.

First, we consider the optimal situation where the highest occupied energy level of the dot ϵ is initially located at resonance with the Fermi energy E_F of the linear edge state, in the absence of drive (see Fig. 2.2 step ①). When a square drive is applied with a peak to peak amplitude Δ, an electron is emitted above the Fermi energy in the first half period (labeled ② in Fig. 2.2). The emission is indeed triggered by the sudden rise of the dot potential, which brings the last occupied energy level of the quantum dot above the Fermi energy. In the second half period (labeled ③ in Fig. 2.2), the potential is brought below the Fermi energy, and thus the dot is reloaded by the absorption of one electron, corresponding to the emission of one hole in the FS. Steps ② and ③ are then repeated alternatively at a drive frequency of $f \sim 1$GHz, which gives rise to periodic emission of a single electron followed by a single hole [30].

Then, the second regime is the so-called resonant emission regime, where the initial highest occupied level of the dot is set at $\epsilon = E_F - \Delta/2$ (see Fig. 2.3 step ①). The applied voltage still consists of sharp steps with amplitude Δ, but the dot levels are shifted with respect to the optimal emission regime, so that there is always one dot level which is resonant with the Fermi level of the edge (see Fig. 2.3 steps ② and ③). The dot levels go back and forth between energies $E_F + n\Delta$ and $E_F + (n+1)\Delta$, with n an integer. Electron and hole emis-

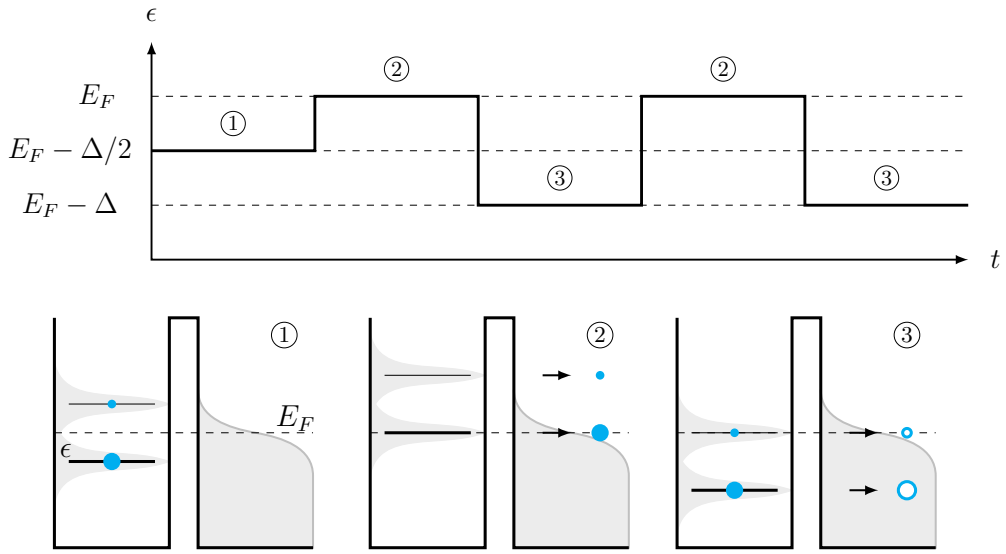

Figure 2.3: (Top panel) Applied step voltage in the resonant emission regime. (Bottom panel) Initially, the Fermi energy is in between two energy levels of the dot (step ①). When applying the excitation voltage, one level of the dot is always at resonance with the Fermi energy (steps ② and ③). Thus, both the electron and hole emissions occur for some part at resonance with E_F.

sion thus happens for an important part at the Fermi energy.

The energy contents of two electrons emitted in the optimal and resonant emission regimes are very different. In the first case, the electron is emitted above the Fermi energy, at $\epsilon = E_F + \Delta/2$, whereas in the resonant emission regime, it is emitted for an important part at the Fermi energy. As detailed in section 2.3, the overlap between the emitted electron energy distribution and the Fermi distribution conditions the noise related to the electron partitioning. Furthermore, as the mesoscopic capacitor is AC driven, the emission of a single electron is always followed by the emission of a single hole. This ability to inject both single electrons and holes will allow to probe electron-hole interference as well as electron-electron interference. In the optimal emission regime, the electron and the hole emitted at steps ② and ③ do not overlap in energy, whereas they do in the resonant emission regime. Consequently, this latter regime is better suited to probe electron-hole interference.

2.1.1.2 *Theoretical description*

This system can be very accurately described using the Floquet scattering formalism [71], which takes advantage of the time-periodicity of the drive. This description is very accurate insofar as the finite temperature, the level spacing Δ in the dot, and the level broadening due to the coupling to the electron gas are precisely taken into account [77]. For example, the average current can be computed: it is well fitted by an exponential decay, allowing to extract the escape time τ_e from the dot. It is directly related to the QPC gate voltage

V_g and thus the QPC transparency $\mathcal{T}$. The larger the transparency is, the less time it takes for the electron to get out of the dot and the smaller τ_e is.

Although very realistic, the Floquet calculations are too heavy to be combined with the noise calculations we intend to perform here. Consequently, they can only provide numerical results, which will be compared with our analytical formulas.

In a simpler way, a single electron emission by the source, processed in the optimal regime, can be modeled as the injection of an exponential electronic wave-packet. This model is less generic, insofar as it only applies to the optimal emission regime, but that regime is the one we will mainly focus on. The state outgoing from the capacitor is written:

$$|\varphi_\mu\rangle = \int \frac{dk}{\sqrt{2\pi}} \varphi^e_\mu(k) \psi^\dagger_\mu(k)|0\rangle \tag{2.1}$$

where μ labels the edge channel coupled to the capacitor. $\varphi^e_\mu(k)$ is the normalized electronic wave-function in momentum space, $\psi^\dagger_\mu$ is the electronic creation operator, and $|0\rangle$ denotes the FS. In the same way, a single hole could be injected by the application of an annihilation operator, rather than a creation operator:

$$\int \frac{dk}{\sqrt{2\pi}} \varphi^h_\mu(k) \psi_\mu(k)|0\rangle \tag{2.2}$$

These electron and hole prepared states can be written for any kind of wave-packets. However, the most realistic shape is exponential in real-space: $\varphi^e_\Gamma(x) = \sqrt{2\Gamma} e^{ik_0 x} e^{\Gamma x} \theta(-x)$ where $\theta(x)$ is the Heavyside function. Such a wave-packet is Lorentzian in energy-space: $\varphi^e_\Gamma(k) = \sqrt{\Gamma/\pi}/\left[(k-k_0)+i\Gamma\right]$.

Two parameters can be tuned in the emitted particle wave-function. First, k_0 is the injection energy of the electron (hole), it corresponds to $E_F + \Delta/2$ ($E_F - \Delta/2$) when the source is processed in the optimal regime (see fig. 2.2). Second, Γ is the energy width of the wave-packet, which depends on the coupling between the dot and the edge channel. It is inversely proportional to the electron escape time τ_e. Thus, when the transparency $\mathcal{T}$ of the dot is increased, the particle will escape from it quickly, with a large energy width.

Finally, the sates given by eq. (2.1) and (2.2) will be used to compute operator averages. Indeed, averaging over one of these prepared states, rather than the FS, amounts to considering that a single particle has been emitted by the capacitor.

2.1.2 *Setups and measurement*

Translating quantum optics experiments to electron quantum optics ones requires a dictionary. We have already seen that single electron sources are now available, providing the analog of a photon-gun for electrons. In the same way, the edge channels of the IQHE allow the ballistic and coherent one-dimensional propagation of electrons, mimicking beams for photons. Finally, a QPC allows either the transmission or the reflection of the impinging electrons, as a beam splitter does for photons. With this simple dictionary in mind, the HBT and HOM quantum optics setups can be transposed to quantum electronics.

The historical HOM setup consists in sending two photons on the two input channels of a beam splitter, and measuring the coincidence rate at the two outputs. Let us label the two outputs 1 and 2, and $N_{1(2)}$ is the number of particles on channel 1(2). When the time delay δT between arrivals of the photons at the beam splitter is large, they are transmitted or reflected independently, and the coincidence rate reaches a steady value. However, when the photons arrive simultaneously at the splitter, they become sensible to their exchange statistics. As photons are bosons, they tend to bunch -be stacked in the same state- and thus exit in the same output of the splitter. Consequently, the coincidence rate between the two outputs $\langle N_1 N_2 \rangle$ drops down to zero. Its measurement as a function of the time delay between arrivals at the splitter, or equivalently the difference between the propagation lengths of the input arms, exhibits a so-called HOM dip (see Fig. 2.4 second column).

In the electronic analog of the HOM setup, two electrons are aimed at a QPC through edge channels of the IQHE. When the time delay between arrivals at the QPC is large, the electrons are partitioned independently and exit in either one or the other output channel. But, when they reach the QPC simultaneously, their fermionic nature forbids them to be superimposed in the same state, in agreement with the Pauli principle. Indistinguishable electrons anti-bunch: the only possible outcome is to measure one electron in each output arm. For fermions, the coincidence count for indistinguishable particles would thus be doubled compared to the classical case. However, as single shot detection is not available yet for electrons, this anti-bunching is not probed by coincidence counts but rather by the low frequency fluctuations of the electrical current transmitted in the outputs. Indeed, the number of particles fluctuations $\langle \delta N_1^2 \rangle = \langle \delta N_2^2 \rangle$ directly reflect the electronic anti-bunching. In analogy with the HOM dip observed for bosons, a Pauli dip is expected for fermions (see Fig. 2.4 third column), albeit on a different quantity. As shown later, the shape of this dip provides valuable information on the electronic wave-packets.

The HBT experiment can be viewed as a peculiar case of HOM interferometry. Instead of placing a single electron source on each input of the QPC, a capacitor is coupled to one incoming arm only -or, similarly, one of the two

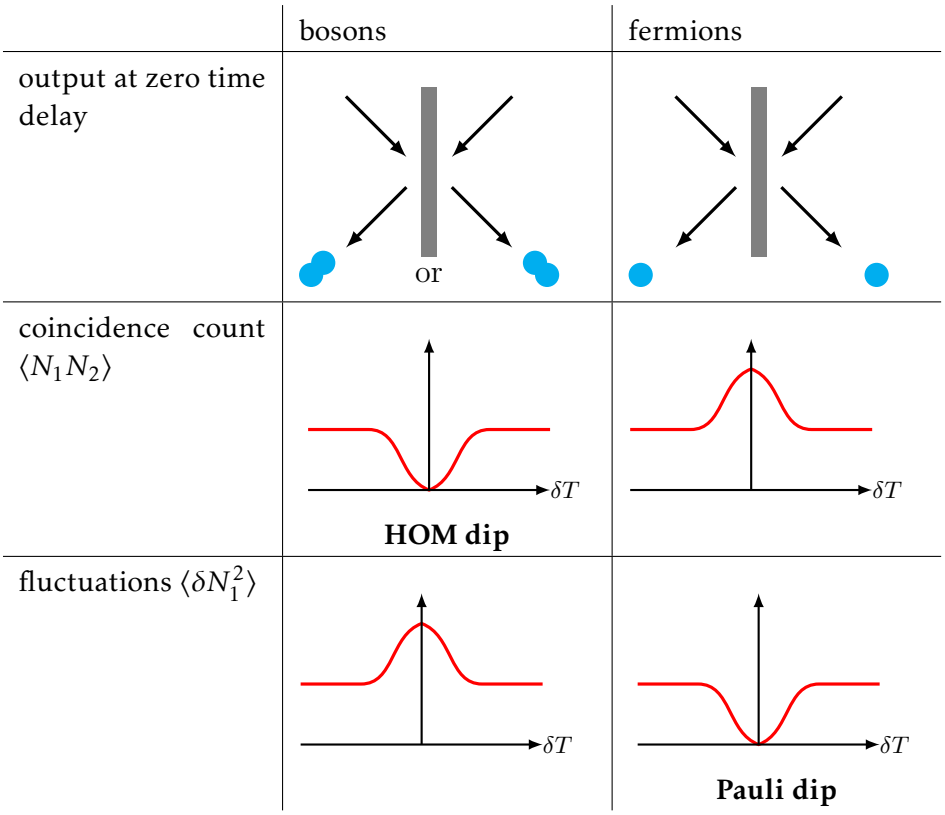

Figure 2.4: Sketch of the experiment. Two indistinguishable particles are partitioned on a splitter. Coincidence counts $\langle N_1 N_2 \rangle$ and number of particles fluctuations $\langle \delta N_1^2 \rangle$ are recorded as a function of the tunable delay δT. Indistinguishable bosons always exit in the same output, which results in the suppression of the coincidence rate (HOM dip) and the doubling of the fluctuations. An opposite behavior is expected for indistinguishable fermions: anti-bunching results in the doubling of the coincidence counts and the suppression of the number of particles fluctuations (Pauli dip).

sources is switched off. The other input arm is populated by thermal electron-hole excitations. These thermal excitations interfere with the ones produced by the source, affecting their partitioning, as they anti-bunch. Classically, the average number of electron-hole pairs emitted in one period can be directly extracted from the low frequency current correlations. But because of this anti-bunching, some of the source excitations cannot be distinguished from thermal ones and do not contribute to the partition noise, which is thus reduced. This effect provides a powerful tool to probe the energy distributions of the excitations produced by the source [36].

Finally, the setup is sketched in fig. 2.5: two counter-propagating edge states meet at a QPC. A single electron emitter is connected to each incoming edge state, and single electrons can be injected with a controlled time difference δT in the two edge states. Each source can be alternatively switched off, so that the HBT noise produced by the other source can be measured. In the HOM setup, when both sources are on, the current correlations are measured at the two outputs of the QPC, as a function of the time difference between the two

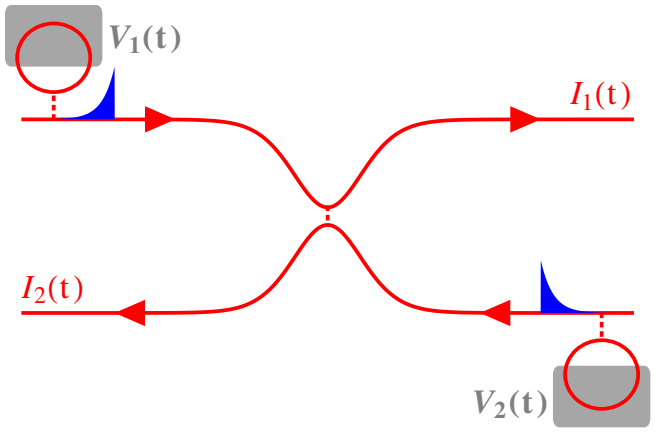

Figure 2.5: The device for electron HOM interferometry. Two chiral edge states meet at a quantum point contact. In each edge state, a single electron source injects an electron when a time-dependent voltage $V(t)$ is applied at the source. Cross-correlations at the two outputs are measured as a function of the time difference between the emitted electrons by each source.

injections. As explained in section 2.1.1, in existing experiments, the emission of a single electron and then a single hole is repeated periodically [30, 64, 77]. Consequently, by properly detuning one source with respect to the other, not only can the interference between two electrons be considered, but also the interference between one electron and one hole. This last case has no counterpart with photons: positive interferences (a peak rather than a dip) are obtained, which depend on the energy overlap between the electron and hole wave-packets, and which are strongly affected by temperature.

A single electron microscope (SEM) picture of the sample is also provided in fig. 2.6.

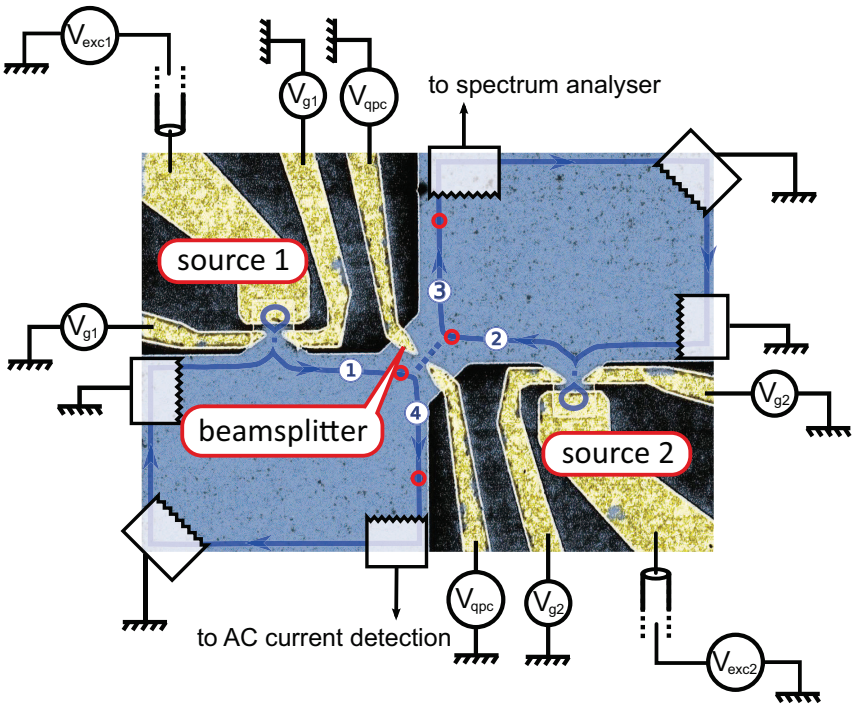

Figure 2.6: Taken from [15]. Sketch of the sample based on a SEM picture. The electron gas is represented in blue. Two single electron emitters are located at inputs 1 and 2 of a QPC used as a single electron beam-splitter. Each emitter can be switched on or off, in order to implement either the HBT or the HOM experiment.

2.2 THEORETICAL MODEL

2.2.1 *Outgoing cross-correlations*

We are interested in the the zero-frequency current cross-correlations between the outputs of the central QPC -which are measured experimentally-, or equivalently the excess auto-correlations. They directly measure the contribution of the excess excitations produced by the source. They are proportional to the number of particles fluctuations and probe anti-bunching between the interfering fermions. They read:

$$S_{12}^{out} = \int dt\, dt' \left\langle I_1^{\text{out}}(x^+,t) I_2^{\text{out}}(x^-,t') \right\rangle - \left\langle I_1^{\text{out}}(x^+,t) \right\rangle \left\langle I_2^{\text{out}}(x^-,t') \right\rangle \ , \quad (2.3)$$

with I_μ^{out} the current on the outgoing channel μ, and $x^+(x^-)$ the measurement position on channel 1(2), as depicted in fig. 2.7. The current operator is readily expressed in terms of the electronic creation and annihilation operators as

$$I_\mu^{\text{out}}(x,t) = -e : \psi_{\mu,\text{out}}^\dagger(x,t)\psi_{\mu,\text{out}}(x,t) : \quad (2.4)$$

where the normal order noted : ... : is taken with respect to the FS and enables to rule out its contribution. We have set the Fermi velocity $v_F = 1$. Because of the linear dispersion of the edges, the currents depend on $t - x^+$ and $t' + x^-$ only, on channels 1 and 2 respectively.

$$\begin{aligned} S_{12}^{\text{out}} &= \int dt\, dt' \left\langle I_1^{\text{out}}(0,t-x^+) I_2^{\text{out}}(0,t'+x^-) \right\rangle \\ &\quad - \left\langle I_1^{\text{out}}(0,t-x^+) \right\rangle \left\langle I_2^{\text{out}}(0,t'+x^-) \right\rangle \\ &= \int dt\, dt' \left\langle I_1^{\text{out}}(0,t) I_2^{\text{out}}(0,t') \right\rangle - \left\langle I_1^{\text{out}}(0,t) \right\rangle \left\langle I_2^{\text{out}}(0,t') \right\rangle \end{aligned} \quad (2.5)$$

Note that the zero-frequency cross-correlations no longer depend explicitly on the measurement positions $x^\pm$. This allows us to write the cross-correlations in terms of the currents measured at the immediate output of the QPC ($x^+ = 0^+$ and $x^- = 0^-$). As it turns out, these outgoing currents can be easily expressed in terms of the incoming ones.

Scattering at the QPC between the two edge states is modeled in a convenient way by a scattering matrix rather than a microscopic description. Using this theory is permitted insofar as free electrons are propagating on the edges. The fermionic fields outgoing from the QPC are expressed as a simple linear combination of the incoming ones, weighted by the appropriate factors in order to properly mimic transmission and reflexion. One thus has for fermionic fields near the QPC:

$$\begin{pmatrix} \psi_2^{\text{out}}(t) \\ \psi_1^{\text{out}}(t) \end{pmatrix} = \begin{pmatrix} \sqrt{\mathcal{T}} & i\sqrt{\mathcal{R}} \\ i\sqrt{\mathcal{R}} & \sqrt{\mathcal{T}} \end{pmatrix} \begin{pmatrix} \psi_2^{\text{in}}(t) \\ \psi_1^{\text{in}}(t) \end{pmatrix}, \quad (2.6)$$

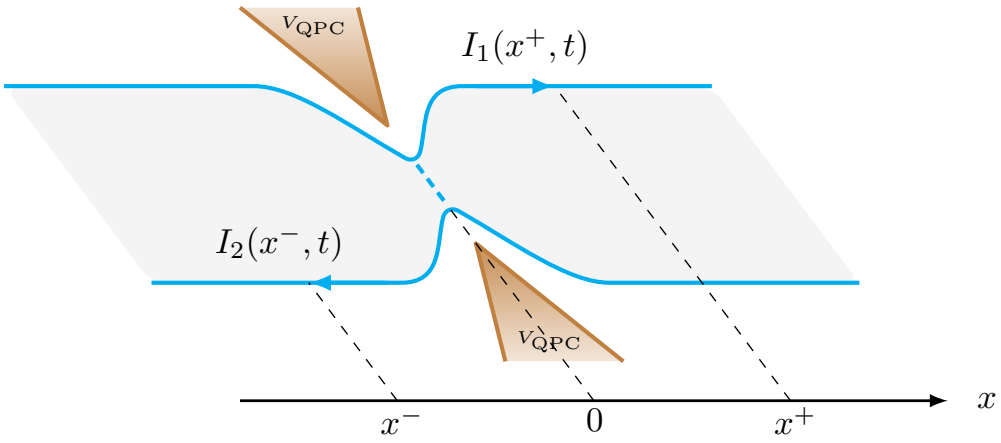

Figure 2.7: The positions are defined on an axis oriented towards the right. The QPC, whose transparency is tuned by varying the voltage V_{QPC}, is located at $x = 0$.

and similarly for the currents

$$\begin{aligned} I_1^{out}(t) &= \mathcal{T} I_1(t) + \mathcal{R} I_2(t) + ie\sqrt{\mathcal{R}\mathcal{T}}(\psi_1^\dagger\psi_2 - \psi_2^\dagger\psi_1)(t) \\ I_2^{out}(t) &= \mathcal{R} I_1(t) + \mathcal{T} I_2(t) - ie\sqrt{\mathcal{R}\mathcal{T}}(\psi_1^\dagger\psi_2 - \psi_2^\dagger\psi_1)(t) \end{aligned} \tag{2.7}$$

where $\mathcal{T}$ and $\mathcal{R} = 1 - \mathcal{T}$ are the transmission and reflection probabilities, and we have dropped the in superscript. Using these expressions in eq. (2.3) allows us to express the noise in terms of averages of incoming operators only [**?**].

$$S_{12}^{out} = \mathcal{R}\mathcal{T}\,(S_{11} + S_{22} - \mathcal{M}) \tag{2.8}$$

where the first two terms are the autocorrelation noises on the two incoming edges: $S_{\mu\mu} = \int dtdt' \langle I_\mu(t) I_\mu(t')\rangle - \langle I_\mu(t)\rangle\langle I_\mu(t')\rangle$. The last term combines averages on both incoming edges:

$$\begin{aligned} \mathcal{M} = e^2 \int dtdt' \, &\langle \psi_1(t)\psi_1^\dagger(t')\rangle\langle\psi_2^\dagger(t)\psi_2(t')\rangle \\ &+\langle\psi_1^\dagger(t)\psi_1(t')\rangle\langle\psi_2(t)\psi_2^\dagger(t')\rangle\,. \end{aligned} \tag{2.9}$$

An important point to notice is that this result only depends on the properties of the QPC through the prefactor $\mathcal{R}\mathcal{T}$. Note that this prefactor is the partition noise obtained classically, as derived in eq. (1.3). It is present in both the HBT setup -with either source on-, and the HOM setup -with both sources on. Therefore, when taking the ratio of the HOM over the HBT result, this prefactor simplifies and the final result is independent of the properties of the QPC.

As explained in section 2.1.1.2, the single particle injection is taken into account by averaging over a prepared state, which amounts to the creation of an electron or hole exponential wave-packet. In the HBT experiment, when the emitter 1 is on and the emitter 2 is off for example, it reads $|\Psi\rangle = |\varphi_1\rangle \otimes |0\rangle$. For the HOM setup, the prepared state is given by $|\Psi\rangle = |\varphi_1\rangle \otimes |\varphi_2\rangle$, with

$|\varphi_\mu\rangle$ defined in eq. (2.1) for an electron injection and in eq. (2.2) for a hole injection. In practice, we will only be interested in the correlations which arise as a consequence of the injected objects. As a result, we need to subtract the contribution from the FS, which is readily obtained by averaging over the FS rather than the prepared state, so that we now focus on:

$$\Delta S_{12}^{out} = \mathcal{RT}\left(\Delta S_{11} + \Delta S_{22} - \Delta\mathcal{M}\right) . \tag{2.10}$$

2.2.2 *Mixed term*

Let us first compute the mixed term $\Delta\mathcal{M}$. It can be expressed either in real space or in k-space, reminding that:

$$\psi_\mu(t) = \int_0^\infty \frac{dk}{\sqrt{2\pi}} e^{-i\sigma_\mu k t}\psi_\mu(k) \tag{2.11}$$

with $\sigma_1 = +$ and $\sigma_2 = -$. Eq. (2.9) thus yields in k-space:

$$\begin{aligned}\Delta\mathcal{M} = e^2 \int dk dk' \quad & \langle\psi_1(k)\psi_1^\dagger(k')\rangle_{\varphi_1}\langle\psi_2^\dagger(-k)\psi_2(-k')\rangle_{\varphi_2} \\ - \quad & \langle\psi_1(k)\psi_1^\dagger(k')\rangle_0\langle\psi_2^\dagger(-k)\psi_2(-k')\rangle_0 \\ + \quad & \langle\psi_1^\dagger(k)\psi_1(k')\rangle_{\varphi_1}\langle\psi_2(-k)\psi_2^\dagger(-k')\rangle_{\varphi_2} \\ - \quad & \langle\psi_1^\dagger(k)\psi_1(k')\rangle_0\langle\psi_2(-k)\psi_2^\dagger(-k')\rangle_0 .\end{aligned} \tag{2.12}$$

where the subscript φ_μ denotes averaging over the prepared state $|\varphi_\mu\rangle$, and the zero subscript denotes averaging over the FS $|0\rangle$.

One convenient object that we can introduce at this stage is the excess coherence function, namely:

$$\phi_\mu(k,k') = \langle\psi_\mu^\dagger(k)\psi_\mu(k')\rangle_{\varphi_\mu} - \langle\psi_\mu^\dagger(k)\psi_\mu(k')\rangle_0 \tag{2.13}$$

With this notation, the mixed term takes the form:

$$\begin{aligned}\Delta\mathcal{M} = e^2 \int dk dk' \quad & \phi_1(k,k')\left(\langle\psi_2(-k)\psi_2^\dagger(-k')\rangle_0 - \langle\psi_2^\dagger(-k')\psi_2(-k)\rangle_0\right) \\ + \quad & \phi_2(k,k')\left(\langle\psi_1(-k)\psi_1^\dagger(-k')\rangle_0 - \langle\psi_1^\dagger(-k')\psi_1(-k)\rangle_0\right) \\ - \quad & 2\phi_1(k,k')\phi_2(-k',k) .\end{aligned} \tag{2.14}$$

Noting $f_\mu(k)$ the Fermi distribution on channel μ, we have:

$$\begin{aligned}\Delta\mathcal{M} = e^2\Bigg\{\int_0^\infty dk\phi_1(k,k)\left[1-2f_2(-k)\right] + \int_{-\infty}^0 dk\phi_2(k,k)\left[1-2f_1(-k)\right] \\ - \int_0^\infty dkdk'\phi_1(k,k')\phi_2(-k',-k)\Bigg\} .\end{aligned} \tag{2.15}$$

On channel 1, the Fermi distribution is given by $f_1(k) = f_k = 1/(1+e^{(k-k_F)/\Theta})$, and on channel 2, $f_2(k) = f_{-k}$.

2.2.3 *Auto-correlations*

Substituting the expression for the currents on the incoming branches given by eq. (2.4), one can rewrite the auto-correlations that enter eq. (2.10) as:

$$\begin{aligned}\Delta S_{\mu\mu} = e^2 \int dt dt' \quad & \langle : \psi_\mu^\dagger(0,t)\psi_\mu(0,t) :: \psi_\mu^\dagger(0,t')\psi_\mu(0,t') :\rangle_{\varphi_\mu} \\ - \quad & \langle : \psi_\mu^\dagger(0,t)\psi_\mu(0,t) :\rangle_{\varphi_\mu}\langle : \psi_\mu^\dagger(0,t')\psi_\mu(0,t') :\rangle_{\varphi_\mu} \\ - \quad & \langle : \psi_\mu^\dagger(0,t)\psi_\mu(0,t) :: \psi_\mu^\dagger(0,t')\psi_\mu(0,t') :\rangle_0 \\ + \quad & \langle : \psi_\mu^\dagger(0,t)\psi_\mu(0,t) :\rangle_0\langle : \psi_\mu^\dagger(0,t')\psi_\mu(0,t') :\rangle_0 \end{aligned} \tag{2.16}$$

Writing explicitly the normal ordering prescription and turning to k-space, this is further simplified as:

$$\begin{aligned}\Delta S_{\mu\mu} = e^2 \int dk dk' \quad & \langle \psi_\mu^\dagger(k)\psi_\mu(k)\psi_\mu^\dagger(k')\psi_\mu(k')\rangle_{\varphi_\mu} \\ - \quad & \langle \psi_\mu^\dagger(k)\psi_\mu(k)\rangle_{\varphi_\mu}\langle \psi_\mu^\dagger(k')\psi_\mu(k')\rangle_{\varphi_\mu} \\ - \quad & \langle \psi_\mu^\dagger(k)\psi_\mu(k')\rangle_0\langle \psi_\mu(k)\psi_\mu^\dagger(k')\rangle_0 \end{aligned} \tag{2.17}$$

In order to go further at this stage, the prepared state $|\varphi_\mu\rangle$ has to be specified. We suppose that one electron is injected on each incoming edge, which allows us to expand the 4-fermion correlator, using Wick's theorem:

$$\begin{aligned} & \langle \psi_\mu^\dagger(k)\psi_\mu(k)\psi_\mu^\dagger(k')\psi_\mu(k')\rangle_{\varphi_\mu} \\ = & \int \frac{dk_1 dk_2}{2\pi} \varphi_\mu^e(k_1)\varphi_\mu^e(k_2)^* \Big[\langle \psi_\mu(k_2)\psi_\mu^\dagger(k)\rangle_0\langle \psi_\mu(k)\psi_\mu^\dagger(k')\rangle_0\langle \psi_\mu(k')\psi_\mu^\dagger(k_1)\rangle_0 \\ + & \langle \psi_\mu(k_2)\psi_\mu^\dagger(k)\rangle_0\langle \psi_\mu(k)\psi_\mu^\dagger(k_1)\rangle_0\langle \psi_\mu^\dagger(k')\psi_\mu(k')\rangle_0 \\ + & \langle \psi_\mu^\dagger(k)\psi_\mu(k)\rangle_0\langle \psi_\mu(k_2)\psi_\mu^\dagger(k')\rangle_0\langle \psi_\mu(k')\psi_\mu^\dagger(k_1)\rangle_0 \\ + & \langle \psi_\mu^\dagger(k)\psi_\mu(k)\rangle_0\langle \psi_\mu(k_2)\psi_\mu^\dagger(k_1)\rangle_0\langle \psi_\mu^\dagger(k')\psi_\mu(k')\rangle_0 \\ + & \langle \psi_\mu^\dagger(k)\psi_\mu(k')\rangle_0\langle \psi_\mu(k_2)\psi_\mu^\dagger(k_1)\rangle_0\langle \psi_\mu(k)\psi_\mu^\dagger(k')\rangle_0 \\ - & \langle \psi_\mu^\dagger(k)\psi_\mu(k')\rangle_0\langle \psi_\mu(k_2)\psi_\mu^\dagger(k')\rangle_0\langle \psi_\mu(k)\psi_\mu^\dagger(k_1)\rangle_0 \Big] \end{aligned} \tag{2.18}$$

Similarly, for the 2-fermion correlator, we get:

$$\begin{aligned} & \langle \psi_\mu^\dagger(k)\psi_\mu(k')\rangle_{\varphi_\mu} \\ = & \langle \psi_\mu^\dagger(k)\psi_\mu(k')\rangle_0 \\ + & \int \frac{dk_1 dk_2}{2\pi} \varphi_\mu^e(k_1)\varphi_\mu^e(k_2)^* \langle \psi_\mu(k_2)\psi_\mu^\dagger(k)\rangle_0\langle \psi_\mu(k')\psi_\mu^\dagger(k_1)\rangle_0 \end{aligned} \tag{2.19}$$

from which one can directly read the excess coherence function expression:

$$\phi_\mu(k,k') = \int \frac{dk_1 dk_2}{2\pi} \varphi_\mu^e(k_1)\varphi_\mu^e(k_2)^* \langle \psi_\mu(k_2)\psi_\mu^\dagger(k)\rangle_0\langle \psi_\mu(k')\psi_\mu^\dagger(k_1)\rangle_0 \tag{2.20}$$

The auto-correlation then takes the simple form:

$$\Delta S_{\mu\mu} = e^2\left[\int dk\phi_\mu(k,k)(1-2f_\mu(k)) - \left(\int dk\phi_\mu(k,k)\right)^2\right] \tag{2.21}$$

Combined with the mixed term and reminding that $f_1(k) = f_2(-k)$, the cross-correlation simplifies into:

$$\begin{aligned}\Delta S_{12}^{\text{out}} = -e^2\mathcal{R}\mathcal{T}\Bigg\{&\left(\int_0^\infty dk\phi_1(k,k)\right)^2 + \left(\int_{-\infty}^0 dk\phi_2(k,k)\right)^2 \\ &-2\int_0^\infty dkdk'\phi_1(k,k')\phi_2(-k',-k)\Bigg\}\end{aligned} \tag{2.22}$$

Substituting the expression for ϕ_μ, one finally has:

$$\begin{aligned}\Delta S_{12}^{\text{out}} = -e^2\mathcal{R}\mathcal{T}\Bigg\{&\left(\int_0^\infty \frac{dk}{2\pi}|\varphi_1^e(k)|^2(1-f_k)^2\right)^2 \\ &+\left(\int_{-\infty}^0 \frac{dk}{2\pi}|\varphi_2^e(k)|^2(1-f_{-k})^2\right)^2 \\ &-2\int_0^\infty \frac{dkdk'}{4\pi^2}\varphi_1^e(k')\varphi_1^e(k)^*\varphi_2^e(-k)\varphi_2^e(-k')^*(1-f_k)^2(1-f_{k'})^2\Bigg\}\end{aligned} \tag{2.23}$$

This expression is still fully general: the temperature is taken into account by the Fermi distribution f_k and any kind of electronic wave-packet φ_μ^e can be considered, though the exponential ones are the most relevant. Moreover, either one or two single electron injections can be considered by setting a wave-packet to zero in order to mimic an emitter being switched off. Thus, both the HBT and HOM setups are described by this formula.

2.3 RESULTS

2.3.1 *Electron-electron collisions*

First, we consider the case of single electron injection, either on one or both incoming arms.

2.3.1.1 *Hanbury Brown and Twiss experiment*

Consider here the case of the injection of a single electron on the right incoming branch: $|\Psi\rangle = |\varphi_1\rangle \otimes |0\rangle$ with $|\varphi_1\rangle$ given by eq. (2.1). Our previous result eq. (2.23) still applies, but only the first term contributes as $\varphi_2^e = 0$. Let us now note $\varphi_1^e(k) = \varphi^e(k)$. Writing explicitly the normalization condition $1 = \langle\varphi_1|\varphi_1\rangle = \int dk/(2\pi)|\varphi^e(k)|^2(1-f_k)$, one has:

$$\begin{aligned} S^{\mathrm{HBT}} &= -e^2\mathcal{R}\mathcal{T}\left(\int_0^\infty \frac{dk}{2\pi}|\varphi^e(k)|^2(1-f_k)^2\right)^2 \\ &= -e^2\mathcal{R}\mathcal{T}\left(1-\int_0^\infty \frac{dk}{2\pi}|\varphi^e(k)|^2 f_k(1-f_k)\right)^2 \end{aligned} \tag{2.24}$$

Notice first that at zero temperature, the final result reduces to a constant as $f_k(1-f_k) = 0$. This zero temperature noise is completely independent of the shape of the injected wave-packet and is a signature of the random nature of partitioning at the QPC. At finite temperature, the HBT contribution drops as the temperature is increased, since $f_k(1-f_k)$ increases. The reduction factor depends strongly on the energetic content of the wave-packet, it indeed scans the overlap between $\varphi^e(k)$ and $f_k(1-f_k)$. Consequently, the more weight there is near the Fermi energy, the quicker the decrease. For example, the noise is much lower in the resonant emission regime than in the optimal emission regime (see section 2.1.1).

Actually, we are here probing anti-bunching between the injected electron and thermal excitations from the FS, incoming from the other arm. In this sense, the HBT experiment at finite temperature can be viewed as a specific case of the HOM interferometer, in which one single electron injected above the FS in one arm interferes with the incoming FS of the other arm. Furthermore, this anti-bunching effect provides a powerful tool to probe the energy distribution of the excitations produced by the source, as the Fermi energy distribution at thermal equilibrium is known. Thus, the HBT interferometry can also be used as a tomography protocol, where the energy distribution of the emitted particle is recovered, knowing its overlap with thermal excitations.

2.3.1.2 *Hong Ou Mandel experiment*

Another electron is now injected on the left incoming arm. It is identical to the right moving one, except that it is injected with a time delay δT:

$$\varphi_2^e(k) = \varphi^e(-k)e^{-ik\delta T} \tag{2.25}$$

Once again, the noise is obtained from eq. (2.23):

$$\frac{S^{\mathrm{HOM}}(\delta T)}{2S^{\mathrm{HBT}}} = 1 - \left| \frac{\int_0^\infty dk |\varphi^e(k)|^2 e^{-ik\delta T}(1-f_k)^2}{\int_0^\infty dk |\varphi^e(k)|^2 (1-f_k)^2} \right|^2 \tag{2.26}$$

Eq. (2.26) shows immediately that when the two identical electrons reach the QPC simultaneously ($\delta T = 0$), the noise is zero as the ratio entering the equation gives one. This is an effect of Fermi statistics. Insofar as it is forbidden by the Pauli principle for two fermions to be superimposed in the same state, the two outgoing electrons are compelled to exit in different channels. Consequently, the random character of partitioning is completely suppressed and a noiseless process is recovered. On the other hand, for large values of δT (much larger than the inverse of the typical width of $\varphi^e(k)$), the second term in eq. (2.26) vanishes. The noise is then given by $2S^{\mathrm{HBT}}$, the sum of the noise of the two electrons taken independently, as the two impinging electrons are partitioned one after the other.

At low temperature, when the wavepacket $\varphi^e(k)$ has weight above the Fermi level only, the noise can be simplified further:

$$\frac{S^{\mathrm{HOM}}(\delta T)}{2S^{\mathrm{HBT}}} = 1 - \left| \int dx\, \varphi^e(x)\, \varphi^e(x+\delta T)^* \right|^2 . \tag{2.27}$$

This expression is reminiscent of the one obtained in optics, where the shape of the HOM dip is given by the self-convolution of the photon wave-packet [40].

Eq. (2.26) and (2.27) are easily generalized to the case of two different wave-packets, for example $\varphi_2^e(k) \neq \varphi^e(-k)$. Specific formulas of the HOM dip can be obtained analytically for different shapes of wave-packets. As justified earlier (sec. 2.1.1.2), we concentrate here on Lorentzian wave-packets in energy space $\varphi_\Gamma^e(k) = \sqrt{\Gamma/\pi}/\left[(k-k_0)+i\Gamma\right]$. This situation corresponds to the emission by the discrete level of a quantum dot at energy k_0, as found in the single-electron emitter. The Lorentzian shape of the emitted electron is reminiscent of the Lorentzian density of state of the dot energy levels (see fig. 2.2 and 2.3), as they are broadened by the coupling to the linear edge state. The real space profile of this wave-packet is exponential (see Fig 2.5): $\varphi_\Gamma^e(x) = \sqrt{2\Gamma} e^{ik_0 x} e^{\Gamma x}\theta(-x)$ where $\theta(x)$ is the Heavyside function. The noise at zero temperature, for the case of two identical Lorentzian wave-packets, reads:

$$\frac{S^{\mathrm{HOM}}(\delta T)}{2S^{\mathrm{HBT}}} = 1 - e^{-2\Gamma|\delta T|} \tag{2.28}$$

when wave-packet 2 reaches the QPC at a time δT after wave-packet 1. The contrast of the HOM dip $\eta = 1 - S^{\mathrm{HOM}}(0)/(2S^{\mathrm{HBT}}) = 1$ then reaches its maximum. This maximal contrast signals a perfect degree of indistinguishability between the interfering electrons, which were indeed chosen with similar parameters. The width of this Pauli dip is also given by the inverse energy width of the wave-packets $1/\Gamma$, or equivalently by their escape time τ_e (see discussion section 2.1.1.2).

The case of two Lorentzian wave-packets, centered at the same k_0 but with different widths $\Gamma_{1,2}$ can also be explored. The noise is again obtained from eq. (2.23), replacing carefully the wave-packets expressions:

$$\frac{S^{\mathrm{HOM}}(\delta T)}{2S^{\mathrm{HBT}}} = 1 - \frac{4\Gamma_1\Gamma_2}{(\Gamma_1+\Gamma_2)^2}\Big[\theta(\delta T)e^{-2\Gamma_1\delta T} + \theta(-\delta T)e^{2\Gamma_2\delta T}\Big] \tag{2.29}$$

A remarkable feature of this HOM dip is its asymmetry: it has an exponential behavior, with different time constants depending on the sign of δT. The exponential decrease of each side of the dip is governed by the inverse energy width of one packet. Furthermore, the contrast of the HOM dip $\eta = 4\Gamma_1\Gamma_2/(\Gamma_1+\Gamma_2)^2$ is smaller than 1, which reflects the fact that the two electrons are not identical. Indeed, the degree of indistinguishability between the colliding electrons has been reduced by detuning their energy widths. This contrast is all the more small, since $|\Gamma_1 - \Gamma_2|$ is increased.

For arbitrary wave-packets, eq. (2.27) also shows that the asymmetry of the HOM dip is possible only if the wave-packets in real space have no mirror symmetry. This is clearly the case for exponential wave-packets, but it is not true for instance for Lorentzians in real space. The asymmetry in the HOM dip thus provides information on the spatial symmetry of the electronic wave-packets.

We now compare eq. (2.29) with the numerical results of a Floquet calculation. It includes the emission process from the single-electron emitters, contrary to the previous analytical calculations. Consequently, the single electron sources parameters have to be carefully set. First, the temperature is chosen to be small ($\Theta = 0.01\Delta$) and the period of the applied voltage $V_{\mathrm{exc}}(t)$ of the emitters is $T_0 = 400\hbar/\Delta$. The emitted wave-packets energy widths are tuned by the transparencies of the dots. In fig. 2.8, both capacitors are processed in the optimal emission regime (section 2.1.1), in which it is known that the electron escape time as a function of the transparency $\mathcal{T}$ is given by $\tau_e = (2\pi/\Delta)(1/\mathcal{T} - 1/2)$ [77]. The lower the transparency of the dot is, the longer it takes for the electron to exit, and the broader the wave-packet is. Consequently, we use this value of the emission time (with $2\Gamma = \tau_e^{-1}$) to plot the analytical predictions from eq. (2.29) (dot-dashed curves). The upper panel shows the symmetric case, where the two emitters have identical parameters. For three different transparencies, we observe three different HOM dips with a maximum contrast $\eta = 1$ (the minimum value is 0 at $\delta T = 0$). The dip is broader for lower emitter transparency, which signals a broader wave-packet. The agreement between the numerical and analytical predictions is

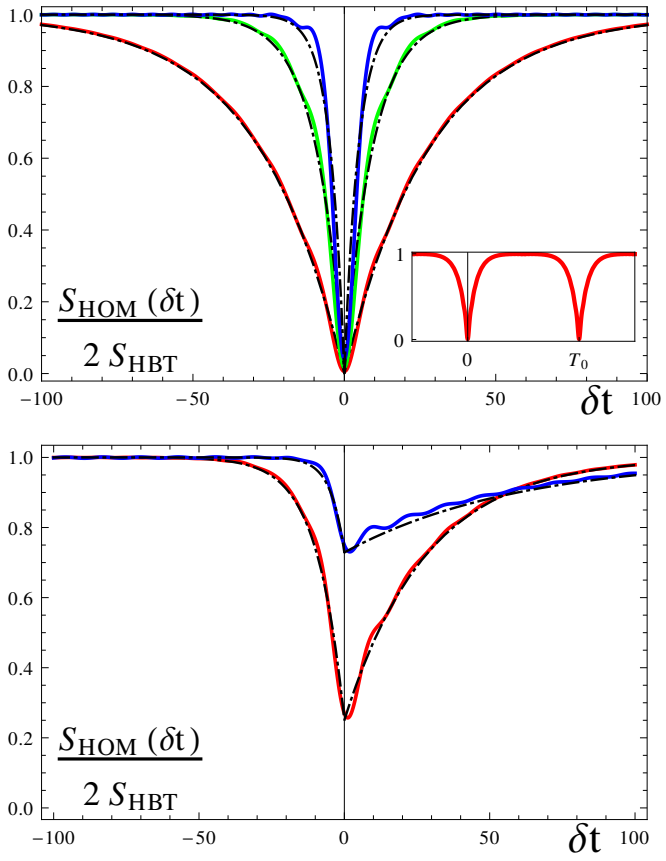

Figure 2.8: HOM dips as a function of the time difference δT (in units of $\hbar/\Delta$), obtained from Floquet scattering matrix formalism in the optimal emission regime (full) and analytical predictions of eq. (2.29) for exponential wavepackets (dot-dashed). Upper panel: symmetric case, with emitter transparencies $\mathcal{T} = 0.2$, 0.5 and 0.8 (from outer to inner curve). Inset: dips for $\mathcal{T} = 0.2$ on two periods of the applied voltage. Lower panel: asymmetric case, with transparencies $\mathcal{T}_1 = 0.2$, $\mathcal{T}_2 = 0.5$ (bottom curve) and $\mathcal{T}_1 = 0.1$, $\mathcal{T}_2 = 0.8$ (top curve).

excellent, without any fitting parameters, especially in the low transparency regime where it is known that true single electron emission is achieved [64**?**]. In the asymmetric case (lower panel), as the emitted electrons are not identical, the contrast is smaller than 1, and the HOM dips are asymmetric. The agreement with the analytical prediction is again very good, both for the asymmetric shapes and for the value of the contrast.

The slight oscillations in Floquet calculations arise from the non-perfect character of the drive voltage. Indeed, experimentally, it is made out of a finite number of harmonics, preventing V_g to be ideally square-shaped (see fig. 2.2, top panel). This constraint is taken into account in the Floquet calculation and results in small oscillations, account for by the numerical approach.

2.3.2 *Electron-hole collisions*

The results presented so far are quite similar to those obtained with photons in optics. However, the existence of the FS allows to create holes in it, which have no counterpart for photons. We study two-particle interferences of electrons and holes, injecting one electron in branch 1, with a state given by eq. (2.1), and one hole injected in branch 2, with a state given by eq. (2.2).

Just as previously, the fermion correlators involved in the expression of the noise, given by eq. (2.17), can be expanded using Wick's theorem, as the prepared state $|\Psi\rangle = |\varphi_1\rangle \otimes |\varphi_2\rangle$ is specified. A remarkable feature is that eq. (2.21) and (2.22), which express the auto- and cross-correlation in terms of the excess coherence functions, remain valid. Only the definition of the excess coherence function on channel 2 is modified, as:

$$\phi_2(k,k') = -\int \frac{dk_1 dk_2}{2\pi} \varphi_2^h(k_1)\varphi_2^h(k_2)^* \langle \psi_2^\dagger(k_2)\psi_2(k')\rangle_0 \langle \psi_2^\dagger(k)\psi_2(k_1)\rangle_0 \quad (2.30)$$

Finally, when substituting the expressions for ϕ_1 and ϕ_2 in the cross-correlation, one gets:

$$\begin{aligned} \Delta S_{12}^{\text{out}} &= -e^2\mathcal{R}\mathcal{T}\left\{\left(\int_0^\infty \frac{dk}{2\pi}|\varphi_1^e(k)|^2(1-f_k)^2\right)^2\right. \\ &+ \left(\int_0^\infty \frac{dk}{2\pi}|\varphi_2^h(k)|^2 f_{-k}^2\right)^2 \\ &+ \left. 2\int_0^\infty \frac{dkdk'}{4\pi^2}\varphi_1^e(k')\varphi_1^e(k)^*\varphi_2^h(k)\varphi_2^h(k')^*(1-f_k)(1-f_{k'})f_{-k}f_{-k'}\right\} \end{aligned} \quad (2.31)$$

Like eq. (2.23), this result is quite general insofar as the temperature, and the electron and hole wave-packets can be modified without preventing the formula from being valid. Furthermore, three different setups can be described by eq. (2.31): the HBT setup with either an electron or a hole being injected, and electron hole HOM interferometry.

2.3.2.1 *Hanbury Brown and Twiss experiment*

For the physics to be the most transparent, we consider the electron-hole symmetric case: $\varphi^e(k) = \varphi^h(-k)$. Thus $\varphi_2^h(k) = \varphi^h(-k)e^{-ik\delta T} = \varphi^e(k)e^{-ik\delta T}$, where the hole on channel 2 is injected with a time delay δT with respect to the electron injection on channel 1. Switching off the electron source on chan-

nel 1, we recover the same noise as the one produced by the partitioning of one electron.

$$\begin{aligned}\Delta S_{12}^{\text{out}} &= -e^2\mathcal{R}\mathcal{T}\left(\int_0^\infty \frac{dk}{2\pi}|\varphi_2^h(k)|^2 f_{-k}^2\right)^2 \\ &= -e^2\mathcal{R}\mathcal{T}\left(\int_0^\infty \frac{dk}{2\pi}|\varphi^e(k)|^2(1-f_k)^2\right)^2 \\ &= S^{\text{HBT}} \end{aligned} \tag{2.32}$$

The noise due to the partitioning of a single charge is independent of its sign. At non zero temperature, probing anti-bunching between one electron and the Fermi distribution f_k is equivalent to probing anti-bunching between the symmetric hole and $(1-f_k)$. The system is indeed electron-hole symmetric and both species obey fermionic statistics.

2.3.2.2 *Hong Ou Mandel experiment*

Analogously to the previous noise calculation, we have:

$$\frac{S^{\text{HOM}}(\delta T)}{2S^{\text{HBT}}} = 1 + \left|\frac{\int_0^\infty dk\,\varphi^e(k)\varphi^h(k)^* e^{-ik\delta T} f_k(1-f_k)}{\int_0^\infty dk\,|\varphi^e(k)|^2(1-f_k)^2}\right|^2 \tag{2.33}$$

Comparing eq. (2.33) with eq. (2.26), we notice important changes. First, the interferences contribute now with a positive sign to the noise, i.e. the opposite of the electron-electron case. Electron-hole interferences produce a "HOM peak" rather than a dip. Second, the value of this peak depends on the overlap of the electron and the hole wavepackets ($\varphi^e(k)\varphi^h(k)^*$), times the Fermi product $f_k(1-f_k)$. This peak thus vanishes as $\Theta \to 0$ since it requires a significant overlap between electron and hole wave-packets, a situation which only happens in an energy range $\sim \Theta$ around k_F, where electronic states are neither fully occupied nor empty. Finally, it is clear from eq. (2.33) that the value of this peak is typically smaller than one, and can at most be one, when $\varphi^e(k) = \varphi^h(k)$.

In order to enhance this overlap between the electron and hole wave-packets, one can work in the resonant emission regime. Indeed, in this regime, both electrons and holes are emitted for some part at the Fermi energy (see fig. 2.3).

We now consider the observation of these electron-hole interferences with realistic electron emitters using Floquet scattering theory. The simultaneous arrival of an electron and a hole at the QPC happens quite naturally in this device. Indeed, each emitter emits periodically an electron and then, half a period T_0 later, a hole. If one applies a time-shift $T_0/2$ between the two emitters, one expects that an electron from one emitter, and one hole from the other emitter, will interfere at the QPC. The optimal emission regime of Fig. 2.8 does not show any sign of electron-hole interference, as can be seen in the inset of this figure (no peak at $\delta T = T_0/2$). This is easily understood from eq. (2.33), as the electron (hole) wave-packet is a Lorentzian peaked at energy

$\Delta/2$ ($-\Delta/2$), and the overlap of the two wave-packets is negligible, even in the totally transparent case.

We consider two regimes where there is a significant overlap between electron and hole wave-packets, leading to observable electron-hole peak. In both cases, we use a small but non-zero temperature $\Theta = 0.1\Delta$, compatible with existing experimental values (typically $\Delta \simeq 2$K, and $\Theta \simeq 150$ mK [14]).

The first regime is the resonant emission regime, where the electron and the hole have a large part of their weight close to the Fermi energy, and one can expect a significant electron and hole overlap. In fact, one can smoothly vary between the optimal and resonant emission regimes, by shifting the excitation drive by ϵ. In the resonant regime, $\epsilon = 0$ and the electron emission occurs for the main part at $E_F + \epsilon = E_F$ (see step ② in fig. 2.3). In the optimal regime, $\epsilon = \Delta/2$ and the electron is emitted at energy $E_F + \epsilon = E_F + \Delta/2$ (see step ② in fig. 2.2). The results for the HOM noise are shown in the upper panel of fig. 2.9, which have been computed for an emitter with transparency $\mathcal{T} = 0.2$. The different curves span the different cases between optimal emission (negligible peak at $\delta T = T_0/2$) and resonant emission (largest peak $\delta T = T_0/2$). The shape of this peak is clearly the same as the HOM dip, and it is due to the exponential profile of the wave-packets in real space.

In the second regime, the applied voltage has a sinusoidal dependence ($V_{\text{exc}}(t) = (\Delta/2)\sin(2\pi t/T_0)$), rather than steps. The main emitting dot level now has a time dependence of the form $\epsilon \sim E_F + V_{\text{exc}}(t)$. Such a profile forces the emitting level to spend a non-negligible amount of time near the Fermi energy. The emitted electron and hole energy distributions thus have substantial weight close to E_F. This weight increases with the dot transparency [14], and one can thus expect that the HOM peak grows larger for transparencies closer to 1. The result for the HOM noise in this case is shown in the bottom panel of fig. 2.9 for different values of $\mathcal{T}$. We observe a small positive peak at $\delta T = T_0/2 = 200\hbar/\Delta$ for the smallest transparency, which increases as $\mathcal{T}$ is increased. For a dot totally transparent ($\mathcal{T} = 1$), the peak becomes as large as the HOM dip. Note that, in the two panels of fig. 2.9, the different curves have been scaled by the corresponding value of HBT noise, which explains why all dips have a depth 1. The non-scaled values of S_{HOM} vary at most by a factor 2 for the upper panel, and a factor 6 for the bottom one.

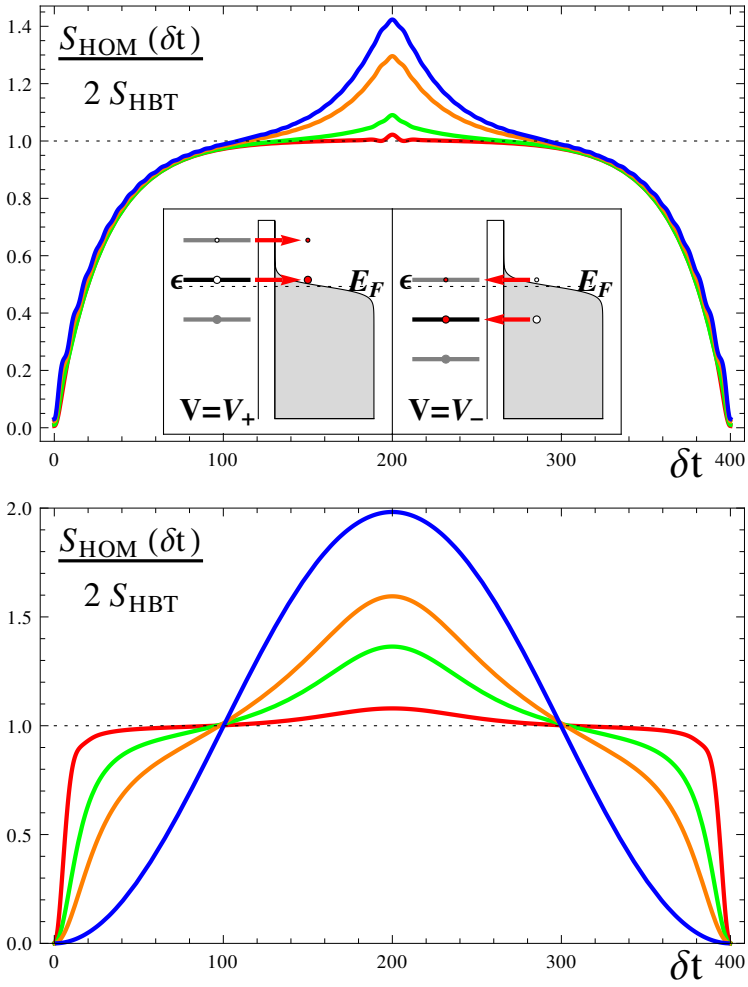

Figure 2.9: Top panel: HOM peak for electron-hole collision, for a square voltage drive at different level positions. Inset: electron and hole emission process for the two positions of the dot level, with level position parametrized by ϵ with respect to E_F. The curves correspond to $\epsilon = 0.5, 0.4, 0.25$ and 0 (in units of Δ) from the smallest to the largest peak. Bottom panel: same for a sinusoidal voltage drive at different transparencies, $\mathcal{T} = 0.2, 0.5, 0.7$ and 1.0 (smaller to larger peak). $\Theta = 0.1\Delta$ in both panels.

2.3.3 *Conclusion*

In conclusion, mesoscopic capacitors now allow to implement the electronic analogs of the HBT and HOM quantum optics experiments, using either electrons, holes or both instead of photons. In any case, these setups probe two particle interferences.

In the HBT experiment, an injected electron (hole) anti-bunches on the QPC with thermal excitations from the other incoming arm. At zero temperature, this effect is killed and the maximum value for the HBT noise is recovered. This value is classical and due to the random nature of scattering at the QPC. At finite temperature, the noise is reduced by a factor which strongly depends on the energy contents of the emitted particle. A wave-packet which has substantial weight near E_F will overlap with excitations of the same energy, leading to a decreased noise.

The fermionic HOM interferometry can also be performed. When two electrons collide on the QPC, the zero-frequency current correlations exhibit a dip as a function of the time delay between arrivals at the QPC. The contrast of this Pauli dip is a probing tool of the degree of indistinguishability between colliding electrons. A maximum contrast is recovered for identical electrons, whereas it is reduced when they are more distinguishable, for example when they have different widths in energy. Through analytic calculations, we could also relate the shape of the dip to the properties of the electron wave-packets colliding. For example, the wave-packets width can be extracted from the dip shape in the case of exponential wave-packets, similarly an asymmetric dip signals that the injected electrons are asymmetric and that the wave-packets have no mirror symmetry in real space.

Electron hole interferences can also be probed by an HOM electronic interferometer. They produce a peak, which vanishes at zero-temperature and can be enhanced by properly tuning the excitation voltage drives of the capacitors. It should be observable in future experimental setups involving two emitters.

Finally, our analytical calculations showed good agreement with the more realistic treatment of the single-electron emitter via Floquet scattering theory, which also allows to consider more experimentally relevant situations. Interactions have been included here in the statistical sense only.

Part II

SWITCHING ON INTERACTIONS

In the previous chapter, electron-electron interactions have been neglected, insofar as the propagation along the channels was assumed to be interaction free and dissipation less. However, due to their one-dimensional nature, quantum Hall edge channels are prone to emphasize interaction effects. In one dimensional systems, the motion of an electron interacting with its neighbors strongly affects the latter, so that the Fermi liquid paradigm does not hold. Contrary to two and three dimensional systems, the picture of quasi-free quasi-particles is not accurate. It is replaced by the Luttinger liquid theory, that relies on bosonic collective excitations. In the IQHE, at filling factor higher than one, transport occurs along several co-propagating channels on each edge. As they are very close by one another, they are coupled by inter-channel Coulomb interaction, which leads to the appearance of new collective propagation modes.

Various experiments have been carried out to investigate the coupling between edge channels and their effect on the relaxation and decoherence of electronic excitations. This coupling has been shown to be responsible for the loss of the visibility of the interference pattern in Mach-Zehnder interferometers at filling factor $\nu = 2$ [83, 73, 82]. In this case, the coupling of the external channel to the neighboring one leads to decoherence as information on the quantum state generated in the outer channel is capacitively transferred to the inner one acting as the environment. Indeed, at $\nu > 1$, interactions dramatically change the nature of excitations, leading to energy exchange between the channels and to charge fractionalization [72, 12, 57, 48, 70, 6, 87, 61, 24]. The influence of inter-channel coupling on the energy relaxation of out of equilibrium excitations emitted in the outer edge channel has also been probed [6, 87] at filling factor $\nu = 2$, using a quantum dot as an energy filter. These results have shown that coherence is lost and energy relaxes on a typical length of a few microns. Numerous theoretical works have successfully interpreted decoherence in interferometers [88, 58, 49] and energy relaxation along propagation [24, 61, 48, 57] as stemming from inter-channel Coulomb interactions.

The puzzle with the recent electronic HOM experiment [15], which was performed at a filling factor $\nu > 1$, is that the Pauli dip does not vanish as expected (see fig. 2.10). The purpose of the present part is to provide a theoretical framework for the experiment and to show that the interaction between quantum channels is responsible for the observed effect.

In Chapter 3, the Tomonaga Luttinger liquid (TLL) theory, which allows to interactions into account for one-dimensional electronic transport, is introduced, as well as the bosonization technique, which enables to solve the model. In Chapter 4, the model aimed at reproducing the experiment is presented.

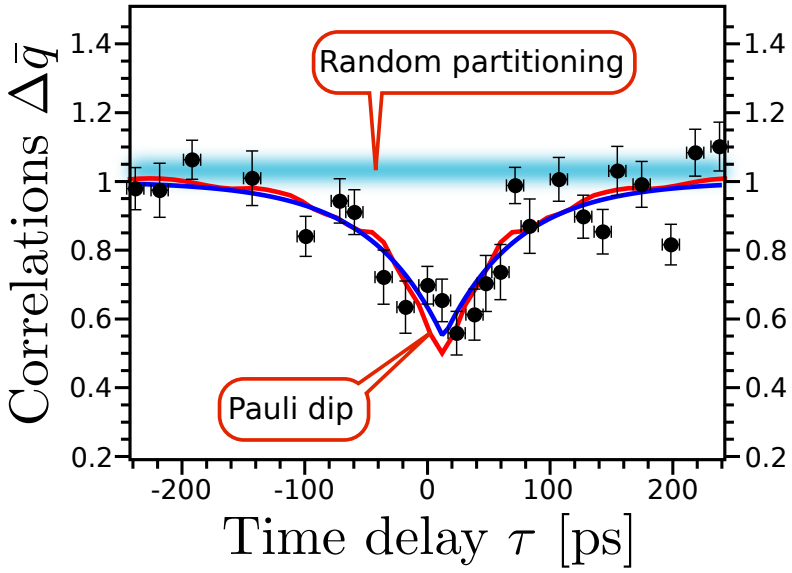

Figure 2.10: Taken from [15]. Excess HOM noise, normalized by the HBT noise: $\Delta\bar{q} = S_{\mathrm{HOM}}(\tau)/(2S_{\mathrm{HBT}})$. The blurry blue line represents the sum of the partition noise of both sources. The blue trace is an exponential fit by $\Delta q = 1 - \gamma e^{-|t-\tau_0|}$. The red trace is obtained using Floquet scattering theory, with an ad hoc fitting parameter.

3

ELECTRONS IN ONE DIMENSION

3.1 INTRODUCTION

Usually, in two and three dimensions, metals are well described by the Fermi liquid theory [52, 51, 74]. In this model the "bare electrons" are "dressed" by interactions and the problem can be addressed in terms of free quasi-particles. These quasi-particles do not interact with each other and have the same quantum numbers as the free particles. Though the energy distribution might be changed, it remains quite similar to the Fermi distribution, in the sense that it is still discontinuous at the Fermi energy at zero temperature. Thus, the quasi-particles are considered to be fermionic. On the contrary, some properties -such as the specific heat capacity or even the mass- are renormalized by interactions. But at low dimensions, the physics is dramatically affected by the dimensionality. For example, in an one-dimensional (spinless) lattice, with one electron on each site, the hopping of an electron from one site to the neighboring site forces every electron to jump forward. The Pauli principle forbids two electrons to be superimposed in the same state, thus each site can be at maximum singly occupied. One electron hopping thus causes every other electrons hopping. Consequently, the only possible excitations in such a system are collective modes, which differ drastically from the original fermions.

During the fifties and sixties, new models were suggested by Tomonaga [89] and then Luttinger [62] to describe a one-dimensional interacting electron gas, that is to say a quantum wire. It was solved by Mattis and Lieb [22]. The underlying idea of those models is to linearize the spectrum in the vicinity of the Fermi energy. The new spectrum is then made out of two branches, corresponding to the electrons propagating towards one direction or the other in the wire.

The most striking feature of this model is that the elementary collective electron-hole excitations have a bosonic character. The Hamiltonian can then

be expressed in terms of bosonic fields instead of the original fermionic ones. The point is that in this formulation the Hamiltonian is quadratic, which is crucial in order to compute physical quantities. This technique is called bosonization. Later on, Haldane [37] showed that this model is way more general and can describe any one-dimensional interacting fermions, or even hard-core bosons, as long as the spectrum respects a few conditions. Since then, the TLL theory has been applied to a variety of systems, among which are carbon nanotubes, some organic conductors, or the edge states of the FQHE. In that latter example, a direction of propagation is assigned to each edge state, and the Hamiltonian has only one branch. The TLL is then called chiral.

First, we will give a very brief introduction on the TLL theory, as many review articles are available. The bosonization technique, which enables one to solve that model, will also be introduced. Finally, we will turn to the hydrodynamical model we use to describe the quantum Hall edge states.

Figure 3.1: One-dimensional tight-binding lattice. μ is each site chemical potential, a is the lattice constant and t is the nearest neighbor hopping amplitude.

3.2 TOMONAGA LUTTINGER LIQUID THEORY

Before introducing the TLL theory, let us review the form of the excitation spectra for non-interacting electrons. Electrons on a one-dimensional lattice (see fig. 3.1) can be described by a tight-binding model given by the Hamiltonian [32]:

$$H_{\text{kin}} = -t\sum_n \left[\psi_n^\dagger \psi_{n+1} + h.c.\right] + \mu \sum_n \psi_n^\dagger \psi_n \tag{3.1}$$

where t is the hopping integral between adjacent lattice sites, with lattice constant a. The operator ψ_n annihilates an electron on site n, μ is the chemical potential and $\rho_n = \psi_n^\dagger \psi_n$ is the electron density at the nth lattice site. For the sake of simplicity we have neglected the spin degree of freedom, but it could be simply taken into account. This model has a symmetric energy band, $E(k) = -2t\cos(ka) + \mu$. In the ground state of the free system, all states with momentum $|k| \leq k_F$ are doubly occupied. At any filling of the single-particle states, the dispersion relation in the vicinity of the Fermi level can be linearized, resulting in the spectrum shown in fig. 3.2. The Fermi surface is reduced to two points: $E(k_F) = E(-k_F) = E_F$. This example is very-well suited to apply the TLL theory. Furthermore, it is all the more relevant since edge channels in the IQHE can be modeled as one-dimensional tight-binding chains [43].

We now consider an interacting one-dimensional electron gas. The Hamiltonian describing this system can be divided into its kinetic and interaction contributions, describing respectively the propagation of free electrons and their interactions: $H = H_{\text{kin}} + H_{\text{int}}$. As long as the energy spectrum is symmetric and gapless, the TLL theory can be applied. The main idea is that the system properties at low energy only depend on the states whose energy is close to the Fermi energy. Furthermore, if the temperature is low enough, the thermal fluctuations will also be restricted to the vicinity of the Fermi energy. As we are essentially zooming on the Fermi surface, the spectrum can be linearized around the Fermi energy (see fig. 3.2) in a good approximation. As

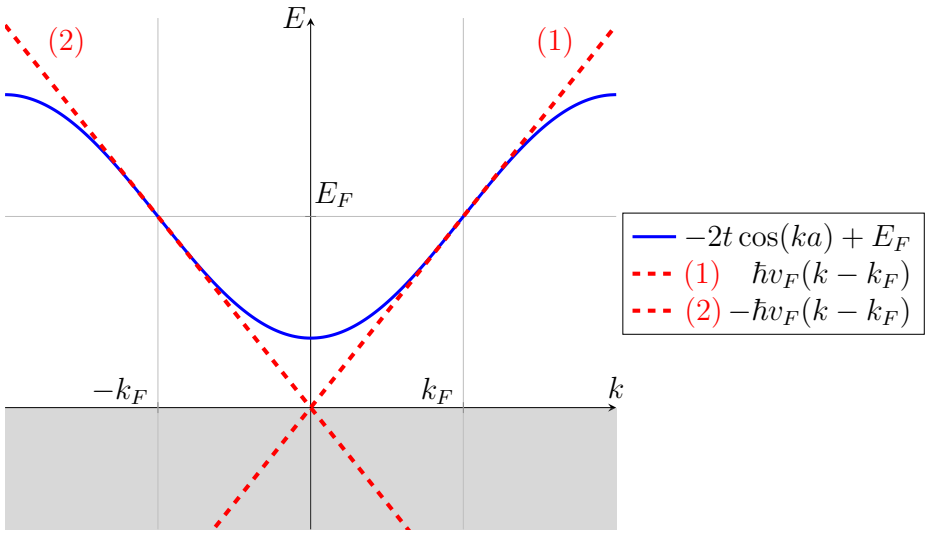

Figure 3.2: Spectrum of the one-dimensional tight-binding model defined by eq. (3.1) with $\mu = E_F$ (plain), and its linearized version near the Fermi energy (dashed). The gray part, corresponding to the negative energy states, is non-physical.

the Fermi surface is composed of two points, two branches are obtained for the linearized spectrum:

$$\begin{aligned} E(k) &= \hbar v_F(k - k_F) \qquad k > 0 \\ E(k) &= -\hbar v_F(k - k_F) \qquad k < 0 \end{aligned} \tag{3.2}$$

As a physical interpretation, a direction of propagation is assigned to each branch. The right branch labeled (1) corresponds to the electrons propagating towards the right ($k > 0$) with the velocity v_F, and the branch labeled (2) corresponds to the left-moving electrons ($k < 0$). This is the Tomonaga model. The TLL approach consists in extending the linearized spectrum to all the values of k: $k < 0$ for the branch (1) and $k > 0$ for the branch (2), colored in gray in fig. 3.2. Thus, an infinite set of virtual states with negative energies has been added to the system. Those are not relevant physically, but the purpose of this addition is to use the so-called bosonization technique. Still, some convergence factors have to be added in order to get rid of the non-physical effects.

From the linearized spectrum given by eq. (3.2), the kinetic part of the Hamiltonian can be obtained:

$$H_{\text{kin}} = \hbar v_F \sum_k k \left(a_{1k}^\dagger a_{1k} - a_{2k}^\dagger a_{2k} \right) \tag{3.3}$$

with $a_{\mu k}$ the electronic annihilation operator on branch $\mu = 1, 2$. The electronic creation and annihilation operators can be obtained in real space by preforming an inverse Fourier transform:

$$\begin{aligned} \psi_\mu(x) &= \frac{1}{\sqrt{L}} \sum_k e^{ikx} a_{\mu k} \\ \psi_\mu^\dagger(x) &= \frac{1}{\sqrt{L}} \sum_k e^{-ikx} a_{\mu k}^\dagger \end{aligned} \tag{3.4}$$

with L the length of the wire. Those operators obey the usual fermionic anticommutation relations:

$$\begin{aligned} \left\{\psi_\mu(x), \psi_{\mu'}^\dagger(x')\right\} &= \delta_{\mu\mu'}\delta(x-x') \\ \left\{\psi_\mu(x), \psi_{\mu'}(x')\right\} &= 0 \end{aligned} \tag{3.5}$$

Thus, in real space the kinetic part of the Hamiltonian reads:

$$H_{\text{kin}} = -i\hbar v_F \int_0^L dx \left(\psi_1^\dagger(x)\partial_x\psi_1(x) - \psi_2^\dagger(x)\partial_x\psi_2(x)\right) \tag{3.6}$$

3.3 BOSONIZATION

3.3.1 *Bosonization identity*

The bosonization procedure consists in expressing the Hamiltonian and all other operators in terms of newly introduced bosonic operators. These operators will obey bosonic statistics, even though they are originally written using fermionic fields.

First, the electronic density operator reads:

$$\rho_\mu(x) = \psi_\mu^\dagger(x)\psi_\mu(x) \tag{3.7}$$

Its k-space expression is obtained via a Fourier transform:

$$\begin{aligned}\rho_\mu(p) &= \frac{1}{\sqrt{L}}\int_0^L dx e^{ipx}\psi_\mu^\dagger(x)\psi_\mu(x)\\ &= \frac{1}{\sqrt{L}}\sum_k a_{\mu,p+k}^\dagger a_{\mu,k}\end{aligned} \tag{3.8}$$

Eq. (3.8) clearly shows that an electronic density excitation of a specific energy is composed of collective electron-hole excitations. All electrons on the considered branch acquire an additional momentum p.

The commutation relations between the density operator and the electronic annihilation operator are easily obtained from eq. (3.5):

$$\left[\psi_\mu(x),\rho_\mu(x')\right] = \delta(x-x')\psi_\mu(x)\,. \tag{3.9}$$

Moreover, the commutation relations of the density with itself are written in k-space:

$$\left[\rho_\mu(k),\rho_\mu(k')\right] = (-1)^\mu\frac{k}{2\pi}\delta_{k,-k'} \tag{3.10}$$

with $\mu = 1,2$. Except for the k factor, these relations look alike bosonic commutation relations. In order to cancel that factor, new operators are introduced:

$$\begin{aligned}b_k^\dagger &= i\sqrt{\frac{2\pi}{|k|}}\Big(\theta(k)\rho_1(k)-\theta(-k)\rho_2(k)\Big)\\ b_k &= i\sqrt{\frac{2\pi}{|k|}}\Big(-\theta(k)\rho_1(-k)+\theta(-k)\rho_2(-k)\Big)\end{aligned} \tag{3.11}$$

Using eq. (3.10), one indeed gets:

$$\begin{aligned}\left[b_k,b_{k'}^\dagger\right] &= \delta_{k,k'}\\ \left[b_k,b_{k'}\right] &= 0\end{aligned} \tag{3.12}$$

These commutation relations are finally truly bosonic. In order to reformulate our problem, we introduce two bosonic Luttinger fields, which are linear superpositions of the electronic density operators or of the bosonic operators we have introduced in eq. (3.11). They read:

$$\begin{aligned}\phi_1(x) &= \frac{1}{\sqrt{2L}}\sum_{k>0}\frac{e^{-ak/2}}{\sqrt{k}}\left[b_k^\dagger e^{-ikx}+b_k e^{ikx}\right]\\ \phi_2(x) &= \frac{1}{\sqrt{2L}}\sum_{k<0}\frac{e^{ak/2}}{\sqrt{-k}}\left[b_k^\dagger e^{-ikx}+b_k e^{ikx}\right]\end{aligned} \tag{3.13}$$

with a a constant which will tend to zero at the end of the calculation. This convergence factor regularizes the negative energy states introduced section 3.2. It is obvious from the above equations that these bosonic fields are hermitian. From eq. (3.12), the commutation relations between the bosonic fields and the electronic density can be computed in k-space, and then written in real space:

$$\left[\phi_\mu(x),\rho_\mu(x')\right] = (-1)^\mu\frac{i}{\sqrt{4\pi}}\delta(x-x') \tag{3.14}$$

Up to a factor $\sqrt{4\pi}$, ϕ and ρ are canonically conjugated fields. The commutation relations between ϕ and itself can be obtained, still from eq. (3.12):

$$\left[\phi_1(x),\phi_1(x')\right] = \frac{1}{2L}\sum_{k<0}\frac{e^{-ak}}{k}\left[e^{-ik(x-x')}+e^{ik(x-x')}\right] \tag{3.15}$$

This sum is well approximated by an integral, and the limit $a\to 0$ is taken. In the same way, the commutator of ϕ_2 with itself can be obtained:

$$\left[\phi_\mu(x),\phi_\mu(x')\right] = (-1)^{\mu+1}\frac{i}{4}\mathrm{sgn}(x-x') \tag{3.16}$$

But when two operators are canonically conjugated, one has the relation

$$\left[p(\lambda),q(\lambda')\right]=-i\delta(\lambda-\lambda')\Rightarrow\left[p(\lambda),e^{iq(\lambda')}\right]=\delta(\lambda-\lambda')e^{iq(\lambda)} \tag{3.17}$$

Looking carefully at the commutators (3.9) and (3.14), one can identify the operators:

$$\begin{aligned}\psi_1(x) &= \frac{U_1}{\sqrt{2\pi a}}e^{ik_Fx}e^{i\sqrt{4\pi}\phi_1(x)}\\ \psi_2(x) &= \frac{U_2}{\sqrt{2\pi a}}e^{-ik_Fx}e^{-i\sqrt{4\pi}\phi_2(x)}\end{aligned} \tag{3.18}$$

with $U_{1,2}$ being Klein factors which ensure the proper anti-commutation relations given by eq. (3.5). Thus, the fermionic operators have been written in terms of the bosonic fields (3.13). The exponential factors $e^{\pm ik_Fx}$ are obtained when computing the average $\langle\psi_r^\dagger(x)\psi_r(x')\rangle_0$ in a non-interacting system. This very powerful system of equation (3.18) is called the bosonization identity.

3.3.2 *Kinetic Hamiltonian*

The bosonization identity provides a new representation in terms of the Luttinger bosonic fields. It allows to re-write the kinetic Hamiltonian given by eq. (3.6) in this new representation. But first, we compute the commutators of H_{kin} with the density operators on each branch:

$$\left[H_{\text{kin}}, \rho_\mu(p)\right] = (-1)^{\mu+1}\hbar v_F p \rho_\mu(p) \tag{3.19}$$

with $\mu = 1, 2$. These equations mean that the states created by the operators $\rho_{1,2}(p)$ are eigenstates of $H_{\text{kin}}$with the energy $\pm\hbar v_F p$. Finally, the kinetic Hamiltonian can be written [65, 86]:

$$H_{\text{kin}} = \frac{\hbar\pi v_F}{2}\sum_{p>0}\left[\rho_1(p)\rho_1(-p) + \rho_2(p)\rho_2(-p)\right] \tag{3.20}$$

$$= \frac{\hbar\pi v_F}{4}\int_0^L dx\left[\rho_1(x)^2 + \rho_2(x)^2\right] \tag{3.21}$$

The equality between the Hamiltonians given by eq. (3.6) and eq. (3.20) is called the Kronig identity [21].

By differentiating eq. (3.13) with respect to x, one gets the charge density on each branch in terms of the bosonic fields.

$$\rho_\mu(x) = \frac{1}{\sqrt{\pi}}\partial_x\phi_\mu(x) \tag{3.22}$$

These equations are of prime importance as they enable to write the Hamiltonian in terms of the bosonic fields. One can now substitute the charge densities in eq. (3.21) by the expressions appearing in eq. (3.22), yielding:

$$H_{\text{kin}} = \hbar v_F\int_0^L dx\left[(\partial_x\phi_1)^2 + (\partial_x\phi_2)^2\right] \tag{3.23}$$

Thus, the kinetic part of the Hamiltonian is both quadratic and diagonal in terms of the bosonic fields. The problem becomes more interesting when interactions are taken into account.

3.3.3 *Interaction Hamiltonian*

The purpose of the TLL theory is to deal with electron-electron interactions. To be added in the bosonized Hamiltonian of eq. (3.23), they first have to be bosonized as well. We only focus here on the interactions we will be later interested in (see sec 4.2), that is to say a local capacitive coupling between two different Luttinger liquids, labeled 1 and 2. (Here, these Luttinger liquids

are counter-propagating, whereas later they will be taken co-propagating.) It reads:

$$\begin{aligned} H_{\text{int}} &= 2\hbar\pi u \int dx \rho_1 \rho_2 \\ &= 2\frac{\hbar}{\pi} u \int dx \big(\partial_x \phi_1\big)\big(\partial_x \phi_2\big) \end{aligned} \tag{3.24}$$

The total Hamiltonian is then given by:

$$H = \frac{\hbar}{\pi} \int_0^L dx v_F \Big[(\partial_x \phi_1)^2 + (\partial_x \phi_2)^2\Big] + 2u\big(\partial_x \phi_1\big)\big(\partial_x \phi_2\big) \tag{3.25}$$

Just as the kinetic Hamiltonian in eq. (3.23), the total Hamiltonian is quadratic in terms of the bosonic fields. This property is absolutely essential, insofar as it guarantees that it is diagonalizable. The eigenstates are also those of the harmonic oscillator.

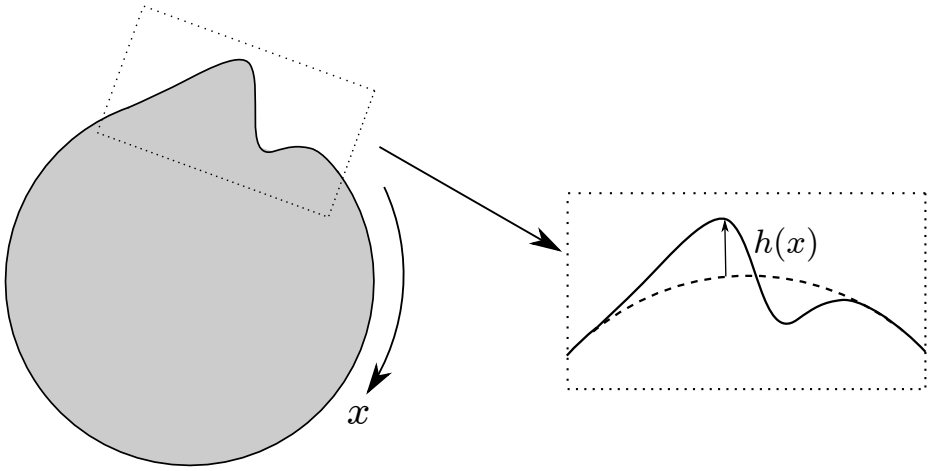

Figure 3.3: A quantum Hall fluid droplet. It undergoes deformations which propagate towards one direction.

3.4 HYDRODYNAMICAL WEN MODEL

We now introduce an empirical model, developed by X.G. Wen in 1992 [92], describing an edge state in the quantum Hall regime. We will see that it can be mapped onto a TLL, with the peculiarity that its spectrum is only composed of one branch, instead of two.

3.4.1 *Hydrodynamical approach*

Let us consider a quantum Hall liquid droplet. It is an incompressible fluid which has a fixed electronic density n_s. In such a system, excitations are deformation waves which propagate along the edge in one direction (see fig. 3.3). Thus the propagation is both one-dimensional and chiral. Let us note $h(x)$ the height of the deformation. The linear density along the edge is then defined by: $\rho(x) = n_s h(x)$. Propagation is finally ruled by the continuity equation:

$$\partial_t \rho - v \partial_x \rho = 0 \tag{3.26}$$

with v the propagation velocity on the edge. The only contribution in the Hamiltonian is then the electrostatic term, that is to say the potential times the total charge:

$$H = \frac{1}{2} \int_0^L dx V(x) e \rho(x) \tag{3.27}$$

When subject to the Hall effect, the electric field of a system is linked to the magentic field as:

$$E = \frac{1}{n_s e} BJ \tag{3.28}$$

with J the current density. On the edge, one has $J = en_s v$, and the previous relation becomes $E = vB$. Finally, the energy can be written as:

$$H = \frac{ev}{2} B \int_0^L dx h(x)\rho(x) = \frac{1}{2}\frac{evB}{n_s}\int_0^L dx \rho(x)^2 \tag{3.29}$$

This Hamiltonian is quadratic in terms of the electronic density. It is useful to define the flux quantum, carried by each electron by surface unit: $\phi_0 = h/e$. The flux quanta density is then naturally $n_\phi = B/\phi_0$. The filling factor ν is defined as the ration between the electronic density and the flux quanta density, and consequently the Hamiltonian can be written using the filling factor rather than the electronic density, as:

$$H = \frac{1}{2}\frac{hv}{\nu}\int_0^L dx \rho(x)^2 \tag{3.30}$$

The Fourier transform density can be made explicit, allowing to write the Hamiltonian in k-space:

$$H = \frac{1}{2}\frac{hv}{\nu}\sum_k \rho(k)\rho(-k) \tag{3.31}$$

and the continuity relation eq. (3.26) reads:

$$\dot{\rho}(k) = -ivk\rho(k)\,. \tag{3.32}$$

Let us quickly consider a Lagrangian formalism governed by the Hamilton equations: $\dot{q} = \partial H/\partial p$ and $\dot{p} = -\partial H/\partial q$. We identify $\rho(k)$ with the generalized coordinate q, and we find, from eq. (3.32) and the Hamilton equations, the canonically conjugate momentum:

$$p(k) = -i\frac{h}{\nu k}\rho(-k) \tag{3.33}$$

3.4.2 *Quantification*

We know the generalized coordinates and the canonically conjugate momentum: so the classical theory can be quantized. $\rho(k)$ and $p(k)$ are now canonically conjugate operators, which obey to the commutation relation:

$$[p(k),\rho(k')] = i\hbar\delta_{kk'} \tag{3.34}$$

Replacing $p(k)$ by its expression in eq. (3.33), one gets the Kac-Moody density-density commutation relation:

$$[\rho(k),\rho(k')] = -\frac{\nu k}{2\pi}\delta_{k,-k'} \tag{3.35}$$

The commutator between the Hamiltonian and the density is thus given by:

$$[H,\rho(k)] = \hbar v k \rho(k) \tag{3.36}$$

This relation is similar to eq. (3.19). It is thus licit to apply the bosonization technique, described in sec. 3.3. We first define the bosonic field:

$$\phi(x) = \frac{\pi}{\sqrt{\nu L}} \sum_k i \frac{e^{-a|k|/2}}{k} e^{-ikx} \rho(k) \tag{3.37}$$

With this definition, the Hamiltonian in eq. (3.30) can be written:

$$H = \frac{\hbar v}{\pi} \int_0^L dx \left(\partial_x \phi\right)^2 \tag{3.38}$$

This Hamiltonian is quadratic and diagonal, as the one of a non-interacting TLL (see sec. 3.3.2). But contrary to the usual case, one field has been introduced instead of two, and the spectrum thus has only one branch. In such a case, the TLL is called chiral. Physically, it means that the excitations are propagating toward one direction only.

Interactions can now be added, and one is able to solve the model, using the bosonization technique introduced previously.

4

THEORETICAL MODEL FOR FILLING FACTOR $\nu = 2$

Using the previous chapter, we are now able to deal with interactions in the IQHE. Consequently, we can mimic much more accurately the experimental conditions: the HOM interferometry is performed at filling factor higher than one, that is to say several co-propagating channels are present on each edge, as explained in section 1.1. Since these channels are very close, Coulomb interaction is far from being negligible. It has indeed been proven experimentally [16] that the charges are fractionnalized as a consequence of inter-edge coupling.

For this reason, we have developed a model which enables one to deal with interferometry at filling factor $\nu = 2$, with local Coulomb repulsion between co-propagating channels. In this model, a lot of information about the electrons propagation in the system is encoded in the Green's functions: whether the temperature is zero or finite, whether the electrons propagate on the outer and inner channels with the same velocity or not... In order to keep it generic as long as possible, the electronic Green's functions are not specified here. Analytical computation of the relevant quantities is performed in the present chapter, until the Green's functions have to be specified. In part iii, explicit results will be provided and commented in several conditions. Nonetheless, we make the assumption that the Green's functions are homogeneous, as it simplifies the calculations a bit, and the results for inhomogeneous Green's functions can be deduced easily from the ones derived here.

4.1 SETUPS

The setup consists in a quantum Hall bar at filling factor $\nu = 2$. On each edge, electrons propagate along two channels, coupled via Coulomb interaction modeled as a short-range interaction H_{int}. Label $j = 1, 2$ identifies outer and inner channels respectively, while $r = R, L$ stands for right and left moving ones. An intrinsic velocity (v_1 or v_2) is assigned to each channel.

Single electrons can be injected along the right-moving and left-moving outer channels of the sample, as it is done experimentally. Indeed, the quantum dots can only be tunnel-coupled to these channels. Like in the non-interacting case, single electron emission is modeled as the creation of exponential wave-packets in real space, as emitted by the mesoscopic capacitor (section 2.1.1).

Backscattering between counter-propagating edge states is enabled by an appropriately tuned QPC, at position $x = 0$ only. Depending on its gate voltage, the outer or inner channels can be selectively transmitted or reflected (see section 1.2). One can thus distinguish two setups (see Fig. 4.1) which we hereby label as setup 1 and 2, corresponding, respectively, to the partitioning of the outer ($s = 1$) or the inner channel ($s = 2$). Both these setups can be realized in practice, and although experimental investigations have focused so far on setup 1, we will be considering them both.

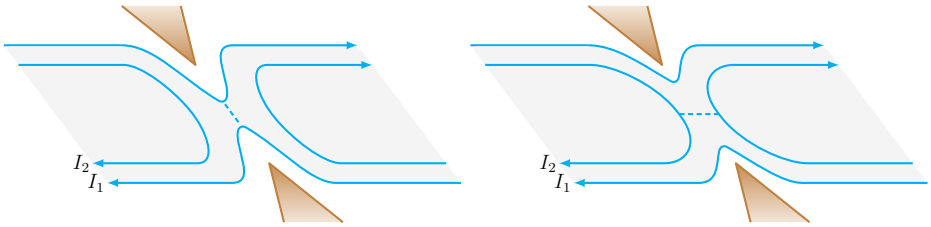

Figure 4.1: The setups: two opposite edge states, each made out of two interacting co-propagating channels, meet at a QPC. (Left) Setup 1: backscattering occurs for outer channels. (Right) Setup 2: backscattering occurs for inner channels.

4.2 BOSONIZATION FRAMEWORK

Our model is based on the TLL theory, which uses the bosonization technique (see chapter 3), in which the fermionic fields are expressed in terms of the bosonic Luttinger ones. In this section, the relevant operators are defined in their bosonized form. Then, a rotation is performed in the bosonic fields basis, so as to make the Hamiltonian diagonal. Finally, the operators are re-expressed in the new basis.

4.2.1 *Definitions*

A chiral Luttinger bosonic field describes each channel : ϕ_{jr} with $j = 1,2$ and $r = R,L$. Each operator in this system can be expressed in terms of those 4 fields. They obey the bosonic commutation relations:

$$[\phi_{jr}(x), \phi_{j'r'}(y)] = -i\pi\delta_{jj'}\delta_{rr'}\mathrm{sgn}(x-y)\,. \tag{4.1}$$

THE ELECTRONIC ANNIHILATION OPERATOR at position x and time t reads:

$$\psi_{jr}(x,t) = \frac{U_r}{\sqrt{2\pi a}} e^{\pm ik_j x} e^{i\phi_{jr}(x,t)} \tag{4.2}$$

where the $+$ sign corresponds to $r = R$ and the $-$ sign to $r = L$, with U_r a Klein factor, and a a cutoff parameter. The Klein factors ensure the proper commutation relations between electronic operators, while the cutoff ensures the convergence of the TLL theory, the cutoff is equal to the smallest length in the system: the magnetic length.

THE HAMILTONIAN is the sum of its kinetic and interaction contributions, which describe respectively the free propagation of electronic excitations, the Coulomb interaction between the co-propagating channels and the intra-channel interaction: $H = H_{\mathrm{kin}} + H_{\mathrm{int}} + H_{\mathrm{intra}}$.

$$H_{\mathrm{kin}} = \frac{\hbar}{\pi} \sum_{j=1,2} v_j \sum_{r=R,L} \int dx \left(\partial_x \phi_{jr}\right)^2 \tag{4.3}$$

$$H_{\mathrm{int}} = 2\frac{\hbar}{\pi} u \sum_r \int dx (\partial_x \phi_{1r})(\partial_x \phi_{2r}) \tag{4.4}$$

$$H_{\mathrm{intra}} = \frac{\hbar}{\pi} \sum_{j,r} U \int dx (\partial_x \phi_{jr})^2 \tag{4.5}$$

where u and U describe respectively the inter- and intra-channel interaction strengths. Let us note here that eq. (4.3) alone describes four quantum Hall edge channels at filling factor $\nu = 1$, and H_{kin} is diagonal in the four Luttinger

fields. The intra-channel interaction, defined by eq. (4.5), simply amounts to a renormalization of the intrinsic velocities $v_{1,2} \to v_{1,2} + U$. For this reason, we will later neglect it as it can be easily switched on by changing the values of v_1 and v_2. What makes the issue we address tricky is that the inter-channel interaction H_{int} prevents the Hamiltonian from being diagonal. Indeed, in the bosonic fields basis, H_{int} corresponds to cross terms.

THE CHARGE DENSITY operator is the electronic charge times the electronic density:

$$q_{jr}(x,t) = e\rho_{jr}(x,t) = \frac{e}{\pi}\partial_x \phi_{jr}(x,t) \tag{4.6}$$

with ρ_{jr} being the electronic density on the corresponding branch. As expressed by eq. (4.4), the inter-channel interaction is a local capacitive coupling between co-propagating channels.

THE CURRENT is given by the variation of the total charge carried on the channel before the position of measurement x_0:

$$I_{jr}(x_0,t) \quad = \quad \frac{dQ_{jr}}{dt}(x_0,t) \tag{4.7}$$

On the right (left) moving channels, the total charge is the sum of the charges at the left (right) of the position of measurement: $y < x_0$ ($y > x_0$).

$$Q_{jR}(x_0,t) \quad = e\int_{-\infty}^{x_0} dy\, \rho_{jR}(y,t) \quad = \frac{e}{\pi}\int_{-\infty}^{x_0} dy\, \partial_y\, \phi_{jR}(y,t) \tag{4.8}$$

$$Q_{jL}(x_0,t) \quad = e\int_{x_0}^{\infty} dy\, \rho_{jL}(y,t) \quad = \frac{e}{\pi}\int_{x_0}^{\infty} dy\, \partial_y\, \phi_{jL}(y,t) \tag{4.9}$$

Using Ehrenfest theorem, the currents can be recast as:

$$I_{jR}(x_0,t) \quad = \quad \frac{e}{i\pi\hbar}\int_{-\infty}^{x_0} dy \Big[\partial_y \phi_{jR}(y,t), H\Big] \tag{4.10}$$

$$I_{jL}(x_0,t) \quad = \quad \frac{e}{i\pi\hbar}\int_{x_0}^{\infty} dy \Big[\partial_y \phi_{jL}(y,t), H\Big] \tag{4.11}$$

These commutators could be computed brute force, but a smarter way to proceed is to rotate the basis of the Luttinger fields before. Then, the calculation of the commutators will become much easier, as the Hamiltonian will be diagonal.

4.2.2 *Diagonalization*

Insofar as the total Hamiltonian is quadratic, one is sure that it can be diagonalized. So we perform a rotation in the Luttinger fields basis, and thus define

four new fields which are linear combinations of the former ones.

Let us define an electronic density vector on each edge: $\boldsymbol{\rho}_\mathbf{r} = \begin{pmatrix} \rho_{1r} \\ \rho_{2r} \end{pmatrix}$. It obeys a matrix continuity equation :

$$\partial_t \boldsymbol{\rho}_\mathbf{r} - \mathcal{V}\partial_x \boldsymbol{\rho}_\mathbf{r} = 0 \qquad \mathcal{V} = \begin{pmatrix} v_1 + U & u \\ u & v_2 + U \end{pmatrix} \tag{4.12}$$

with $\mathcal{V}$ the velocity matrix. The total Hamiltonian can be simply written as :

$$H = \hbar\pi \sum_r {\boldsymbol{\rho}_\mathbf{r}}^\dagger \mathcal{V} \boldsymbol{\rho}_\mathbf{r} \,. \tag{4.13}$$

Eq. (4.13) clearly shows that it is the inter-channel interaction which prevents the Hamiltonian from being diagonal, as its strength u is the non-diagonal term in the velocity matrix, see eq.(4.12).

The full interacting problem can now be easily diagonalized:

$$\mathcal{P}^{-1}\mathcal{V}\mathcal{P} = \begin{pmatrix} v_+ & 0 \\ 0 & v_- \end{pmatrix} \tag{4.14}$$

$v_\pm$ are the eigenvalues of $\mathcal{V}$, also called eigenvelocities. The transformation matrix $\mathcal{P}$ is the counter-clockwise rotation of angle θ defined as:

$$\tan(2\theta) = 2u/(v_1 - v_2) \tag{4.15}$$

It is called the *mixing angle* and expresses the coupling strength between co-propagating channels. There are two limits: $\theta = 0$ and $\theta = \pi/4$. When the mixing angle is zero, the inter-channel interaction strength is zero as well: there is no coupling at all, and the system boils down to four edge states at filling factor one. On the contrary, for $\theta = \pi/4$, the coupling is maximal and the charge fluctuations are equally partitioned between the outer and inner channels.

The eigenvelocities are given by:

$$v_\pm = \frac{v_1 + v_2}{2} + U \pm \frac{u}{\sin 2\theta} \tag{4.16}$$

and the eigenvectors by:

$$\begin{aligned} \rho_+ &= \rho_1 \sin\theta + \rho_2 \cos\theta \\ \rho_- &= \rho_1 \cos\theta - \rho_2 \sin\theta \,. \end{aligned} \tag{4.17}$$

The charge density is related to the bosonic field as $\pi\rho_s = \partial_x \phi_s$. So integrating the previous equations over x, we define four new fields $\phi_\pm = \pi \int dx \rho_\pm$, which provide a new basis to write down the calculation in a simpler way. This two equation system can be inverted, leading to:

$$\begin{aligned} \phi_1 &= \sin\theta\phi_+ + \cos\theta\phi_- \\ \phi_2 &= \cos\theta\phi_+ - \sin\theta\phi_- \end{aligned} \tag{4.18}$$

The rotated Luttinger fields obey the same commutation relations as previously, as given in eq. (4.1):

$$[\phi_{pr}(x), \phi_{p'r'}(y)] = -i\pi\delta_{pp'}\delta_{rr'}\mathrm{sgn}(x-y) \tag{4.19}$$

with $p, p' = \pm$.

4.2.3 *In the rotated basis*

As calculations will be continued in the rotated basis, one needs to express the operators in terms of these rotated fields.

THE ELECTRONIC ANNIHILATION OPERATORS are obtained from eq. (4.2) by replacing ϕ_s by their expressions in terms of $\phi_\pm$, as given by eq. (4.18) and (4.18).

$$\begin{aligned} \psi_{1r}(x,t) &= \frac{U_r}{\sqrt{2\pi a}} e^{\pm ik_1 x} e^{i(\sin\theta\phi_{+r}(x,t) + \cos\theta\phi_{-r}(x,t))} \\ \psi_{2r}(x,t) &= \frac{U_r}{\sqrt{2\pi a}} e^{\pm ik_2 x} e^{i(\cos\theta\phi_{+r}(x,t) - \sin\theta\phi_{-r}(x,t))} \end{aligned} \tag{4.20}$$

The $\pm$ signs correspond respectively to $r = R, L$.

THE HAMILTONIAN is quadratic and diagonal in the new variables :

$$H = \frac{\hbar}{\pi} \sum_r \int dx\, v_+ (\partial_x \phi_{+r})^2 + v_- (\partial_x \phi_{-r})^2 \tag{4.21}$$

This last equation looks very much like eq. (4.3), which describes the free propagation of electrons. Indeed, this Hamiltonian describes the *free propagation of the two collective modes*: a fast charge mode traveling with velocity v_+ and a slow neutral mode propagating at v_-. Instead of addressing the problem in terms of interacting electrons, we are now dealing with non-interacting collective modes.

THE CHARGE DENSITY operators are naturally obtained from eq. (4.6):

$$\begin{aligned} q_1(x,t) &= \frac{e}{\pi} (\sin\theta \partial_x \phi_+(x,t) + \cos\theta \partial_x \phi_-(x,t)) \\ q_2(x,t) &= \frac{e}{\pi} (\cos\theta \partial_x \phi_+(x,t) - \sin\theta \partial_x \phi_-(x,t)) \end{aligned} \tag{4.22}$$

Since $0 \leq \theta \leq \pi/4$, the fast and slow excitations contribute with the same sign to the charge on channel one. On the contrary, on channel two, the fast excitation is plus-charged and the slow one is minus-charged.

THE CURRENT computation can now be carried on. In eq. (4.10) and (4.11), we were left with four commutators to compute: $[\partial_y \phi_{jr}(y,t), H]$. In the rotated basis, it boils down to computing commutators of the type:

$\left[\partial_y \phi_{pr}(y), \left(\partial_x \phi_{p'r'}(x)\right)^2\right]$. These commutators are integrated over x on all the real axis, and over y from $-\infty$ to x_0 on the right moving edge, and from x_0 to $+\infty$ on the left moving edge. Finally, we get expressions for the current operators:

$$\begin{aligned} I_{1r}(x_0,t) &= \pm\frac{2e}{\pi}\left(\sin\theta v_+ \partial_x \phi_{+r}(x_0,t) + \cos\theta v_- \partial_x \phi_{-r}(x_0,t)\right) \\ I_{2r}(x_0,t) &= \pm\frac{2e}{\pi}\left(\cos\theta v_+ \partial_x \phi_{+r}(x_0,t) - \sin\theta v_- \partial_x \phi_{-r}(x_0,t)\right) \end{aligned} \quad (4.23)$$

with the $+$ and $-$ signs corresponding respectively to $r = R$ and L. If we turn back to the channels basis, we get:

$$\begin{aligned} I_{1r}(x_0,t) &= \pm\frac{2e}{\pi}\Big[(\cos^2\theta v_+ + \sin^2\theta v_-)\partial_x \phi_{1r}(x_0,t) \\ &\qquad + \cos\theta\sin\theta(v_+ - v_-)\partial_x \phi_{2r}(x_0,t)\Big] \\ I_{2r}(x_0,t) &= \pm\frac{2e}{\pi}\Big[\cos\theta\sin\theta(v_+ - v_-)\partial_x \phi_{1r}(x_0,t) \\ &\qquad + (\sin^2\theta v_+ + \cos^2\theta v_-)\partial_x \phi_{2r}(x_0,t)\Big] \end{aligned} \quad (4.24)$$

Because of inter-channel interactions, the current on each channel is now caused by the charge fluctuations on *both channels*. They have been mixed by the rotation of angle θ. The non-interacting case can be recovered from the previous equations: if one sets $\theta = 0$, we find back $I_{jr} = (v_F + U)e/\pi\partial_x \phi_{jr}$.

4.3 ON A SINGLE EDGE

Let us focus first on a single edge, the left moving one for example. The two co-propagating channels are coupled via Coulomb interaction and consequently, a charge density fluctuation on the outer channel (typically, a single electron injection) will cause a charge density fluctuation on the inner channel, even if no global charge can be transfered. The purpose of this section is to characterize electron injection on the outer channel.

4.3.1 *Bosonic Green's functions*

In order to obtain information on the dynamics of electrons, one needs to specify the bosonic Green's function. They are defined for each mode by:

$$G_{pr}(x,t;x',t') = \langle \phi_{pr}(x,t)\phi_{pr}(x',t')\rangle - \frac{1}{2}\langle \phi_{pr}^2(x,t)\rangle - \frac{1}{2}\langle \phi_{pr}^2(x',t')\rangle \tag{4.25}$$

with $p = \pm$ and $r = R, L$.

The system is time translation invariant, and we add the assumption that it is also space translation invariant. One consequently has for the correlation function of the bosonic field: $G_{jr}(x,t;x',t') = G_{jr}(t-t';x-x')$.

4.3.2 *Normalization*

The single electron source is modeled through the injection of single electronic wave-packets along the edges at a distance l from the QPC, which amounts to calculating all average values over the prepared state:

$$|\phi_L\rangle = \int dy_L \varphi_L(y_L)\psi_{1,L}^\dagger(y_L + l, 0)|0\rangle\,. \tag{4.26}$$

where $|0\rangle$ describes the FS. This approach is the one we have used at filling factor one, see section 2.1.1.2. In order to be as close as can be to the experiment, electrons are injected on the outer channel as exponential wave-packets in real space, thus mimicking the optimal emission regime of the mesoscopic capacitor:

$$\varphi_L(x) = \sqrt{\frac{2\Gamma}{v_1}} e^{-ik_0 x} e^{-\Gamma x/v_1}\theta(x) \tag{4.27}$$

with θ the Heaviside function. In energy space, this wave packet is Lorentzian: $\varphi_L(\epsilon) = \sqrt{\Gamma/(\pi v_1)}/[(\epsilon-\epsilon_0)/v_F + i\Gamma/v_1]$. Its energy width is Γ, and $\epsilon_0 = k_0 v_F$

is the injection energy. One can also define its energy resolution, as the injection energy over the energy width: $\gamma = \epsilon_0/\Gamma$. In what follows, we will focus on two kinds of wave-packets, we call wide in energy ($\epsilon_0 = 175$mK and $\gamma = 1$) and energy-resolved ($\epsilon_0 = 0.7$K and $\gamma = 8$). The energy-resolved packets are injected much higher above the FS and are thiner in energy, as depicted in fig. 4.2.

The prepared state $|\phi_L\rangle$ has not been normalized yet:

$$\begin{aligned}\mathcal{N}_L &= \langle\phi_L|\phi_L\rangle \\ &= \int dy_L dz_L \varphi_L(y_L)\varphi_L^*(z_L)\langle\psi_{1L}(z_L+l,0)\psi_{1L}^\dagger(y_L+l,0)\rangle_0 \\ &= \frac{1}{2\pi a}\int dy_L dz_L \varphi_L(y_L)\varphi_L^*(z_L)\left\langle e^{i\sin\theta\phi_{+L}(z_L+l,0)}e^{-i\sin\theta\phi_{+L}(y_L+l,0)}\right\rangle_0 \\ &\quad \left\langle e^{i\cos\theta\phi_{-L}(z_L+l,0)}e^{-i\cos\theta\phi_{-L}(y_L+l,0)}\right\rangle_0 \end{aligned} \tag{4.28}$$

where $\langle ...\rangle_0 = \langle 0|...|0\rangle$ denotes averaging over the FS. The operators average is split into two factors, as the fast and slow modes propagation is free.

Important remark:
From now on, all parameters are normalized so that they are dimensionless. That is to say all lengths are divided by the cutoff a, all time scales are multiplied by a/v_F...

$$\begin{aligned} x/a &\to x \\ ka &\to k \\ \Gamma a/v_1 &\to \Gamma \\ t v_F/a &\to t \\ u/v_F &\to u \end{aligned}$$

The correlators are expressed in terms of the bosonic Green's functions:

$$\begin{aligned}\mathcal{N}_L &= \frac{\Gamma}{\pi}\int dy_L dz_L e^{ik_0(z_L-y_L)}e^{-\Gamma(z_L+y_L)}\theta(y_L)\theta(z_L) \\ &\quad \exp\left(\sin^2\theta G_{+L}(0;z_L-y_L)\right)\exp\left(\cos^2\theta G_{-L}(0;z_L-y_L)\right)\end{aligned} \tag{4.29}$$

4.3.3 *Charge density*

As the co-propagating channels are coupled via Coulomb interaction, we are interested in the charge density on both channels after injection and propagation. In order not to repeat the calculation twice, we write the electronic

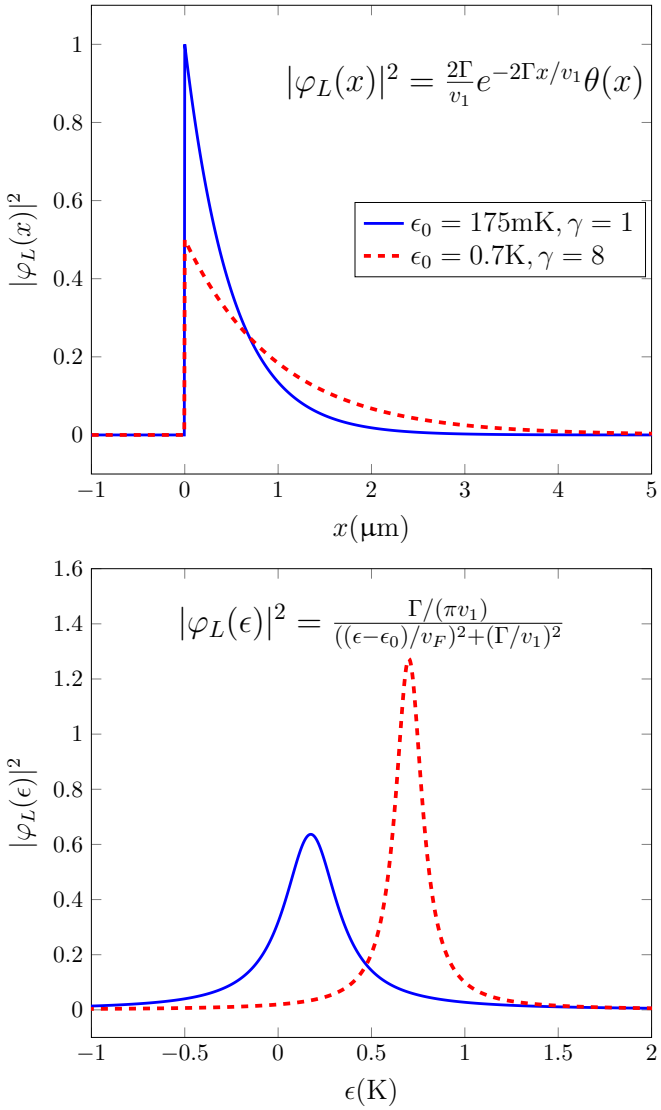

Figure 4.2: Wave-packets envelopes in real space (top) and energy space (bottom). The plain curves are for the packet wide in energy, and the dashed ones for the energy-resolved packet. The energy-resolved packet is injected higher above the FS and is wider in real space.

annihilation operator on both channels in one equation. Indeed, eq. (4.20) can be recast as:

$$\psi_{jr}(x,t) = \frac{U_r}{\sqrt{2\pi a}} e^{\pm i k_j x} \exp\left[i \left(\frac{d}{d\theta} \right)^{j-1} (\sin\theta \phi_{+r}(x,t) + \cos\theta \phi_{-r}(x,t)) \right] \tag{4.30}$$

In terms of the dimensionless parameters and according to eq. (4.22), the charge density operators on the outer and inner channels can be written:

$$q_j(x,t) = \frac{e}{i\pi a} \partial_x \partial_\xi \left(\frac{d}{d\theta} \right)^{j-1} \left\{ \sin\theta e^{i\xi\phi_+(x,t)} + \cos\theta e^{i\xi\phi_-(x,t)} \right\}_{\xi=0} \tag{4.31}$$

Then, on the left moving edge, we compute the charge density mean value in the normalized prepared state $|\phi_L\rangle/\sqrt{\mathcal{N}_L}$. Such an average is noted $\langle ... \rangle_{\phi_L} = \langle \phi_L | ... | \phi_L \rangle / \mathcal{N}_L$.

$$\begin{aligned} \langle q_{jL}(x,t) \rangle_{\phi_L} = & \frac{1}{\mathcal{N}_L} \frac{e\Gamma}{i\pi^2 a} \int dy_L dz_L e^{ik_0(z_L - y_L)} e^{-\Gamma(z_L + y_L)} \theta(y_L)\theta(z_L) \\ & \exp\left(\sin^2\theta G_{+L}(0; z_L - y_L) \right) \exp\left(\cos^2\theta G_{-L}(0; z_L - y_L) \right) \\ \partial_x & \left\{ \sin\theta \left(\frac{d}{d\theta} \right)^{j-1} \left[\sin\theta \left(-G_{+L}(-t; z_L + l - x) + G_{+L}(t; x - y_L - l) \right) \right] \right. \\ & \left. + \cos\theta \left(\frac{d}{d\theta} \right)^{j-1} \left[\cos\theta \left(-G_{-L}(-t; z_L + l - x) + G_{-L}(t; x - y_L - l) \right) \right] \right\} \end{aligned} \tag{4.32}$$

One can see again from this equation that the fast and slow excitations on the inner channel contribute with opposite signs, whereas they contribute with the same signs on the outer channel.

4.3.4 *Noise*

As explained in section 1.3, the noise encodes information about the statistics of the carriers. For this reason, it is of major interest when studying HOM interferometry, which probes exchange statistics between the interfering excitations. At filling factor one (see chapter 2), we could extract a lot of information from this quantity: the width of the exponential wave-packets colliding, their degree of indistiguishability, etc. The zero-frequency noise is defined as the Fourier transform of the current-current auto-correlations.

$$S_{ij}^{LL} = \int dt dt' \langle I_{iL}(x,t) I_{jL}(x',t') \rangle - \langle I_{iL}(x,t) \rangle \langle I_{jL}(x',t') \rangle \qquad i,j = 1,2 \tag{4.33}$$

where the averages are taken in the normalized prepared state $|\phi_L\rangle/\sqrt{\mathcal{N}_L}$ and the FS contribution is ruled out.

The two parts of the eq. (4.33) must be computed separately: on the one hand the true correlations and on the other the current averages. First, the true correlations are defined as:

$$C_{ij}^{LL} = \int dtdt' \langle I_{iL}(x,t) I_{jL}(x',t') \rangle_{\phi_L} - \langle I_{iL}(x,t) I_{jL}(x',t') \rangle_0 \tag{4.34}$$

In terms of the dimensionless parameters, the current on channel 1, for example, is :

$$I_{1L}(x,t) = \frac{2ie}{\pi a} \partial_x \partial_\xi \Big|_{\xi=0} e^{i\xi(\sin\theta v_+ \phi_{+L}(x,t) + \cos\theta v_- \phi_{-L}(x,t))} \tag{4.35}$$

Let us compute the current product in the prepared state for $i = j = 1$:

$$\begin{aligned}
& \int dtdt' \langle I_{1L}(x,t) I_{1L}(x',t') \rangle_{\phi_L} \\
= \; & -\left(\frac{2e}{\pi}\right)^2 \frac{\Gamma}{\pi \mathcal{N}_L} \int dy_L dz_L e^{ik_0(z_L - y_L)} e^{-\Gamma(z_L + y_L)} \theta(y_L)\theta(z_L) \\
& \int dtdt' \partial_x \partial_{x'} \partial_\xi \partial_{\xi'} \Big|_{\xi=\xi'=0} \\
& \left\langle e^{i\sin\theta \phi_{+L}(z_L + l, 0)} e^{i\xi \sin\theta v_+ \phi_{+L}(x,t)} e^{i\xi' \sin\theta v_+ \phi_{+L}(x',t')} e^{-i\sin\theta \phi_{+L}(y_L + l, 0)} \right\rangle_0 \\
& \left\langle e^{i\cos\theta \phi_{-L}(z_L + l, 0)} e^{i\xi \cos\theta v_- \phi_{-L}(x,t)} e^{i\xi' \cos\theta v_- \phi_{-L}(x',t')} e^{-i\cos\theta \phi_{-L}(y_L + l, 0)} \right\rangle_0
\end{aligned} \tag{4.36}$$

Using Wick's theorem, the averages are recast as a product of Green's functions, in which the FS contribution appears explicitly. This latter is canceled in the true correlations. C_{12}^{LL} and C_{22}^{LL} can be obtained by the same kind of calculation, only some signs and the angular factors are changed. These three quantities can be recast together if we define:

$$\begin{aligned}
\mathcal{I}_j(y_L, z_L) \; = \; & \int dt \partial_x \Big\{ v_+ \sin\theta \left(\frac{d}{d\theta}\right)^{j-1} \sin\theta \\
& \quad [-G_{+L}(-t; z_L + l - x) + G_{+L}(t; x - y_L - l)] \\
& + v_- \cos\theta \left(\frac{d}{d\theta}\right)^{j-1} \cos\theta \\
& \quad [-G_{-L}(-t; z_L + l - x) + G_{-L}(t; x - y_L - l)] \Big\}
\end{aligned} \tag{4.37}$$

One important remark here is that these quantities do not depend on the measurement position x. Because of the linear dispersion of the edges, we have: $G_{\pm L}(t; x) = \mathcal{G}(t + x/v_\pm)$. Thus, when performing the integral over time, the x-dependency is lost. Consequently, neither the true correlations nor the noise will depend on the measurement positions. For the sake of simplicity, we choose them to be zero: $x = x' = 0$. Thus, the electron injection position l (see eq. (4.26)) also defines the propagation length before the QPC.

The true correlations can then be written:

$$C_{ij}^{LL} = -\left(\frac{2e}{\pi}\right)^2 \frac{\Gamma}{\pi\mathcal{N}_L} \int dy_L dz_L e^{ik_0(z_L-y_L)} e^{-\Gamma(z_L+y_L)} \theta(y_L)\theta(z_L) \exp\left[\sin^2\theta G_{+L}(0;z_L-y_L) + \cos^2\theta G_{-L}(0;z_L-y_L)\right] \mathcal{I}_i(y_L,z_L)\mathcal{I}_j(y_L,z_L) \tag{4.38}$$

The time integral of the current average can be obtained in the same way: we just have to get rid of one current operator. In that case, the FS contribution is zero and we are left with:

$$\int dt \langle I_{iL}(t)\rangle_{\phi_L} = \frac{2ei}{\pi} \frac{\Gamma}{\pi\mathcal{N}_L} \int dy_L dz_L e^{ik_0(z_L-y_L)} e^{-\Gamma(z_L+y_L)} \theta(y_L)\theta(z_L) \exp\left[\sin^2\theta G_{+L}(0;z_L-y_L) + \cos^2\theta G_{-L}(o;z_L-y_L)\right] \mathcal{I}_i(y_L,z_L) \tag{4.39}$$

The noise after the injection finally reads:

$$S_{ij}^{LL} = C_{ij}^{LL} - \int dt \langle I_{iL}(t)\rangle_{\phi_L} \int dt' \langle I_{jL}(t')\rangle_{\phi_L} \tag{4.40}$$

Remark:
In the case in which both $\mathcal{I}_j$ do not depend on (y_L, z_L), the correlations are given by $C_{ij}^{LL} = -(2e/\pi)^2 \mathcal{I}_i\mathcal{I}_j$, and the time integrals of the currents by $\int dt \langle I_{jL}(t)\rangle_{\phi_L} = (2ei/\pi)\mathcal{I}_j$. Consequently, in this case, one directly has: $S_{ij}^{LL} = 0$.

4.4 HANBURY BROWN AND TWISS EXPERIMENT

We partition at the QPC the excitations propagating along the left-moving edge, following the injection along the outer left-moving channel of an exponential wave-packet at position $x = l$. Depending on the setup (see Fig. 4.1), either the injection channel or the co-propagating one is partitioned. The other channel is either fully transmitted or fully reflected.

The quantity of interest is the zero-frequency current correlations [66, 67] (or noise) measured on the partitioned channel: $S_{\text{HBT}} = \int dtdt' \langle I_s(t) I_s(t') \rangle - \langle I_s(t) \rangle \langle I_s(t') \rangle$, with $s = 1, 2$ the setup label. We choose to focus on the auto-correlation noise rather than the cross-correlation noise, as in chapter 2. In the end, it simply amounts to changing the sign in front of the mixed term, already defined in eq. (2.9). As in eq. (4.33), the averages are performed in the normalized prepared state $|\phi_L\rangle / \sqrt{\mathcal{N}_L}$ and the FS contribution has been removed. Once again, the linear dispersion of the edges rules out the measurement positions dependencies and allows us to compute the noise at the immediate output of the QPC, without loss of generality.

4.4.1 *Scattering matrix*

The QPC is described by its scattering matrix, like in the previous part (see eq. (2.6)), despite the slightly different notations. The outgoing fields along the partitioned channel are related to the incoming ones:

$$\begin{pmatrix} \psi_{sR} \\ \psi_{sL} \end{pmatrix}^{\text{outgoing}} = \begin{pmatrix} \sqrt{\mathcal{T}} & i\sqrt{\mathcal{R}} \\ i\sqrt{\mathcal{R}} & \sqrt{\mathcal{T}} \end{pmatrix} \begin{pmatrix} \psi_{sR} \\ \psi_{sL} \end{pmatrix}^{\text{incoming}} \tag{4.41}$$

where $\mathcal{T}$ and $\mathcal{R} = 1 - \mathcal{T}$ are the transmission and reflexion probabilities. Eq. (4.41) allows us to express the noise in terms of the incoming operators only [36]:

$$S_{\text{HBT}} = \mathcal{R}^2 S_{ss}^{LL} + \mathcal{T}^2 S_{ss}^{RR} + (ev_s)^2 \mathcal{R}\mathcal{T}\mathcal{M} \tag{4.42}$$

All quantities in the right member of eq. (4.42) are computed at the input of the QPC. We already know that $S_{ss}^{RR} = 0$ as no electron is injected on the right moving edge, and the FS contribution is subtracted. The mixed term can be written:

$$\begin{aligned} \mathcal{M} = \int dtdt' \langle \psi_{sR}^\dagger(t) \psi_{sR}(t') \rangle_0 \Big(\langle \psi_{sL}(t) \psi_{sL}^\dagger(t') \rangle_{\phi_L} - \langle \psi_{sL}(t) \psi_{sL}^\dagger(t') \rangle_0 \Big) \\ + \Big(\langle \psi_{sL}^\dagger(t) \psi_{sL}(t') \rangle_{\phi_L} - \langle \psi_{sL}^\dagger(t) \psi_{sL}(t') \rangle_0 \Big) \langle \psi_{sR}(t) \psi_{sR}^\dagger(t') \rangle_0 \end{aligned} \tag{4.43}$$

The averages are expressed in terms of the fast and slow Green's functions of the bosonic fields. As the incoming noise has already been computed, one is left with the calculation of the mixed term.

4.4.2 *Mixed term*

Depending on the setup, we do not need to compute the same averages. Both case are nonetheless treated at the same time, using the trick of eq. (4.30). On the left moving edge, on channel s, we have:

$$\begin{aligned}
&\langle \psi_{sL}^{-\varepsilon}(t)\psi_{sL}^{\varepsilon}(t')\rangle_{\phi_L} \\
=\;& \frac{1}{2\pi a}\frac{\Gamma}{\pi\mathcal{N}_L}\int dy_L dz_L e^{ik_0(z_L-y_L)}e^{-\Gamma(z_L+y_L)}\theta(y_L)\theta(z_L) \\
&\Big\langle e^{i\sin\theta\phi_{+L}(z_L+l,0)+\cos\theta\phi_{-L}(z_L+l,0)}e^{i\varepsilon\left(\frac{d}{d\theta}\right)^{s-1}(\sin\theta\phi_{+L}(0,t)+\cos\theta\phi_{-L}(0,t))} \\
&e^{-i\varepsilon\left(\frac{d}{d\theta}\right)^{s-1}(\sin\theta\phi_{+L}(0,t')+\cos\theta\phi_{-L}(0,t'))}e^{-i(\sin\theta\phi_{+L}(y_L+l,0)+\cos\theta\phi_{-L}(y_L+l,0))}\Big\rangle_0 \\
=\;& \frac{\Gamma}{2\pi^2 a\mathcal{N}_L}\int dy_L dz_L e^{ik_0(z_L-y_L)}e^{-\Gamma(z_L+y_L)}\theta(y_L)\theta(z_L) \\
&\exp\left[\sin^2\theta G_{+L}(0;z_L-y_L)\right]\exp\left[\cos^2\theta G_{-L}(0;z_L-y_L)\right] \\
&\exp\left[\left(\left(\frac{d}{d\theta}\right)^{s-1}\sin\theta\right)^2 G_{+L}(t-t';0)\right]\exp\left[\left(\left(\frac{d}{d\theta}\right)^{s-1}\cos\theta\right)^2 G_{-L}(t-t';0)\right] \\
&\exp\left[\varepsilon\sin\theta\left(\frac{d}{d\theta}\right)^{s-1}\sin\theta\left(\mathcal{A}_{+L}(-t,-t';z_L+l)-\mathcal{A}_{+L}(t,t';-y_L-l)\right)\right] \\
&\exp\left[\varepsilon\cos\theta\left(\frac{d}{d\theta}\right)^{s-1}\cos\theta\left(\mathcal{A}_{-L}(-t,-t';z_L+l)-\mathcal{A}_{-L}(t,t';-y_L-l)\right)\right]
\end{aligned} \tag{4.44}$$

where $\varepsilon = +$ designates the operator dagger and $\varepsilon = -$ leaves the operator unchanged. We have also defined:

$$\mathcal{A}_{\pm r}(t,t';x) = -G_{\pm r}(t;x) + G_{\pm r}(t';x) \tag{4.45}$$

We now turn to the computation of the averages over the FS. Noticing that $G_{\pm R}(t;0) = G_{\pm L}(t;0)$, all are found equal and read:

$$\begin{aligned}
&\langle \psi_{sR}^{\dagger}(t)\psi_{sR}(t')\rangle_0 = \langle \psi_{sR}(t)\psi_{sR}^{\dagger}(t')\rangle_0 = \langle \psi_{sL}(t)\psi_{sL}^{\dagger}(t')\rangle_0 = \langle \psi_{sL}^{\dagger}(t)\psi_{sL}(t')\rangle_0 \\
=\;& \frac{1}{2\pi a}\exp\left[\left(\left(\frac{d}{d\theta}\right)^{s-1}\sin\theta\right)^2 G_{+L}(t-t';0)\right]\exp\left[\left(\left(\frac{d}{d\theta}\right)^{s-1}\cos\theta\right)^2 G_{-L}(t-t';0)\right]
\end{aligned} \tag{4.46}$$

The HBT mixed term is finally given by:

$$\begin{aligned}
\mathcal{M} \;=\; & \frac{2\Gamma}{(2\pi)^3\mathcal{N}_L}\int dy_L dz_L e^{ik_0(z_L-y_L)}e^{-\Gamma(z_L+y_L)}\theta(y_L)\theta(z_L) \\
& \exp\left[\sin^2\theta G_{+L}(0;z_L-y_L)\right]\exp\left[\cos^2\theta G_{-L}(0;z_L-y_L)\right] \\
& \int dtdt'\exp\left[2\left(\left(\frac{d}{d\theta}\right)^{s-1}\sin\theta\right)^2 G_{+L}(t-t';0)\right] \\
& \qquad \exp\left[2\left(\left(\frac{d}{d\theta}\right)^{s-1}\cos\theta\right)^2 G_{-L}(t-t';0)\right] \\
& \left\{\exp\left[\sin\theta\left(\frac{d}{d\theta}\right)^{s-1}\sin\theta\left(\mathcal{A}_{+L}(-t,-t';z_L+L)-\mathcal{A}_{+L}(t,t';-y_L-L)\right)\right]\right. \\
& \quad \exp\left[\cos\theta\left(\frac{d}{d\theta}\right)^{s-1}\cos\theta\left(\mathcal{A}_{-L}(-t,-t';z_L+L)-\mathcal{A}_{-L}(t,t';-y_L-L)\right)\right]-1 \\
& +\exp\left[\sin\theta\left(\frac{d}{d\theta}\right)^{s-1}\sin\theta\left(-\mathcal{A}_{+L}(-t,-t';z_L+L)+\mathcal{A}_{+L}(t,t';-y_L-L)\right)\right] \\
& \left.\quad \exp\left[\cos\theta\left(\frac{d}{d\theta}\right)^{s-1}\cos\theta\left(-\mathcal{A}_{-L}(-t,-t';z_L+L)+\mathcal{A}_{-L}(t,t';-y_L-L)\right)\right]-1\right\}
\end{aligned} \tag{4.47}$$

An interesting property to notice from eq. (4.45) is: $\mathcal{A}_{\pm L}(t,t';x) = -\mathcal{A}_{\pm L}(t',t;x)$. We perform the substitution $t \leftrightarrow t'$ in the last term of the sum, and use that $G_{\pm L}(-t;-x) = G^*_{\pm L}(t;x)$, and the property $\mathcal{A}_{\pm L}(-t,-t';-x) = \mathcal{A}^*_{\pm L}(t,t';x)$ to find:

$$\begin{aligned}
\mathcal{M} \;=\; & \frac{\Gamma}{2\pi^3\mathcal{N}_L}\int dy_L dz_L e^{ik_0(z_L-y_L)}e^{-\Gamma(z_L+y_L)}\theta(y_L)\theta(z_L) \\
& \exp\left[\sin^2\theta G_{+L}(0;z_L-y_L)\right]\exp\left[\cos^2\theta G_{-L}(0;z_L-y_L)\right] \\
& \int dtdt'\mathrm{Re}\left\{\exp\left[2\left(\left(\frac{d}{d\theta}\right)^{s-1}\sin\theta\right)^2 G_{+L}(t-t';0)\right]\right. \\
& \qquad \left.\exp\left[2\left(\left(\frac{d}{d\theta}\right)^{s-1}\cos\theta\right)^2 G_{-L}(t-t';0)\right]\right\} \\
& \left\{\exp\left[\sin\theta\left(\frac{d}{d\theta}\right)^{s-1}\sin\theta\left(\mathcal{A}_{+L}(-t,-t';z_L+L)-\mathcal{A}^*_{+L}(-t,-t';y_L+L)\right)\right]\right. \\
& \left.\quad \exp\left[\cos\theta\left(\frac{d}{d\theta}\right)^{s-1}\cos\theta\left(\mathcal{A}_{-L}(-t,-t';z_L+L)-\mathcal{A}^*_{-L}(-t,-t';y_L+L)\right)\right]-1\right\}
\end{aligned} \tag{4.48}$$

4.5 HONG-OU-MANDEL EXPERIMENT

Another electron is now injected on the right moving arm, at position $x = -l$ with a time delay δT over the left moving one. The prepared state is replaced by $|\phi_R\rangle \otimes |\phi_L\rangle / \sqrt{\mathcal{N}_R \mathcal{N}_L}$, with

$$|\phi_R\rangle = \int dy_R \varphi_R(y_R) \psi_{1R}^\dagger(y_R - l, \delta T)|0\rangle \tag{4.49}$$

and $|\phi_L\rangle$ given by eq. (4.26). For the sake of simplicity, we focus on the interference between identical wave-packets: $\varphi_R(x) = \varphi_L(-x)$. The description of the QPC by its scattering matrix is still valid, but this time the incoming noise on the right-moving channel is non-zero, as an electron has been injected on the right-moving edge as well: $S_{ss}^{RR} \neq 0$. The mixed term is given by:

$$\begin{aligned} \mathcal{M} = \int dt dt' \quad & \langle \psi_{sR}^\dagger(t) \psi_{sR}(t') \rangle_{\phi_R} \langle \psi_{sL}(t) \psi_{sL}^\dagger(t') \rangle_{\phi_L} \\ - \quad & \langle \psi_{sR}^\dagger(t) \psi_{sR}(t') \rangle_0 \langle \psi_{sL}(t) \psi_{sL}^\dagger(t') \rangle_0 \\ + \quad & \langle \psi_{sL}^\dagger(t) \psi_{sL}(t') \rangle_{\phi_L} \langle \psi_{sR}(t) \psi_{sR}^\dagger(t') \rangle_{\phi_R} \\ - \quad & \langle \psi_{sL}^\dagger(t) \psi_{sL}(t') \rangle_0 \langle \psi_{sR}(t) \psi_{sR}^\dagger(t') \rangle_0 \,. \end{aligned} \tag{4.50}$$

Only the averages in the state $|\phi_R\rangle / \sqrt{\mathcal{N}_R}$ have to be computed again.

On the right moving edge, for setup s, we have:

$$
\begin{aligned}
& \langle \psi_{sR}^{\varepsilon}(t)\psi_{sR}^{-\varepsilon}(t')\rangle_{\phi_R} \\
= \;& \frac{1}{2\pi a}\frac{\Gamma}{\pi\mathcal{N}_R}\int dy_R dz_R e^{ik_0(y_R-z_R)}e^{\Gamma(z_R+y_R)}\theta(-y_R)\theta(-z_R) \\
& \Big\langle e^{i(\sin\theta\phi_{+R}(z_R-l,\delta T)+\cos\theta\phi_{-R}(z_R-l,\delta T))}e^{-i\varepsilon\left(\frac{d}{d\theta}\right)^{s-1}(\sin\theta\phi_{+R}(0,t)+\cos\theta\phi_{-R}(0,t))} \\
& \quad e^{i\varepsilon\left(\frac{d}{d\theta}\right)^{s-1}(\sin\theta\phi_{+R}(0,t')+\cos\theta\phi_{-R}(0,t'))}e^{-i(\sin\theta\phi_{+R}(y_R-l,\delta T)+\cos\theta\phi_{-R}(y_R-l,\delta T))}\Big\rangle_0 \\
= \;& \frac{\Gamma}{2\pi^2 a\mathcal{N}_R}\int dy_R dz_R e^{ik_0(y_R-z_R)}e^{\Gamma(z_R+y_R)}\theta(-y_R)\theta(-z_R) \\
& \exp\left[\sin^2\theta G_{+R}(0;z_R-y_R)\right]\exp\left[\cos^2\theta G_{-R}(0;z_R-y_R)\right] \\
& \exp\left[\left(\left(\frac{d}{d\theta}\right)^{s-1}\sin\theta\right)^2 G_{+R}(t-t';0)\right]\exp\left[\left(\left(\frac{d}{d\theta}\right)^{s-1}\cos\theta\right)^2 G_{-R}(t-t';0)\right] \\
& \exp\left[\varepsilon\sin\theta\left(\frac{d}{d\theta}\right)^{s-1}\sin\theta\right. \\
& \qquad \left.\left(\mathcal{A}^*_{+R}(\delta T-t,\delta T-t';y_R-l)-\mathcal{A}_{+R}(\delta T-t,\delta T-t';z_R-l)\right)\right] \\
& \exp\left[\varepsilon\cos\theta\left(\frac{d}{d\theta}\right)^{s-1}\cos\theta\right. \\
& \qquad \left.(\mathcal{A}^*_{-R}(\delta T-t,\delta T-t';y_R-l)-\mathcal{A}_{-R}(\delta T-t,\delta T-t';z_R-l))\right]
\end{aligned}
\tag{4.51}
$$

Performing the same simplifications as previously, the mixed term is finally modified as:

$$
\begin{aligned}
\mathcal{M} \;=\; & \frac{\Gamma^2}{2\pi^4 \mathcal{N}_L \mathcal{N}_R} \int dy_L dz_L dy_R dz_R e^{ik_0(z_L - y_L + y_R - z_R)} e^{\Gamma(y_R + z_R - y_L - z_L)} \\
& \exp\Big[\sin^2\theta G_{+L}(0; z_L - y_L)\Big] \exp\Big[\cos^2\theta G_{-L}(0; z_L - y_L)\Big] \theta(y_L)\theta(z_L) \\
& \exp\Big[\sin^2\theta G_{+R}(0; z_R - y_R)\Big] \exp\Big[\cos^2\theta G_{-R}(0; z_R - y_R)\Big] \theta(-y_R)\theta(-z_R) \\
& \int dt dt' \mathrm{Re}\Bigg\{ \exp\left[2\left(\left(\frac{d}{d\theta} \right)^{s-1} \sin\theta \right)^2 G_{+L}(t - t'; 0) \right] \\
& \qquad \exp\left[2\left(\left(\frac{d}{d\theta} \right)^{s-1} \cos\theta \right)^2 G_{-L}(t - t'; 0) \right] \Bigg\} \\
& \Bigg\{ \exp\left[\sin\theta \left(\frac{d}{d\theta} \right)^{s-1} \sin\theta \Big(\mathcal{A}_{+L}(-t, -t'; z_L + L) - \mathcal{A}^*_{+L}(-t, -t'; y_L + L) \Big) \right] \\
& \quad \exp\left[\cos\theta \left(\frac{d}{d\theta} \right)^{s-1} \cos\theta \left(\mathcal{A}_{-L}(-t, -t'; z_L + L) - \mathcal{A}^*_{-L}(-t, -t'; y_L + L) \right) \right] \\
& \quad \exp\Bigg[\sin\theta \left(\frac{d}{d\theta} \right)^{s-1} \sin\theta \\
& \qquad \Big(\mathcal{A}^*_{+R}(\delta T - t, \delta T - t'; y_R - L) - \mathcal{A}_{+R}(\delta T - t, \delta T - t'; z_R - L) \Big) \Bigg] \\
& \quad \exp\Bigg[\cos\theta \left(\frac{d}{d\theta} \right)^{s-1} \cos\theta \\
& \qquad \left(\mathcal{A}^*_{-R}(\delta T - t, \delta T - t'; y_R - L) - \mathcal{A}_{-R}(\delta T - t, \delta T - t'; z_R - L) \right) \Bigg] - 1 \Bigg\}
\end{aligned}
\tag{4.52}
$$

4.6 CONCLUSION

To sum up, several formula have been derived here, which are very generic, except for the assumption that the bosonic Green's functions are homogeneous. After choosing appropriately such Green's functions, one can substitute them in eq. (4.29) and (4.32) to obtain immediately the prepared state norm and the charge density after injection on both channels, respectively. Similarly, the same substitution in eq. (4.38) and (4.39) allows to obtain the true correlations and the time integral of the current average, from which the noise associated with the injection process -which will enter the QPC- is obtained, using eq. (4.40). Even more importantly, the HBT and HOM mixed terms are obtained using eq. (4.48) and (4.52) respectively. The outgoing noise is then a linear combination of the incoming noises and the mixed term, as specified in eq. (4.42).

Part III

ELECTRON QUANTUM OPTICS AT FILLING FACTOR $\nu = 2$

All computations have been made so far for any mixing angle, but we will now focus on the so called strong coupling regime, defined by $\theta = \pi/4$. This regime, which seems to be the most relevant experimentally [16], mixes the co-propagating channels in a maximal way.

As a result of propagation under the influence of interactions, an electronic excitation will fractionalize and additional electron-hole pairs will be excited at low energy. Depending on the zero or finite character of the temperature, the physics is quite different. Indeed, the finite temperature acts as a small energy cutoff, which limits the creation of electron-hole pairs near the FS.

In such cases, the common choice is to start with the zero temperature model. However, here, the finite temperature results are much more relevant as they better reproduce the experimental conditions: indeed, no experiment can be realized at zero temperature! Consequently, we will start with the finite temperature case, in which the temperature is set at its experimental value: $\Theta \sim 0.1\text{K}$. Then, we will refine the model, so that the inter-channel interactions are switched on, on finite region of the sample only. The electron emission is thus better reproduced. Finally, we will turn to the less experimentally relevant zero temperature case, in which peculiarities are observed.

5

FINITE TEMPERATURE

As discussed in section 4.2.1, the physics is very little modified by adding intra-channel interaction. It amounts to a renormalization of the velocities $v_{1,2} \to v_{1,2} + U$. We thus focus on the regime with no intra-channel interaction: $U = 0$. As are working in the strong coupling regime, the eigenvelocities, defined by eq. (4.16), are given by: $v_\pm = 1 \pm u$, and the intrinsic velocities are the same on the inner and outer channels: $v_1 = v_2 = v_F = 1$.

In order to match with the experimental conditions, we choose the temperature to be $\Theta = 0.1\text{K}$.

Finally, the results are plotted with real units, instead of our system of arbitrary units. The conversion from one system to another is detailed in appendix, section A.1.

5.1 PRELIMINARIES

5.1.1 *Green's functions*

The retarded Green's functions for the bosonic eigenfields read:

$$\begin{aligned} G_{\pm R}(t;x) &= -\log\left[s\left(\frac{i}{v_\pm}-t+\frac{x}{v_\pm}\right)\Big/ s\left(\frac{i}{v_\pm}\right)\right] \\ G_{\pm L}(t;x) &= -\log\left[s\left(\frac{i}{v_\pm}-t-\frac{x}{v_\pm}\right)\Big/ s\left(\frac{i}{v_\pm}\right)\right] \end{aligned} \tag{5.1}$$

with $s(x)=\sinh(\pi x/\beta)$ and $\beta = 1/(k_B\Theta)$ the inverse temperature.

5.1.2 *Normalization*

When replacing the Green's functions by their expression in eq. (4.29), we get:

$$\begin{aligned} \mathcal{N}_L &= \frac{\Gamma}{\pi}\int dy_L dz_L e^{ik_0(z_L-y_L)-\Gamma(z_L+y_L)}\theta(y_L)\theta(z_L) \\ &\quad \left[\frac{s(i/v_+)}{s\left((y_L+i)/v_+\right)}\right]^{1/2}\left[\frac{s(i/v_-)}{s\left((y_L+i)/v_-\right)}\right]^{1/2} \end{aligned} \tag{5.2}$$

Performing the substitution $y_L - z_L \to y_L$ and computing the integral over z_L, one is left with:

$$\mathcal{N} = \frac{1}{2\pi}\int dy_L e^{-ik_0 y_L-\Gamma|y_L|}\left[\frac{s(i/v_+)}{s\left((y_L+i)/v_+\right)}\right]^{1/2}\left[\frac{s(i/v_-)}{s\left((y_L+i)/v_-\right)}\right]^{1/2} \tag{5.3}$$

This latter integral is easily computed numerically. (On the right moving edge, one would have found $\mathcal{N}_R = \mathcal{N}_L = \mathcal{N}$.)

5.1.3 *Charge fractionalization*

Using the finite temperature Green's functions, from eq. (4.32), we compute the charge density on both channels:

$$\begin{aligned}\langle q_{jL}(x,t)\rangle_{\phi_L} = \frac{1}{\mathcal{N}}\frac{e\Gamma}{2i\pi^2 a}\int dy_L dz_L e^{ik_0(z_L-y_L)}e^{-\Gamma(z_L+y_L)}\theta(y_L)\theta(z_L)\\ \left[\frac{s(i/v_+)}{s\left((y_L-z_L+i)/v_+\right)}\right]^{1/2}\left[\frac{s(i/v_-)}{s\left((y_L-z_L+i)/v_-\right)}\right]^{1/2}\\ \left\{\frac{\pi}{\beta v_+}\left[\coth\left(\frac{\pi}{\beta v_+}(i+v_+t+x-z_L-L)\right)\right.\right.\\ \left.+\coth\left(\frac{\pi}{\beta v_+}(i-(v_+t+x-y_L-L))\right)\right]\\ +\frac{\sigma_j\pi}{\beta v_-}\left[\coth\left(\frac{\pi}{\beta v_-}(i+v_-t+x-z_L-L)\right)\right.\\ \left.\left.+\coth\left(\frac{\pi}{\beta v_-}(i-(v_-t+x-y_L-L))\right)\right]\right\}\end{aligned} \tag{5.4}$$

with $\sigma_j = (-1)^{j+1}$. One can already see here that both the fast and slow excitations carry the same charge, on the outer channel. Only the sign of the charge of the slow excitation is switched, on the inner channel.

When imaging the charge density at the time of injection (see fig. 5.1), one can see the electronic wave-packet injected on the outer channel. Its shape differs from the exponential wave-packet envelope (see fig. 4.2, top panel), since our calculations are only exact in the limit of a zero cutoff: $a \to 0$, which cannot be achieved numerically. The non-zero cutoff effects are all the more important since the packet is injected at high energy (bottom panel). On the inner channel, almost nothing can be seen yet. The slight charge imaged on the inner channel, at finite temperature, is also due to the finite cutoff errors.

During propagation, the charge fractionalizes into two modes (see fig. 5.2): a fast charged mode traveling at velocity v_+, and a slow neutral mode traveling at velocity v_-. Each mode is made of two excitations: one on each channel. Both excitations composing the fast mode are $\oplus$, that is to say carrying the charge $e/2$. Thus, its total charge is e. The slow mode is composed of one $\oplus$-excitation on the outer channel and one $\ominus$-excitation -carrying the charge $-e/2$- on the inner channel. It is thus neutral. Furthermore, the total charge on the outer channel is e, whereas it remains zero on the inner channel. No charge is transfered between co-propagating channels, only the capacitive coupling induces charge fluctuations on the inner channel.

As the electronic wave-packet propagates, that is to say the propagation time t increases, the spatial splitting between the fast and slow modes increases (see fig. 5.2).

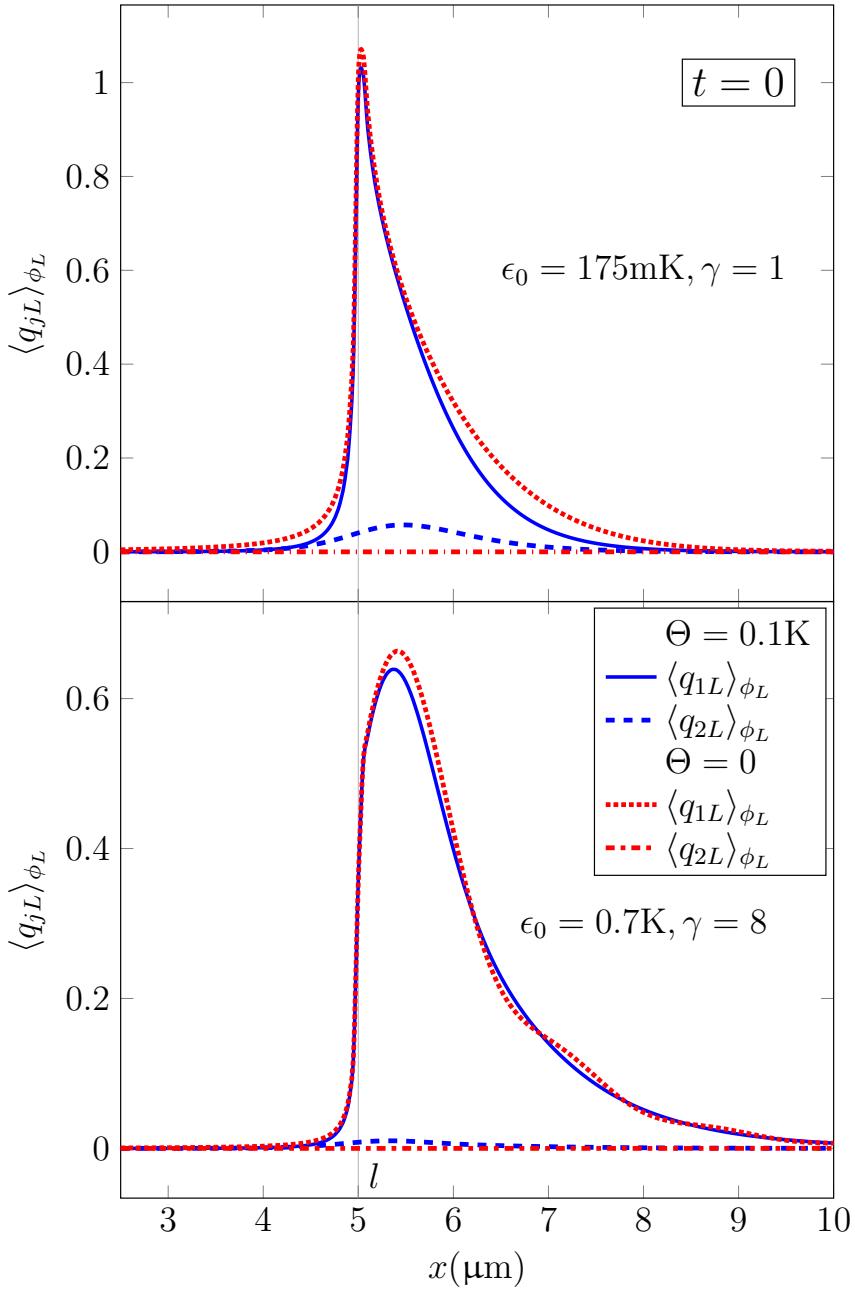

Figure 5.1: Charge density on the outer channel (plain blue at finite temperature, dotted red at zero temperature) and inner channel (dashed blue at finite temperature, dash-dotted red at zero temperature), at the injection time $t = 0$, for wide packets in energy (top panel) and energy resolved packets (bottom panel). The injection position is $l = 5\mu\text{m}$.

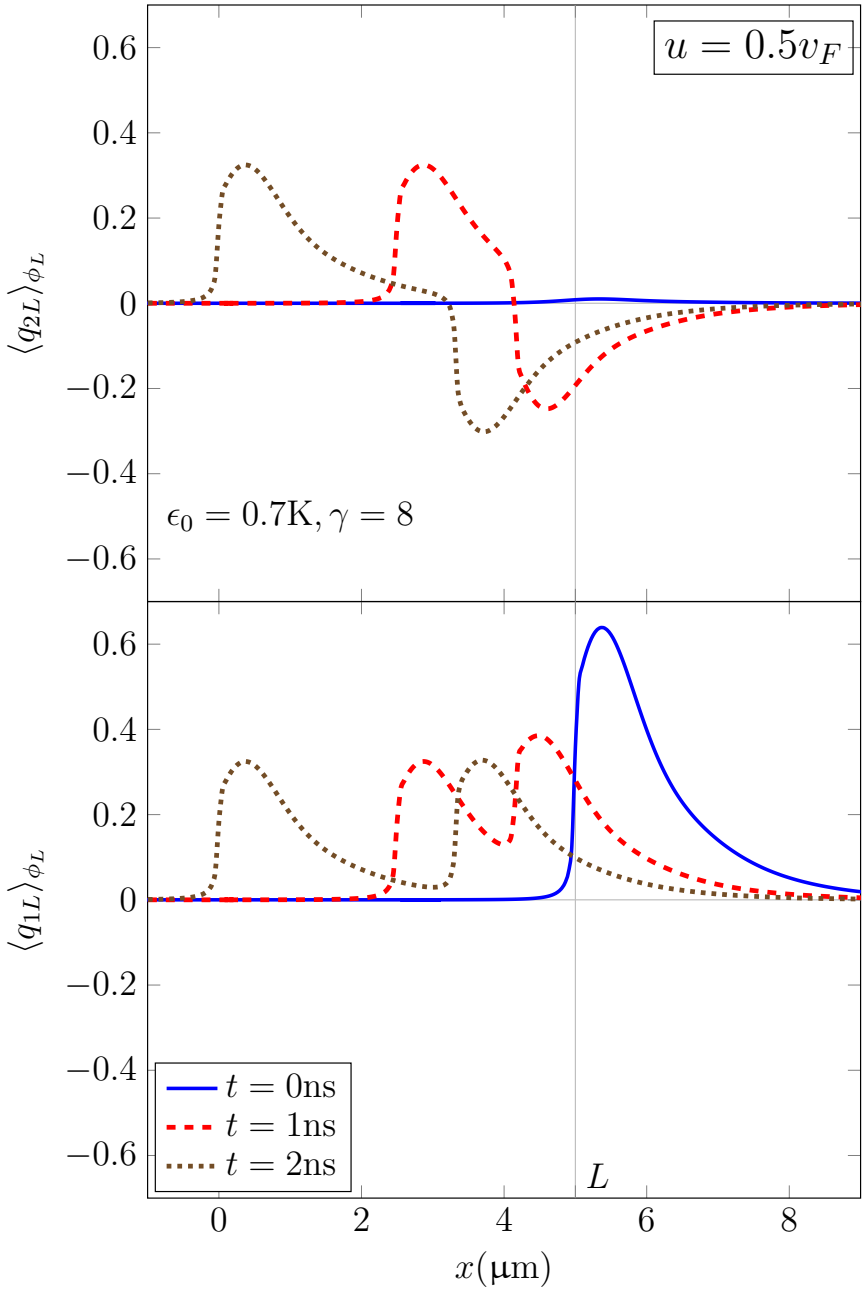

Figure 5.2: Charge density on the outer (bottom panel) and inner (top panel) left moving channels, for energy resolved packets and $u = 0.5v_F$. The injection position is $l = 5\mu$m, and the charge density is imaged after a propagation time $t = 0, 1$ or 2ns. As the modes propagate, they get more and more apart.

5.1.4 *Incoming noise*

The incoming noise on the QPC is the difference between the true correlations and the product of the currents averages, as stated by eq. (4.40). Both these quantities are expressed using $\mathcal{I}_1$ and $\mathcal{I}_2$, defined in eq. (4.37), which have to be computed first by substituting the Green's functions.

$$\begin{aligned}\mathcal{I}_j(y_L,z_L) = \frac{1}{2}\int dt\partial_x\Bigg\{ \quad v_+ \quad & \left(\log\left[s\left(\frac{i}{v_+}+t+\frac{x-z_L-L}{v_+}\right)\Big/s\left(\frac{i}{v_+}\right)\right]\right. \\ & \left.-\log\left[-s\left(\frac{-i}{v_+}+t+\frac{x-y_L-L}{v_+}\right)\Big/s\left(\frac{i}{v_+}\right)\right]\right) \\ + \quad \sigma_j v_- \quad & \left(\log\left[s\left(\frac{i}{v_-}+t+\frac{x-z_L-L}{v_-}\right)\Big/s\left(\frac{i}{v_-}\right)\right]\right. \\ & \left.-\log\left[-s\left(\frac{-i}{v_-}+t+\frac{x-y_L-L}{v_-}\right)\Big/s\left(\frac{i}{v_-}\right)\right]\right)\Bigg\}\end{aligned} \tag{5.5}$$

Performing the derivative over x, we get:

$$\begin{aligned}\mathcal{I}_j(y_L,z_L) = \frac{\pi}{2\beta}\int dt\Bigg\{ \quad & \left(\coth\left[\frac{\pi}{\beta v_+}(i+v_+t-z_L-L)\right]\right. \\ & \left.-\coth\left[\frac{\pi}{\beta v_+}(-i+v_+t-y_L-L)\right]\right) \\ + \quad \sigma_j \quad & \left(\coth\left[\frac{\pi}{\beta v_-}(i+v_-t-z_L-L)\right]\right. \\ & \left.-\coth\left[\frac{\pi}{\beta v_-}(-i+v_-t-y_L-L)\right]\right)\Bigg\}\end{aligned} \tag{5.6}$$

Only the imaginary part of the integrand contributes, as the real part of coth is antisymmetric. Performing substitutions, eq. (5.6) finally leads to:

$$\mathcal{I}_j \quad = \quad \frac{2i\pi}{\beta}\left(\frac{1}{v_+}+\frac{\sigma_j}{v_-}\right) \tag{5.7}$$

The important thing about this result is that $\mathcal{I}_j$ does not depend on y_L and z_L, which directly results in the cancellation of the incoming noises: $S_{ij}^{LL}=0$ with $i,j=1,2$.

Thus, in our model, the injection process is noiseless, even though both left-moving channels are interacting. One could have expected non-zero cross-correlations, as a result of inter-channel interactions. In fact, the noise is canceled because it is computed at zero-frequency. This information matters, insofar as the incoming noises contribute to the outgoing noise from the QPC, see eq. (4.42).

5.2 HANBURY BROWN AND TWISS EXPERIMENT

Since the incoming noises are zero (see section 5.1.4), the HBT noise is given by the mixed term, up to a prefactor: $S_{\mathrm{HBT}} = (ev_F)^2\mathcal{R}\mathcal{T}\mathcal{M}$. For both HBT setups, this term is made explicit in eq. (4.48), in which appear the following quantities: $\mathcal{A}_{\pm L}(-t,-t';z_L+L)$ and $-\mathcal{A}^*_{\pm L}(-t,-t';y_L+L)$. These ones are easily computed from their definitions, eq. (4.45). We finally make the substitutions $t \to t+\tau$ and $t' \to t$, and we get for setup s:

$$\begin{aligned} S_{\mathrm{HBT}} &= -\frac{2e^2\mathcal{R}\mathcal{T}}{(2\pi)^3\mathcal{N}}\mathrm{Re}\left\{\int dy_L dz_L\, \varphi_L(y_L)\varphi_L^*(z_L)g(0,z_L-y_L)\right. \\ &\qquad \left.\int dt\, d\tau\, \mathrm{Re}\Big[g(\tau,0)^2\Big]\left[\frac{h_s(t;y_L+l,z_L+l)}{h_s(t+\tau;y_L+l,z_L+l)}-1\right]\right\}, \end{aligned} \tag{5.8}$$

with

$$g(t,x) = \left[\frac{s\left(\frac{i}{v_+}\right)}{s\left(\frac{i}{v_+}+t-\frac{x}{v_+}\right)}\frac{s\left(\frac{i}{v_-}\right)}{s\left(\frac{i}{v_-}+t-\frac{x}{v_-}\right)}\right]^{1/2} \tag{5.9}$$

$$h_s(t;x,y) = \left[\frac{s\left(\frac{i}{v_+}-t+\frac{x}{v_+}\right)}{s\left(\frac{i}{v_+}+t-\frac{y}{v_+}\right)}\right]^{1/2}\left[\frac{s\left(\frac{i}{v_-}-t+\frac{x}{v_-}\right)}{s\left(\frac{i}{v_-}+t-\frac{y}{v_-}\right)}\right]^{3/2-s}. \tag{5.10}$$

Electron transport through a QPC is a noisy process because of its random character. At filling factor one, the noise caused by the partitioning of one electron reaches $e^2\mathcal{R}\mathcal{T}$ (in absolute value) at most at zero temperature, and is reduced at finite temperature. This reduction factor depends on the overlap between the Fermi distribution and the electronic wave-packet.

At filling factor two, two excitations are partitioned at the QPC instead. The resulting noise also depends on the energy contents of the emitted wave-packets: it increases (in absolute value) with the energy resolution γ of the packet. As a single electron injected above the FS relaxes, it creates particle-hole pairs near the Fermi energy [23], which scatter at the QPC. The number of these pairs rises with γ, since more room is available for them to be created. $|S_{\mathrm{HBT}}|$ counts the number of partitioned excitations [76], hence its energy-resolution dependence. The additional electron-hole pairs are also more numerous for a stronger inter-channel interaction u, leading to an increased noise. Both these behaviors are illustrated in fig. 5.3: the noise is higher for energy-resolved wave-packets ($\gamma = 8$, bottom panel) than for wave-packets large in energy ($\gamma = 1$, top panel), and increases with u.

Let us remind here that l is the injection position of the electronic wave-packet, which then propagates towards the QPC located at $x = 0$. The most

striking difference with the non-interacting case is simply that the noise depends on l. Without interactions, the energy contents of the wave-packet are not modified during propagation. At filling factor 2, the dependence on the propagation length is governed by two opposing effects.

On the one hand, when l rises, the distance between the fast and slow modes increases, just as when the propagation time t is increased, as depicted in fig. 5.2. While the eigenmodes are dragged apart, the number of particle-hole pairs increases, leading to the same increase in the noise.

On the other hand, at finite temperature, $|S_{\mathrm{HBT}}|$ is dramatically reduced because of anti-bunching with thermal excitations at the output of the QPC [17]. This effect accounts for the noise decrease at filling factor one, where the reduction factor scans the overlap in energy between the wave-packet and the Fermi distribution (see section 2.3.1.1). The anti-bunching effect dependence on the injection energy of the wave-packet is the same for filling factor $\nu = 2$. In both cases, the lower ϵ_0, the lower the noise. In fig. 5.3, the noise (in absolute value) is indeed more reduced for wave-packets large in energy (top panel), which are injected much nearer to the FS ($\epsilon_0 = 175\mathrm{mK}$), than for energy-resolved wave-packets (bottom panel), injected higher above the FS ($\epsilon_0 = 0.7\mathrm{K}$).

Furthermore, the noise is also reduced by the temperature, since thermal excitations spread in energy space around E_F. This is confirmed later in chapter 7 when studying the zero temperature case. The same tendency is obtained at $\nu = 1$, as the maximum value of $|S_{\mathrm{HBT}}|$ is recovered for $\Theta = 0$. Anti-bunching thus minimizes the contribution to the noise from low-energy particles. The finite temperature consequently acts as a low-energy cutoff, washing out the length dependence of the noise, which typically is constant for $l \geq 2\mu\mathrm{m}$, at $\Theta = 0.1\mathrm{K}$.

The small l behavior of the noise depends on the considered setup. Typically, for setup 1, the noise is reduced from its $l = 0$ value to its steady value. The injected wave-packet collapses onto low energy electron-hole pairs which anti-bunch with thermal excitations, thus reducing the noise. On the contrary, for setup 2, the noise is increased when l rises (see fig. 5.3). As the wave-packet propagates, more and more electron-hole pairs are created on the co-propagating channel, initially empty.

Furthermore, the length at which the noise becomes constant decreases when u is increased. Indeed, the stronger the interaction is, the quicker the electron relaxes and decoheres, and thus the quicker the noise steady value is reached.

Finally, the steady value of S_{HBT} is independent of the setup, signaling that the partition noise made by an excitation does not depend on its charge. As a consequence of charge fractionalization, both HBT setups probe the partitioning of a fast excitation, and then of a slow one. More exactly, they probe the interference between a fast and a slow excitation, with the FS incoming from

the opposite arm. In this sense, HBT interferometry is a peculiar case of HOM interferometry. In setup 1, both excitations are $\oplus$-charged, whereas the fast one is $\oplus$-charged and the slow one is $\ominus$-charged in setup 2 (see fig. 5.2).

Similarly, the noise is independent of the charge at $\nu = 1$, since the hole HBT interferometry yields the same result as the electron HBT interferometry (see section 2.3.2.1).

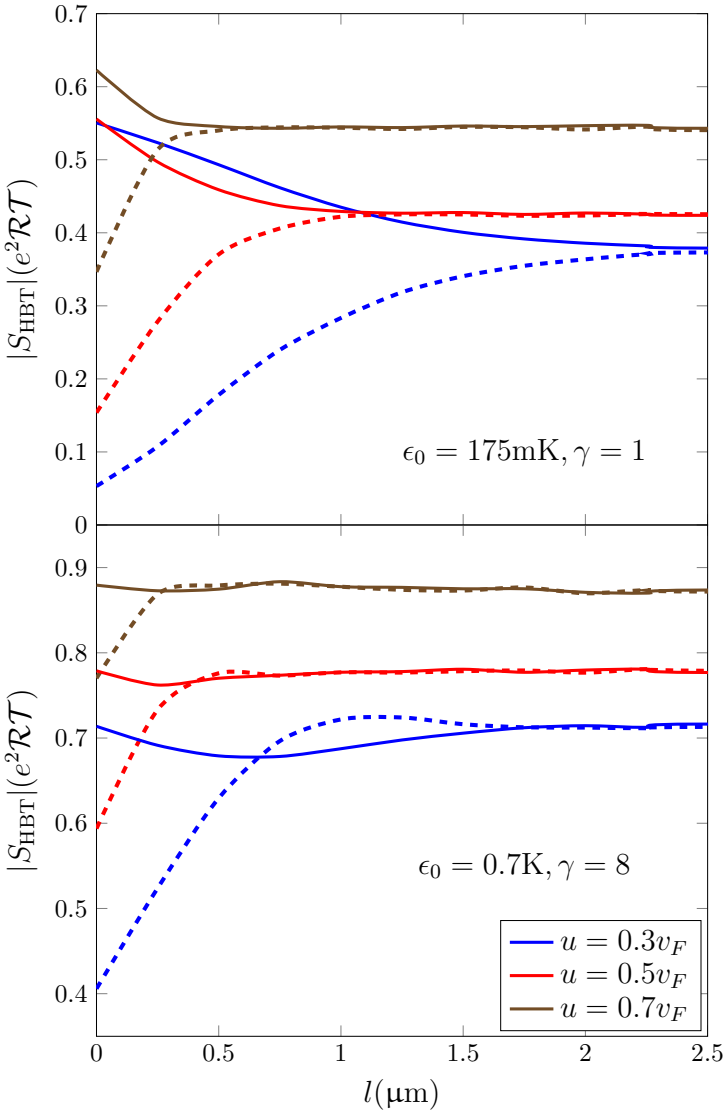

Figure 5.3: $|S_{\mathrm{HBT}}|$ at $\Theta = 0.1\mathrm{K}$ as a function of the propagation length l for wave-packets large in energy (top panel) and energy resolved wave-packets (bottom panel), for several interaction strengths. The plain curves stand for setup 1 and the dashed ones setup 2. The noise (in absolute value) rises with the interaction strength, the injection energy and the energy resolution of the wave-packet. In setup 1, it is decreased from its $l = 0$ value to its steady value. In setup 2, the noise rises until it reaches its final value. The length from which the noise is constant decreases with u.

5.3 HONG-OU-MANDEL EXPERIMENT

Depending on the setup, the HOM experiment can probe the interferometry between excitations with different charges or not. Indeed, for setup 1, two $\oplus$-excitations will meet with two other $\oplus$-excitations at the QPC. Whereas for setup 2, a $\oplus$-excitation and a $\ominus$-excitation interfere with another $\oplus$ and $\ominus$-excitation (see fig. 5.4). The HOM noise, for setup s, is obtained from eq. (4.52):

$$\begin{aligned} S_{\mathrm{HOM}}(\delta T) &= -\frac{2e^2\mathcal{R}\mathcal{T}}{(2\pi a)^4\mathcal{N}^2}\mathrm{Re}\Bigg\{\int dy_L dz_L\, \varphi_L(y_L)\varphi_L^*(z_L)g(0,z_L-y_L) \\ &\times \int dy_R dz_R\, \varphi_R(y_R)\varphi_R^*(z_R)g(0,y_R-z_R)\int d\tau\,\mathrm{Re}\left[g(\tau,0)^2\right] \\ &\times \int dt\left[\frac{h_s(t;y_L+L,z_L+L)}{h_s(t+\tau;y_L+L,z_L+L)}\frac{h_s(t+\tau-\delta T;L-y_R,L-z_R)}{h_s(t-\delta T;L-y_R,L-z_R)}-1\right]\Bigg\}. \end{aligned} \tag{5.11}$$

with the functions g and h_s defined in eq. (5.9) and (5.10) respectively.

As the time delay δT between the right- and left-moving electron is varied, we find three characteristic signatures in the noise (see fig. 5.5 and 5.6). At $\delta T = 0$, a central dip appears, and at $\delta T = \pm l(v_+ - v_-)/(v_+v_-) = \pm 2lu/(1-u^2)$, side structures emerge symmetrically with respect to the central dip. Away from these three features, S_{HOM} saturates at twice the HBT noise: electrons injected on the two incoming arms scatter independently at the QPC. This large δT value of the HOM noise does not depend on l anymore, as we consider $l \geq 2\mu$m, for which the propagation length dependence of S_{HBT} is washed out (see fig. 5.3).

The three structure interference pattern is interpreted in terms of the different excitations propagating along the partitioned edge channel. After injection, the electron fractionalizes into two modes. The fast charged mode is composed of two $\oplus$-excitations. The slow neutral mode is made out of a $\oplus$-excitation propagating along the injection channel and a $\ominus$-excitation traveling along the co-propagating channel. The central dip, which corresponds to the symmetric situation of synchronized injections, thus, probes the interference of excitations with the same velocity and charge: two fast $\oplus$-excitations then two slow $\oplus$ or $\ominus$ excitations, for setup 1 and 2 respectively (see fig. 5.4). These identical excitations interfere destructively, leading to a reduction of the noise (in absolute value), thus, producing a dip. Note that the bottom of this dip is practically insensitive to the chosen setup (and thus, to the partitioned channel) signaling that the interference between identical excitations is independent of the charge they carry. This is once again a signature of electron-hole symmetry of the system.

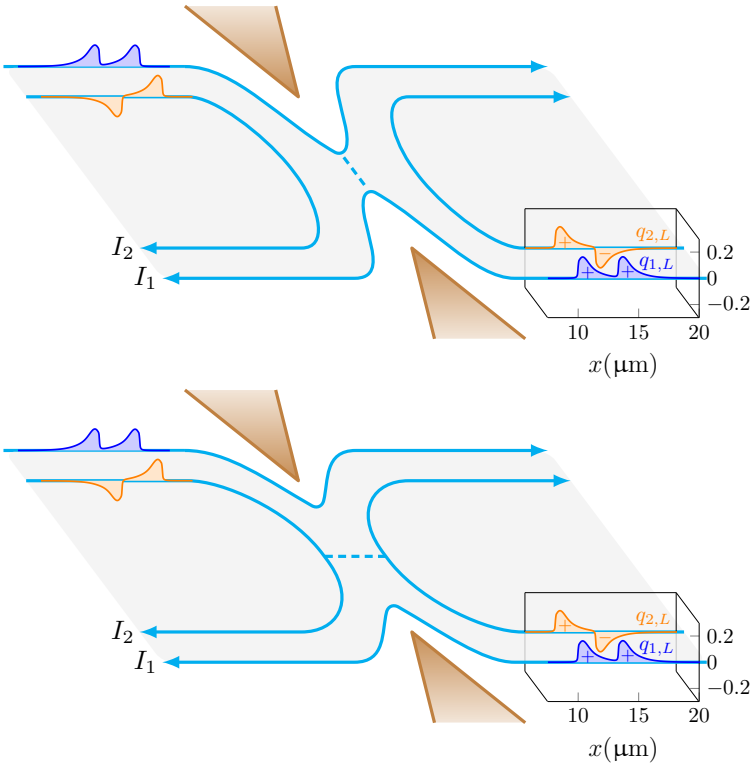

Figure 5.4: An electronic wave-packet is injected on both incoming outer channels. (Right insets) Electron density as a function of position for an energy-resolved packet imaged after propagating on a 5µm length, revealing the presence of two modes composed each of two ⊕/⊖ excitations. (Top) Setup 1: backscattering occurs for the outer channels. (Bottom) Setup 2: backscattering occurs for the inner channels.

A striking difference with the $\nu = 1$ case is that the central dip never reaches down to 0, as observed experimentally (see fig. 2.10). The depth of this dip is actually a probing tool of the degree of indistinguishability between the colliding excitations [29]. Our present work suggests that because of the strong inter-channel coupling, some coherence is lost in the co-propagating channels, and the Coulomb-induced decoherence leads to this characteristic loss of contrast for the Pauli dip.

This effect gets more pronounced for further energy-resolved packets. While for wide packets in energy the contrast is still pretty good (see fig. 5.5), $\eta = 1 - |S_{\mathrm{HOM}}(0)|/(2|S_{\mathrm{HBT}}|) \sim 0.8$ for $\gamma = 1$, the loss of contrast can be dramatic for energy-resolved packets (see fig. 5.6), with $\eta \sim 0.4$ for $\gamma = 8$. The same trend is observed in experiments [14]. When an energy-resolved wave-packet, injected high above the FS ($\epsilon_0 = 0.7$K), relaxes because of interactions, its energy distribution is very much modified. Indeed, it will collapse onto low energy lying particle-hole pairs. Thus, much information is lost during this process and the interference with the other incoming packet is weaker. On the contrary, a packet large in energy, injected near the FS ($\epsilon_0 = 175$mK), will less decohere as its energy is already quite low. Consequently, the degree of indistinguishability of two such packets is higher, and their interference is stronger, resulting in a deeper dip.

Adjusting δT appropriately, one can also probe interferences between excitations that have different velocities. This effect is responsible for the side structures appearing in the noise, whose positions scale like l. At $\delta T = 2lu/(1-u^2)$ for example, the fast right-moving excitation and the slow left-moving one reach the QPC at the same time. The two remaining excitations are partitioned independently, and add the contribution S_{HBT} to the noise.

In setup 1, these lateral structures correspond to the collision of two $\oplus$-excitations (see fig. 5.4, at the top), which interfere destructively, as they carry the same charge. This destructive interference leads to dips. Their depth is, however, less than half the one of the central dip (see fig. 5.5 and 5.6, at the top). This can be attributed to the velocity mismatch between interfering excitations. Indeed, the loss of contrast of the central dip has already proven that a reduced degree of indistinguishability between the colliding excitations leads to a weaker interference. In the same spirit, for the lateral dips, the difference between the velocities of the excitations makes them even more distinguishable, which results in even smaller dips. Furthermore, this interpretation is confirmed by previous results at filling factor one, where the interference of two packets with different shapes leads to a dip with reduced contrast (see fig. 2.8).

More interestingly, setup 2 allows us to probe the encounter of excitations with opposite charge (see fig. 5.4, at the top), which is expected to lead to constructive interference. Indeed, at $\nu = 1$ the electron-hole interferometry leads to a peak rather than a dip, in the HOM noise, as detailed in section 2.3.2.2. The value of this peak depends on the overlap of the electron and the hole wave-packets ($\varphi^e(k)\varphi^h(k)^*$). This is consistent with the occurrence of lateral peaks in our calculations at $\nu = 2$ (see fig. 5.5, bottom panel). They are more

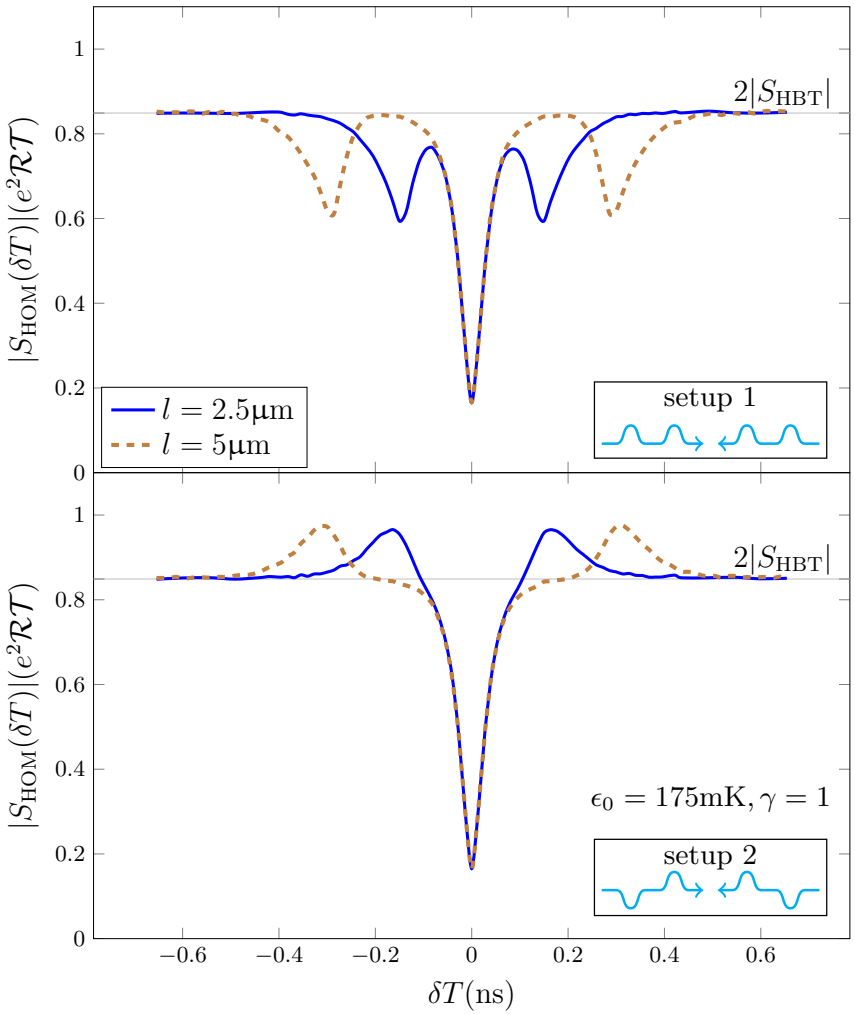

Figure 5.5: Modulus of S_{HOM} in units of $e^2\mathcal{RT}$ as a function of the time delay δT, for setup 1 (top panel) and setup 2 (bottom panel), with $u = 0.5v_F$ and $\Theta = 0.1\mathrm{K}$, for packets wide in energy. The contrast is quite good and the central dip depth does not depend on the setup. Results for setup 1 reveal a triple dip structure, with the lateral dips being less than half the central one. For setup 2 we obtain a peak-dip-peak structure. All the lateral dips and peaks are asymmetric.

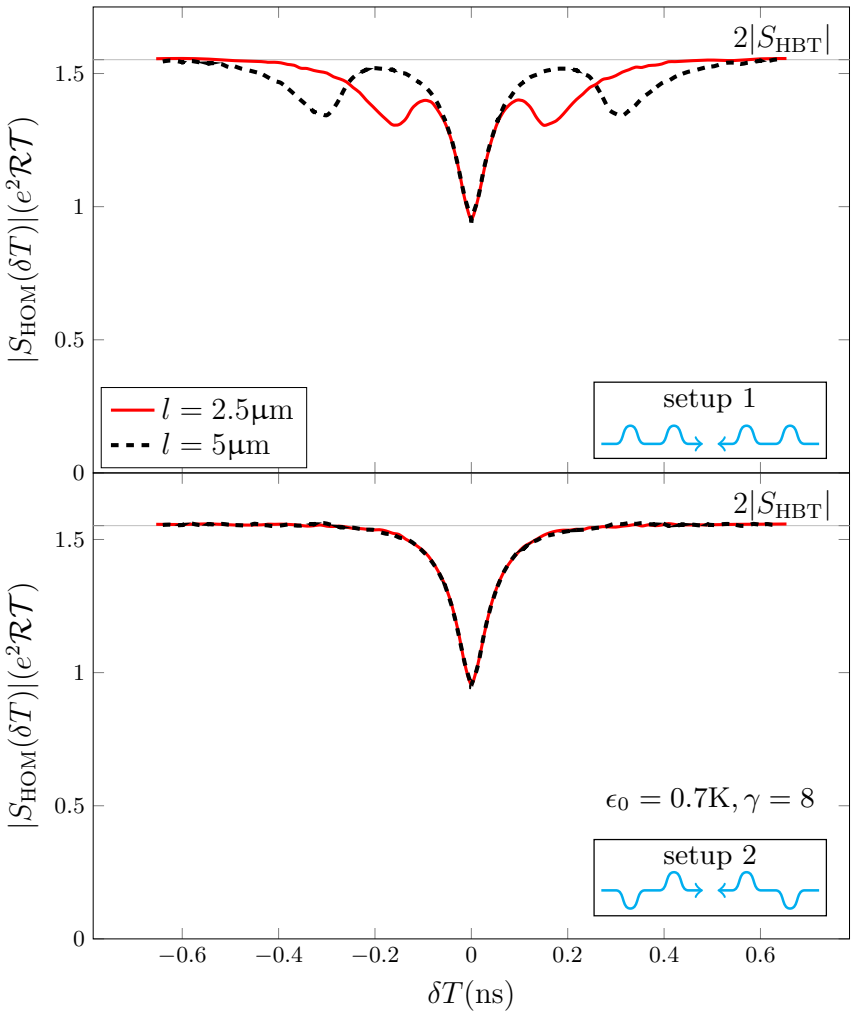

Figure 5.6: Same as figure 5.5, for energy-resolved packets. The loss of contrast of the central dip is dramatic. Three dips are still observed for setup 1, with an additional loss of contrast and an asymmetry for the lateral ones, but no peak is observed for setup 2.

pronounced for small γ, and become vanishingly small for larger values of the energy resolution (see fig. 5.6, bottom panel), signaling a nontrivial dependence on the packet energy contents. One can guess from the $\nu = 1$ results that the $\oplus$- and $\ominus$-excitations created by an energy-resolved wave-packet cannot overlap in energy, whereas this is possible for a large wave-packet in energy, created at a lower energy.

All these lateral dips and peaks are asymmetric as a consequence of the velocity difference between excitations. Typically, the slope is steeper for smaller $|\delta T|$. This asymmetry is similar to the one encountered in the non-interacting case for interfering packets with different shapes, where a broad right-moving packet in space collides onto a thin left-moving one (see fig. 2.8).

Our approach is general enough to be extended to regimes that have yet to be explored experimentally, such as electron-hole interferometry, where an electron is injected on one edge, while a hole is injected on the other edge (see fig. 5.7). There, we recover three structures in the noise. For both setups, at $\delta T = 0$, $\oplus$-excitations interfere constructively with $\ominus$-excitations, leading to a central peak. The top of this peak does not depend on the considered setup. However, while setup 1 shows lateral peaks produced by interfering oppositely charged excitations, setup 2 probes the interference of excitations carrying the same charge, leading to lateral dips. These lateral structures are also asymmetric as a consequence of the velocity mimatch between the colliding excitations. Finally, the lateral dips obtained for setup 2 are more pronounced than the lateral peaks in setup 1. This proves that the constructive interference ($\oplus/\ominus$) is weaker than the destructive one ($\oplus/\oplus$ or $\ominus/\ominus$).

Results concerning the dependence of the central dip depth on the energy width of the packet are presented in fig. 5.8, for an injection well above the FS ($\epsilon_0 = 0.7$K). First, the HBT noise does not depend much on Γ. The central dip, however, sinks drastically as Γ is increased, leading to a much higher contrast. The more resolved a packet is in energy, the more it decoheres and becomes distinguishable from its symmetric incoming packet, and the worse the contrast. A thin wave-packet energy distribution is indeed very distorted during propagation, as plenty of room is available for it to decohere. Thus, it looses a lot of quantum information, which ultimately leads to a considerable loss of contrast.

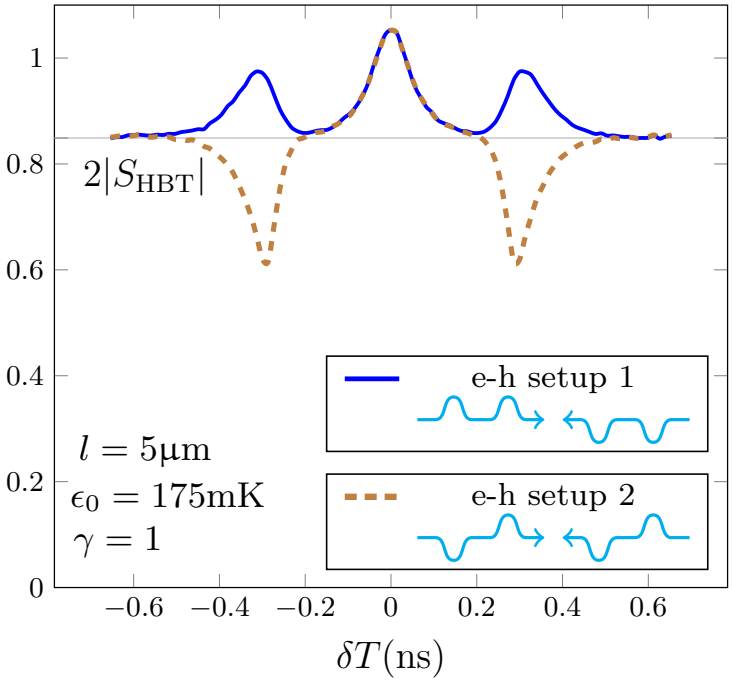

Figure 5.7: Modulus of S_{HOM} in units of $e^2\mathcal{R}\mathcal{T}$ as a function of the time delay δT, for setups 1 and 2, with $u = 0.5v_F$ and $\Theta = 0.1\mathrm{K}$. Electron-hole interference: an electron has been injected on the right moving arm and a hole on the left moving one. Constructive interference is weaker than destructive interference.

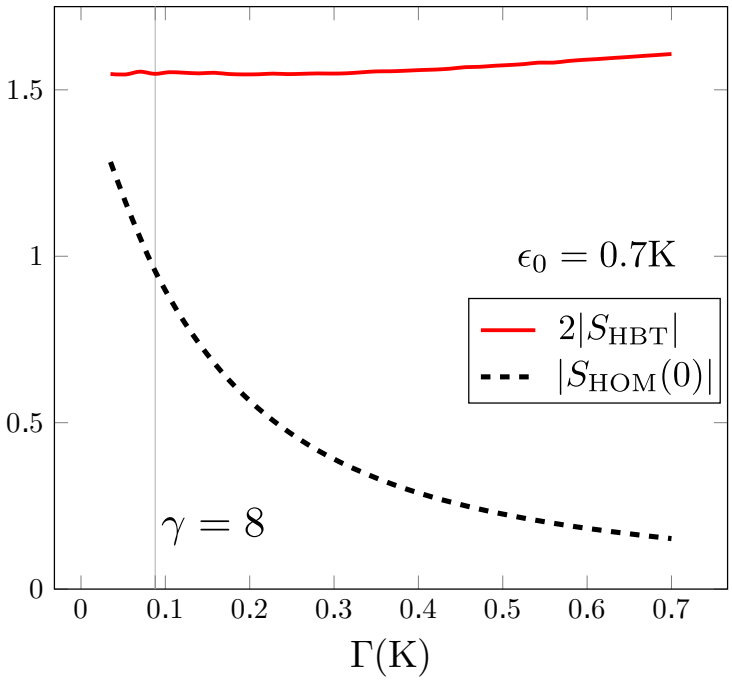

Figure 5.8: Modulus of $S_{\mathrm{HOM}}(0)$ and $2S_{\mathrm{HBT}}$ in units of $e^2\mathcal{R}\mathcal{T}$ as a function of Γ, for $\epsilon_0 = 0.7\mathrm{K}$. $u = 0.5$ and $\Theta = 0.1\mathrm{K}$. The larger the wave-packet, the better the contrast.

5.4 CONCLUSION

To conclude, strong coupling between the co-propagating channels makes an injected electron fractionnalize into two modes, each made out of two excitations, propagating with different velocities. On the outer channel, both excitations carry the charge $\oplus$, whereas the fast one is $\oplus$-charged and the slow one is $\ominus$-charged on the inner channel. Setup 1 probes the interference between two $\oplus$-excitations with the FS of the other incoming arm -in the HBT experiment-, or with the symmetric excitations -in the HOM experiment-. In setup 2, one $\oplus$-excitation and one $\ominus$-excitation encounter either the FS, or the symmetric excitations.

As the wave-packet propagates, it collapses onto low energy electron-hole pairs, whose number is counted by the HBT noise. But this latter is reduced because of anti-bunching between the fractionalized excitations and the thermal ones. The intensity of this effect depends on the initial wave-packet parameters, as the lower it is injected in energy, the more its energy contents will overlap with the FS, and the stronger the anti-bunching. As a consequence, the propagation length dependence of the noise is washed out by the finite temperature, which acts as a low energy cutoff. Moreover, once the final value of the HBT noise is reached, it does not depend on the considered setup: the partition noise made by a $\oplus$- and a $\ominus$-excitation is the same.

The main result of this part is the obtained sensible loss of contrast of the HOM central dip, as observed in the experiment. This reduction factor strongly depends on the energy resolution of the emitted packets and is directly related to decoherence. The higher and the thiner a wave-packet is in energy, the more it decoheres as its energy distribution is very distorted during propagation. Consequently, a lot of information is lost in the co-propagating channel and the packet is very distinguishable from the symmetric incoming packet. When increasing the energy width of the injected packets Γ, the contrast of the central dip is enhanced, as there is less room for the packets to decohere.

Moreover, fast and slow modes do interfere with each other and, depending on the charge carried by the colliding excitations, produce smaller asymmetric dips or peaks. Two excitations with the same charge always lead to destructive interference, whereas interference is constructive for $\oplus/\ominus$ collisions. The small character of these side structures is due to the reduced degree of indistinguishability between two such excitations, as they propagate with different velocities. The asymmetry of these lateral structures, caused by the velocity mismatch, is reminiscent of the asymmetry obtained for packets with different widths. Furthermore, as l is varied, the lateral dips or peaks positions are shifted. While these have not yet been observed in the lab, we argue that upcoming experiments with better resolution should reveal such signatures es-

pecially when operating at lower excitation frequency, thus accessing a wider interval of time delays.

The predicted behavior as l is varied could be checked if lateral gates were added to the setup, modifying the propagation path before the QPC. Measurements with different injection energies and packets widths are already being processed. Possible extensions of this work include taking into account: long-range interactions between co-propagating states, interaction between opposite edges near the QPC, fractional filling factors reached for higher magnetic fields.

6

FINITE INTERACTION REGION

The loss of contrast of the HOM dip predicted in section 5.3 for realistic electronic wave-packets is absolutely dramatic, as depicted in fig. 5.6. Actually, it exceeds the obtained experimental data. A reason for this disagreement is the model used for electron injection. As the whole packet is created at the injection time, its front will experience the interaction over the length l -the distance to the QPC-. However, its tail is created at the same time and thus will experience the interaction over a length equal to l plus the width of the packet. This length is far too long, up to $2l$ (see fig. 5.1).

To solve this problem, we now consider a finite interaction region, ranging from $-l$ to $+l$. In this way, any part of the packet will be submitted to inter-channel interaction over the same length. The setup still consists in the previous quantum Hall bar, except that inter-channel interaction is switched on, on a finite region only (see fig. 6.1). Elsewhere the charge fluctuations propagate on the co-propagating channels independently.

First, we discuss a simple model describing a single chiral edge channel, with different propagation velocities depending on the position. It is relevant insofar as switching on interactions amounts to changing the propagation velocity of charge fluctuations. This study helps catching the physics in the fol-

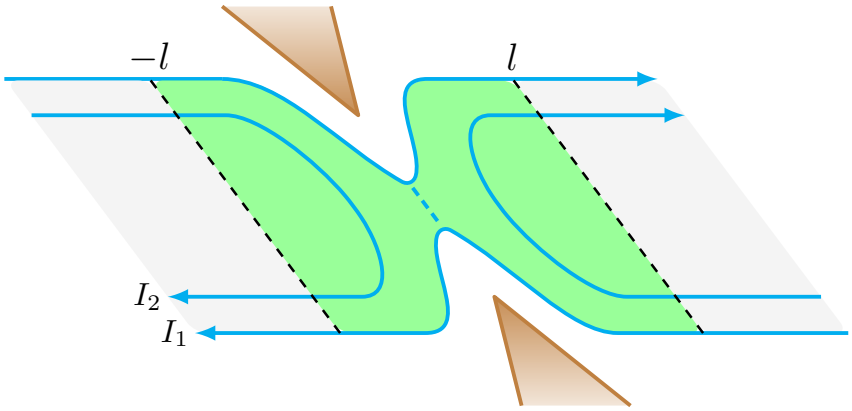

Figure 6.1: Setup 1. Inter-channel interaction is switched on in the green region only, ranging from $-l$ to l.

lowing. Then, we turn back to filling factor two and compute the relevant quantities, such as the charge density or the noise.

6.1 TOY MODEL

First, we consider a right-moving chiral edge channel, whose propagation velocity depends on position. A wave-packet is propagating: from $-\infty$ to $-l$, its velocity is $v_1 = v$, then $v_2 = w$ from $-l$ to l, and finally $v_3 = v$ again from l to $+\infty$ (see fig. 6.2). We define the packet envelope Ψ as a piecewise function, such that $\Psi(t;x) = \Psi_j(t - x/v_j)$ in region j, because of the linear dispersion in each region.

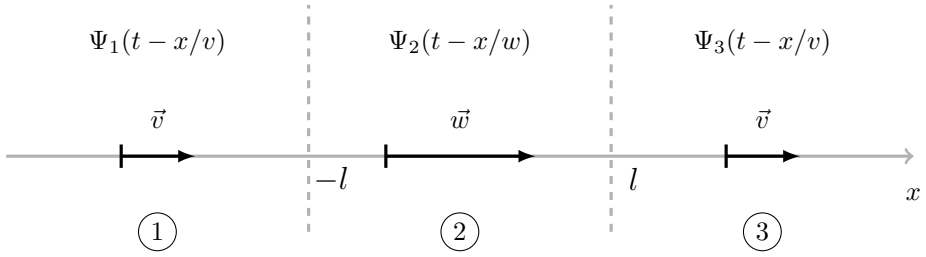

Figure 6.2: On a right-moving channel, a wave-packet propagates at velocity v in regions 1 and 3, and w in region 2. The packet envelope is a piecewise function $\Psi = \Psi_j$ in region j.

The current in region j is defined as:

$$I_j(t;x) = v_j \Psi_j(t - x/v_j) \tag{6.1}$$

The current conservation yields at $x = -l$:

$$\begin{aligned} I_2(t;-l) = I_1(t;-l) \quad &\Rightarrow \quad w\Psi_2(t + l/w) = v\Psi_1(t + l/v) \\ &\Rightarrow \quad \Psi_2(t) = \frac{v}{w}\Psi_1(t - l/W) \end{aligned} \tag{6.2}$$

with $W = 1/w - 1/v$. At $x = l$, the current conservation yields:

$$\begin{aligned} v\Psi_3(t - l/v) &= w\Psi_2(t - l/w) \\ \Rightarrow \Psi_3(t) = \frac{w}{v}\Psi_2(t + l/W) &= \Psi_1(t - 2l/W) \end{aligned} \tag{6.3}$$

In the end, current conservation implies that the envelope has the following form:

$$\Psi(t;x) = \begin{cases} \Psi_1(t;x) = \Psi_1(t - x/v) & x < -l \\ \Psi_2(t;x) = (v/w)\Psi_1(t - x/w - l/W) & -l < x < l \\ \Psi_3(t;x) = \Psi_1(t - x/v - 2l/W) & l < x \end{cases} \tag{6.4}$$

This envelope is not continuous, and this condition is required for the current -and the total charge- to be conserved.

The propagation of a Gaussian wave-packet (top panel) and an exponential one (bottom panel) is illustrated in fig. 6.3. Before the interaction region, a packet propagates without deformation at velocity v. When it reaches $x = -l$, its front starts propagating at $w > v$, whereas what is left in region 1 still propagates at velocity v. Thus, the packet spreads. But as the area under the curve has to remain unchanged, for the charge to be conserved, its value is decreased: $\Psi(t : -l^+) < \Psi(t; -l^-)$. Then, it propagates in region 2 under this wider shape. At the end of the interaction region, the front is slowed, resulting in the narrowing of the envelope, which retrieves its initial shape in region 3. Finally, it propagates again without deformation at velocity v.

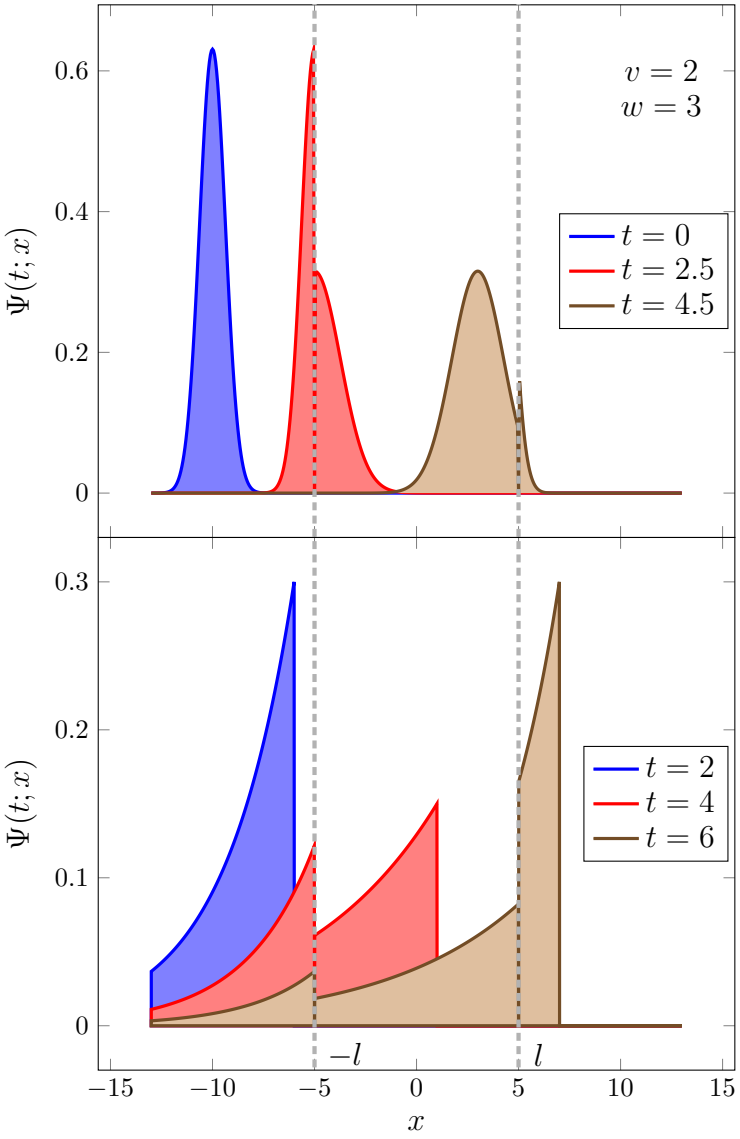

Figure 6.3: Envelopes of a Gaussian (top panel) and an exponential (bottom panel) wave-packets, which propagate toward the right at velocities $w = 3$ in the interaction region (from $-l$ to l) and $v = 2$ elsewhere. The injection position is $x = -10$ and $l = 5$. The envelope is wider when the packet travels faster, but the area under the curve remains unchanged.

6.2 PRELIMINARIES

We now turn back to the setup depicted in fig. 6.1, in which the co-propagating channels interact only for $-l < x < l$.

Like in section 5.1, we would like to use the results from chapter 4 to obtain the quantities of interest, by simply substituting the Green's functions by their expressions. However, the calculations were made for Green's functions assumed to be homogeneous. It is not the case anymore, as the propagation velocity now depends on the position.

First we compute the new Green's functions. Then, we simply deduce the new results from chapter 4 by analogy, rather than presenting the whole computation over again.

6.2.1 *Intra-channel interactions*

In this chapter, we are seeking a more quantitative agreement with experimental data. Consequently, we take intra-channel interactions into account as well as inter-channel interactions: $U \neq 0$. It boils down to rescaling the intrinsic velocities: $v_{1,2} \to v_{1,2} + U$. As we are still working in the strong coupling regime because of its experimental relevance (see discussion at the very beginning of part iii), one has: $v_1 = v_2 = v_F$. We now add intra-channel interactions and define the propagation velocity outside of the interaction region: $v = v_F + U$. In order to be consistent with the toy model of section 6.1, we label the fast and slow modes velocities, in the interaction region, w_+ and w_- respectively. They are defined by eq. (4.16): $w_\pm = v \pm u$.

The purpose of adding intra-channel interactions is to choose the velocities in agreement with experimental measurements. It is known from the experiment that the ratio of the fast mode velocity over the slow mode velocity is much greater than one: $w_+/w_- \gg 1$. The Fermi velocity measurement in the sample has yielded $v_F = 2.5\ 10^4 \mathrm{m.s}^{-1}$ and the slow mode velocity: $w_- = 4.6\ 10^4 \mathrm{m.s}^{-1}$. The fact that $w_- > v_F$ already proves that intra-channel interactions are present (otherwise, one would have $v_- = v_F - u < v_F$). If one sets v_F and w_- according to the experimental values, and sets the ratio w_+/w_- arbitrarily, both interaction strengths u and U are found.

6.2.2 *Green's functions*

Apart from the inter-channel interaction, the Hamiltonian describes two edge states made out of two channels each, in the strong coupling regime:

$$H_{\text{kin}} + H_{\text{intra}} = \frac{\hbar}{\pi} v \sum_{r=R,L} \sum_{j=1,2} \int dx (\partial_x \phi_{jr})^2 \tag{6.5}$$

with $v = 1 + U$. The inter-channel interaction is only present in a restricted region of the system:

$$H_{\text{int}} = 2\frac{\hbar}{\pi} u \sum_r \int_{-l}^{l} dx (\partial_x \phi_{1r})(\partial_x \phi_{2r}) \tag{6.6}$$

The total Hamiltonian can thus be diagonalized as:

$$H = \frac{\hbar}{\pi} \sum_r \int dx \left[v_+(x)(\partial_x \phi_{+r})^2 + v_-(x)(\partial_x \phi_{-r})^2 \right] \tag{6.7}$$

where

$$v_\pm(x) = \begin{cases} v & = 1 + U \qquad x < -l \quad \text{or} \quad x > l \\ w_\pm & = 1 + U \pm u \quad -l \le x \le l \end{cases} \tag{6.8}$$

In practice, we are interested in the correlator: $G_{\pm r}(t; x, x') = \langle \phi_{\pm r}(x,t) \phi_{\pm r}(x',0) \rangle = \langle \phi_{\pm r}(x,0) \phi_{\pm r}(x',-t) \rangle$. And using that $\partial_t \phi_{\pm r}(x,t) = \partial_t \left(e^{iHt} \phi_{\pm r}(x) e^{-iHt} \right)$, one has:

$$\begin{aligned} \partial_t G_{\pm r}(t; x, x') = & \quad -\sigma_r v_\pm(x) \partial_x \partial_t \quad G_{\pm r}(t; x, x') \\ = & \quad +\sigma_r v_\pm(x') \partial_{x'} \partial_t \quad G_{\pm r}(t; x, x') \end{aligned} \tag{6.9}$$

with $\sigma_R = 1$ and $\sigma_L = -1$. It follows that the correlator is a function of the argument:

$$t - \sigma_r \left(\frac{x}{v_\pm(x)} - \frac{x'}{v_\pm(x')} \right). \tag{6.10}$$

In fact, using eq. (5.1) and the previously studied toy model, we make the assumption that the Green's functions now read:

$$\begin{aligned} G_{\pm R}(t; x, y) &= -\log \left[s\left(\frac{i}{v} - t + f_{\pm R}(x) - f_{\pm R}(y) \right) \Big/ s\left(\frac{i}{v} \right) \right] \\ G_{\pm L}(t; x, y) &= -\log \left[s\left(\frac{i}{v} - t - f_{\pm L}(x) + f_{\pm L}(y) \right) \Big/ s\left(\frac{i}{v} \right) \right] \end{aligned} \tag{6.11}$$

with

$$f_{\pm R}(x) = \begin{cases} x/v & x < -L \\ x/w_\pm + L/W_\pm & -L \le x \le L \\ x/v + 2L/W_\pm & L < x \end{cases}$$

$$f_{\pm L}(x) = \begin{cases} x/v - 2L/W_\pm & x < -L \\ x/w_\pm - L/W_\pm & -L \le x \le L \\ x/v & L < x \end{cases} \tag{6.12}$$

and $W_\pm = 1/(1/w \pm -1/v) = \mp u/(1 \pm u)$.

6.2.3 *Normalization*

The injection position is replaced by α, as l designates the distance between the QPC and the boundary of the interaction region. Thus, the prepared state now reads:

$$|\phi_L\rangle = \int dy_L \varphi_L(y_L) \psi_{1L}^\dagger(y_L + \alpha, 0)|0\rangle \tag{6.13}$$

As $\varphi_L(y) = 0$ for $y < 0$ for exponential wave-packets, as stated by eq. (4.27), we are sure that nothing can be injected in the interaction region. By analogy with eq. (4.29), after carefully introducing the new Green's functions, we get for the norm:

$$\mathcal{N}_L = \frac{1}{2\pi} \int dy_L e^{-ik_0 y_L - \Gamma|y_L|} \frac{s(i/v)}{s\left((y_L + i)/v\right)} \tag{6.14}$$

6.2.4 *Charge fractionalization*

The charge density on both left-moving channels is obtained by analogy with eq. (4.32) and leads to:

$$\begin{aligned}
&\langle q_{jL}(x,t)\rangle_{\phi_L} \\
= \; & \frac{1}{\mathcal{N}} \frac{e\Gamma}{2i\pi^2 a} \int dy_L dz_L e^{ik_0(z_L - y_L)} e^{-\Gamma(z_L + y_L)} \theta(y_L)\theta(z_L) \\
& \left[\frac{s(i/v)}{s(i/v + f_+(y_L+\alpha) - f_+(z_L+\alpha))}\right]^{1/2} \left[\frac{s(i/v)}{s(i/v + f_-(y_L+\alpha) - f_-(z_L+\alpha))}\right]^{1/2} \\
& \Bigg\{ \frac{\pi}{\beta} f_+'(x) \left[\coth\left(\frac{\pi}{\beta}(i/v + t + f_+(x) - f_+(z_L+\alpha))\right)\right. \\
& \qquad \left. + \coth\left(\frac{\pi}{\beta}(i/v - t - f_+(x) + f_+(y_L+\alpha))\right)\right] \\
& + \sigma_j \frac{\pi}{\beta} f_-'(x) \left[\coth\left(\frac{\pi}{\beta}(i/v + t + f_-(x) - f_-(z_L+\alpha))\right)\right. \\
& \qquad \left. + \coth\left(\frac{\pi}{\beta}(i/v - t - f_-(x) + f_-(y_L+\alpha))\right)\right] \Bigg\}
\end{aligned} \tag{6.15}$$

Fig. 6.4 illustrates the propagation of an exponential wave-packet large in energy, injected at $\alpha = 5\mu$m. Before the interaction region, on the outer channel, the envelope differs from a perfect exponential shape because of the finite cutoff. On the inner channel, nothing is imaged as the fast and slow excitations propagate at the same velocity, with the same shape but opposite charges. The wave-packet propagates at velocity v until it reaches $x = l$, then the fast and slow excitations split. The fast ones spread, as the front of such

an excitation starts propagating at velocity $v_+ > v$ while the tail is still propagating at v. The slow ones are narrowed, as the front of a slow excitation is slowed down whereas the tail velocity remains the same for a while. The same phenomena were observed in our previous toy model (see fig. 6.3). The fast and slow excitations composing the charged and neutral modes have now different shapes, and they propagate under this form until the end of the interaction region. Then, at $x = -l$, the reverse process takes place: the fast excitations are slowed down and the slow ones are accelerated. Because of this abrupt change of velocity, the shapes of the charge excitations are changed once again, and they recover their initial shape, that is to say half of the initial exponential wave-packet. All excitations finally propagate at v, but the fast and slow modes have acquired the time delay $2l(1/w_+ - 1/w_-)$.

6.2.5 *Incoming noise*

Once again, we need to compute $\mathcal{I}_1$ and $\mathcal{I}_2$ first, in order to obtain the incoming noise on the QPC. They are obtained by analogy with eq. (4.37). Because of the exponential nature of the wave-packets, only $y_L, z_L > 0$ contribute. And as we set $\alpha > l$, we have $f_{\pm L}(y_L + \alpha) = (y_L + \alpha)/v$. (The same identity holds for z_L.) Furthermore, we are interested in the incoming noise at the QPC and thus x is in the interaction region, yielding: $f_{\pm L}(x) = x/w_\pm - l/W_\pm$. With these simplifications, $\mathcal{I}_j$ is obtained as:

$$\begin{aligned}\mathcal{I}_j(y_L, z_L) = \frac{1}{2}\int dt\,\partial_x\Bigg\{ \quad & w_+ \quad \left(\log\left[s\left(\frac{i}{v} + t + \frac{x}{w_+} - \frac{l}{W_+} - \frac{z_L+\alpha}{v}\right)\Big/ s\left(\frac{i}{v}\right)\right]\right. \\ & \qquad \left. -\log\left[-s\left(\frac{-i}{v} + t + \frac{x}{w_+} - \frac{l}{W_+} - \frac{y_L+\alpha}{v}\right)\Big/ s\left(\frac{i}{v}\right)\right]\right) \\ + \quad & \sigma_j w_- \quad \left(\log\left[s\left(\frac{i}{v} + t + \frac{x}{w_-} - \frac{l}{W_-} - \frac{z_L+\alpha}{v}\right)\Big/ s\left(\frac{i}{v}\right)\right]\right. \\ & \qquad \left. -\log\left[-s\left(\frac{-i}{v} + t + \frac{x}{w_-} - \frac{l}{W_-} - \frac{y_L+\alpha}{v}\right)\Big/ s\left(\frac{i}{v}\right)\right]\right)\Bigg\}\end{aligned} \tag{6.16}$$

Just as in the infinite interaction region case, the derivative over x and then the integral over t are performed. One is finally left with: $\mathcal{I}_j = 2i\pi(1+\sigma_j)/(\beta v)$. This result does not depend on y_L and z_L, which directly results in the cancellation of the incoming noises, and once again $S_{ij}^{LL} = 0$.

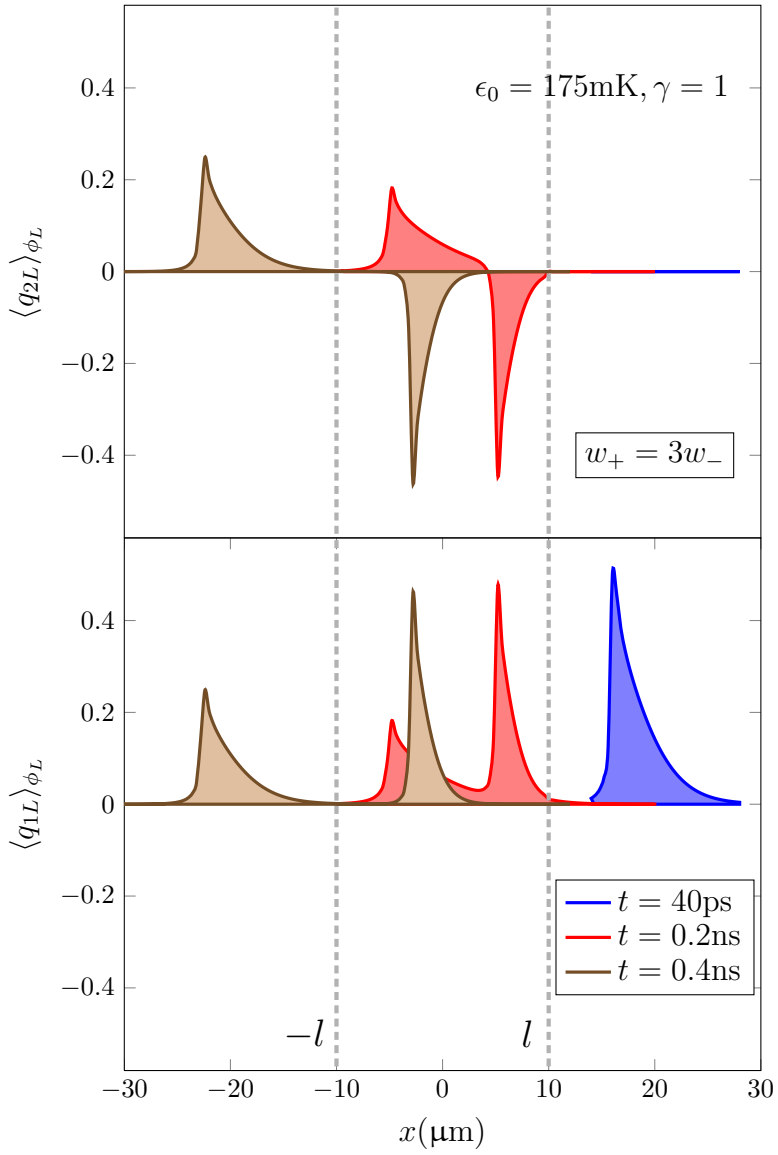

Figure 6.4: Charge density of a large wave-packet in energy on the left-moving outer channel (bottom panel) and inner channel (top panel), for an injection at $\alpha = 20\mu\text{m}$ and $t = 0$. The interaction region ranges from $-l$ to l, with $l = 10\mu\text{m}$. In this region, the fast and slow excitations have different shapes because of the velocity mismatch at the boundary $x = l$. At the interaction region output, the excitations are halves of the initial wave-packet, propagating at v again, but they have acquired a time delay.

6.3 HANBURY BROWN AND TWISS EXPERIMENT

The same kind of work can be performed to obtain the HBT noise. Basically, l is replaced by α, and the Green's functions by their new expressions. One still has to be very careful with spatial arguments, because of the additional terms in $l/W_{\pm}$. Eq. (5.8) is thus slightly modified as:

$$\begin{aligned} S_{\mathrm{HBT}} &= -\frac{2e^2\mathcal{R}\mathcal{T}}{(2\pi)^3\mathcal{N}}\mathrm{Re}\left\{\int dy_L dz_L\, \varphi_L(y_L)\varphi_L^*(z_L)g(0,z_L-y_L)\right. \\ &\left.\int dt\, d\tau\, \mathrm{Re}\left[g(\tau,0)^2\right]\left[\frac{h_s(t;y_L+\alpha,z_L+\alpha)}{h_s(t+\tau;y_L+\alpha,z_L+\alpha)}-1\right]\right\} \end{aligned} \tag{6.17}$$

with

$$g(t,x) = \frac{s\left(\frac{i}{v}\right)}{s\left(\frac{i}{v}+t-\frac{x}{v}\right)} \tag{6.18}$$

$$h_s(t;x,y) = \left[\frac{s\left(\frac{i}{v}-t+\frac{x}{v}+lW_+\right)}{s\left(\frac{i}{v}+t-\frac{y}{v}-lW_+\right)}\right]^{1/2}\left[\frac{s\left(\frac{i}{v}-t+\frac{x}{v}+lW_-\right)}{s\left(\frac{i}{v}+t-\frac{y}{v}-lW_-\right)}\right]^{3/2-s} \tag{6.19}$$

Just as in section 5.3, where inter-channels interactions span all the quantum Hall bar, the HBT noise (in absolute value) increases with the energy resolution of the wave-packet. As depicted in fig. 6.5, the noise is greater for energy-resolved packets (bottom panel, $\gamma = 8$) than for packets large in energy (top panel, $\gamma = 1$).

But in stark contrast with the infinite interaction region case, the dependence on the inter-channel interaction strength u is ruled out: whatever its value, the noise reaches the same steady value.

Moreover, S_{HBT} depends on the propagation length l under the effect of inter-channel interactions. This dependence is governed by the same opposing effects as previously: more and more electron-hole pairs are created near the FS while the interaction region length increases, leading to the same increase in the noise. But this effect is killed by the finite-temperature, which acts as a small energy cutoff.

Once again, the small l behavior of the noise depends on the considered setup. Especially, the $l = 0$ limit deserves attention. In this limit, inter-channel interactions are switched on nowhere, and we recover four quantum edge states at filling factor one. Indeed, for setup 1, we recover the value obtained from eq. (2.24), which describes the noise associated with an electronic wave-packet anti-bunching with thermal excitations. For setup 2, the limit is zero

as no excitation is created on the inner channel because of the missing coupling.

Moreover, the length at which the steady value of S_{HBT} is reached decreases with the ration w_+/w_- (or equivalently with the inter-channel interaction strength u). This behavior was already observed when inter-channel interactions were switched on everywhere (see fig. 5.3). However, S_{HBT} reaches its steady value for a longer propagation length subject to interactions, than in the infinite interaction region case. As the whole wave-packet experiences interactions over a length l (and not l plus the width of the packet, for its tail), it has to propagate longer to collapse onto the final set of electron-hole pairs. In the end, the inter-channel interaction strength u now simply determines how fast the wave-packet relaxes, but not the number of pairs created near the FS, counted by the HBT noise.

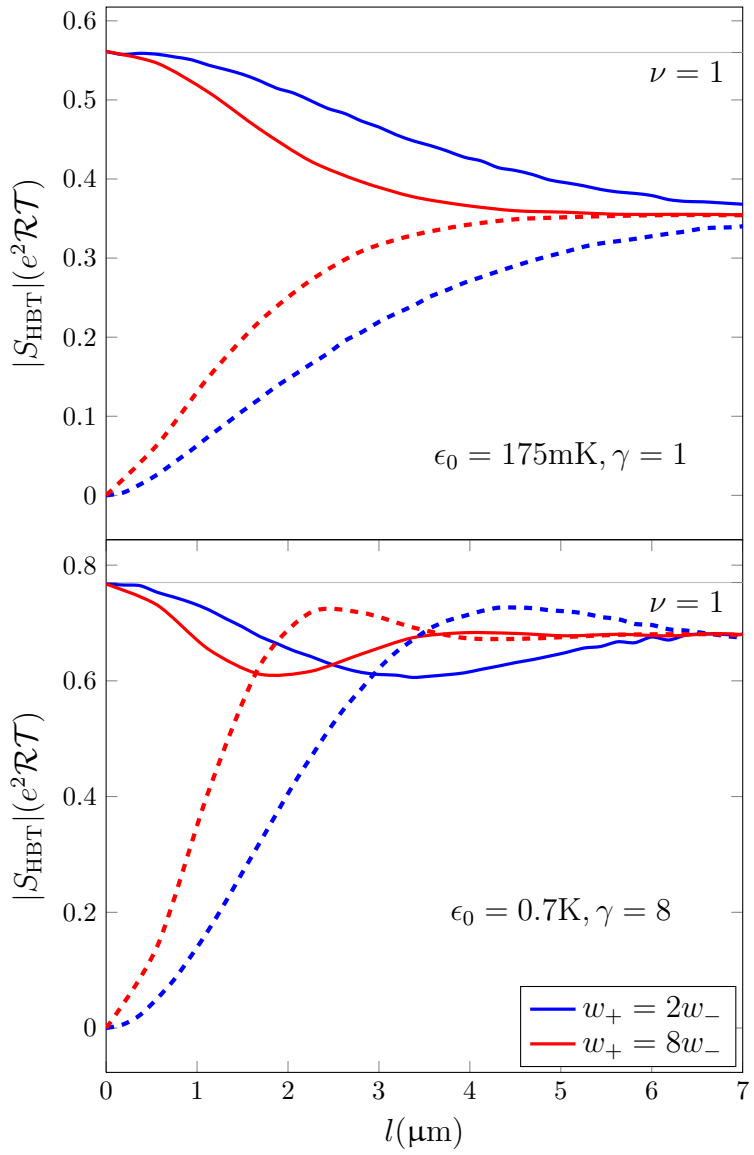

Figure 6.5: $|S_{\text{HBT}}|$ as a function of the propagation length under inter-channel interactions, for large packets in energy (top panel) and energy-resolved packets (bottom panel). For both setups, the blue curves stand for $w_+ = 2w_-$ ($u = 0.33v$) and the red ones for $w_+ = 8w_-$ ($u = 0.78v$). Typically, for $l > 7\mu$m a steady value independent of u is reached. At $l = 0$, the noise is zero for setup 2, and reduced from one for setup 1 because of anti-bunching with thermal excitations, leading to the same value as the $\nu = 1$ case.

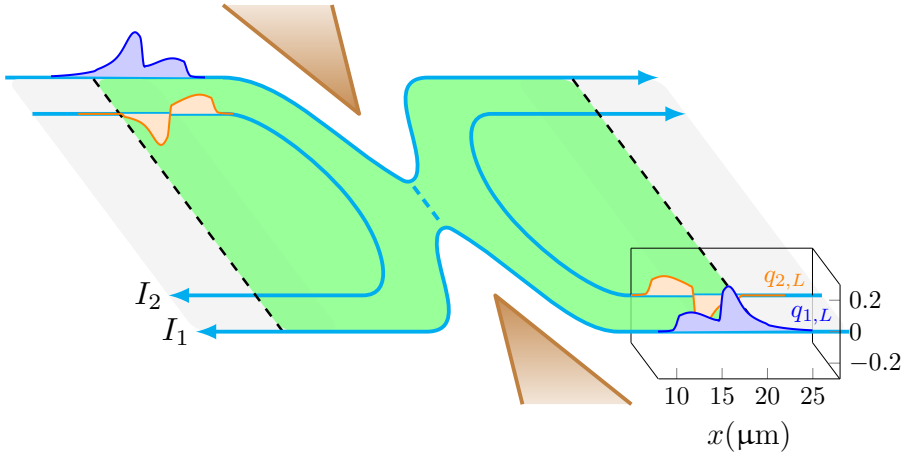

Figure 6.6: Setup 1. An electronic wave-packet is injected on both incoming outer channels. It is fractionalized when entering the interaction region (colored in green). (Right inset) Electron density as a function of position for an energy-resolved packet, injected in the non-interacting region. Inter-channel interactions are switched on between −20 and 20µm. $w_+ = 2w_-$ and the time of propagation is $t = 0.2$ns. The fast excitations are spread whereas the slow ones are narrowed.

6.4 HONG-OU-MANDEL EXPERIMENT

Two electrons are injected at positions α and $-\alpha$, outside of the interaction region, on the left- and right-moving outer channels respectively. Because of inter-channel interactions, when incoming into this region, the charges are fractionalized into a fast and a slow mode, which have different shapes (see fig. 6.6). Like in the infinite interaction region case, discussed in section 5.3, the HOM experiment probes the interference of excitations which have either the same or opposite charges, and either the same or different velocities. In addition, in the present model, interference between excitations which have different shapes is also probed.

However, we are not going to study in details the interference pattern depending on the time delay, as we did previously. Here, we are rather seeking a quantitative agreement between theoretical and experimental data, for the central dip contrast as a function of the escape time τ_e of the injected wave-packets. As discussed in section 2.3.1.2, the escape time of an electron from the capacitor is inversely proportional to the width of the emitted packet. This relation is more precisely derived in appendix, section A.2. In order to compare with the experimental data, we focus on setup 1, which is realized in practice.

Performing the same substitutions as in the HBT case, the formula for the noise is computed:

$$\begin{aligned} S_{\mathrm{HOM}}(\delta T) &= -\frac{2e^2\mathcal{R}\mathcal{T}}{(2\pi a)^4\mathcal{N}^2}\mathrm{Re}\left\{\int dy_L dz_L\, \varphi_L(y_L)\varphi_L^*(z_L)g(0,z_L-y_L)\right. \\ &\times \int dy_R dz_R\, \varphi_R(y_R)\varphi_R^*(z_R)g(0,y_R-z_R)\int d\tau\,\mathrm{Re}\left[g(\tau,0)^2\right] \\ &\times \left.\int dt\left[\frac{h_s(t;y_L+\alpha,z_L+\alpha)}{h_s(t+\tau;y_L+\alpha,z_L+\alpha)}\frac{h_s(t+\tau-\delta T;\alpha-y_R,\alpha-z_R)}{h_s(t-\delta T;\alpha-y_R,\alpha-z_R)}-1\right]\right\} \end{aligned} \tag{6.20}$$

with g and h_s being defined in eq. (6.18) and (6.19) respectively.

The most important results are illustrated in fig. 6.7: the normalized HOM noise is plotted as a function of the escape time. First, it does not reach down to zero, indicating that some coherence is lost in the inner channel, which is not partitioned. Second, $S_{\mathrm{HOM}}(0)/(2S_{\mathrm{HBT}})$ increases with the escape time, and thus with the energy resolution of the wave-packet. Both these features were already observed for inter-channel interactions spanning all the sample. In a few words, the loss of coherence is due to the loss of quantum information in the non-partitioned co-propagating channel. It is increased for energy-resolved wave-packets, as their energy distribution is very distorted while they relax towards low-energy electron-hole pairs. Thus, the degree of indistinguishability between two such packets is reduced.

The main result is that the bottom of the dip (normalized by twice the HBT noise) is lower in the finite interaction region model, and in excellent agreement with the experimental data! A better contrast is obtained, reproducing the measurements. Indeed, less coherence is lost in the co-propagating channel in this model as the whole wave-packet, and not only its front, interacts with the neighboring channel on a length l. Previously, especially in the case of large packets in real space, the tail of the packet was subject to inter-channel interactions on a much longer length. This explains why the difference between both theoretical models is greater for a larger escape time, and consequently a larger width in real space. Because of this limited length with inter-channel interactions, the packet has less time to collapse onto electron-hole pairs near the Fermi energy, and loses less information on the co-propagating channel. Thus, the degree of indistinguishability between two such packets is enhanced.

Finally, a time delay sweep of the normalized HOM noise is plotted in fig. 6.8, for energy-resolved and large in energy wave-packets, for realistic parameters: the ratio of the fast and slow mode velocities is $w_+/w_- = 3$ and the propagation length before the QPC is $l = 4\mu\mathrm{m}$. First of all, we recover the three structure interference pattern described in section 5.3. Because of the shortness of l, and since the velocities are quickened by intra-channel interactions, the side structures are shifted towards small time delays, and melt into the

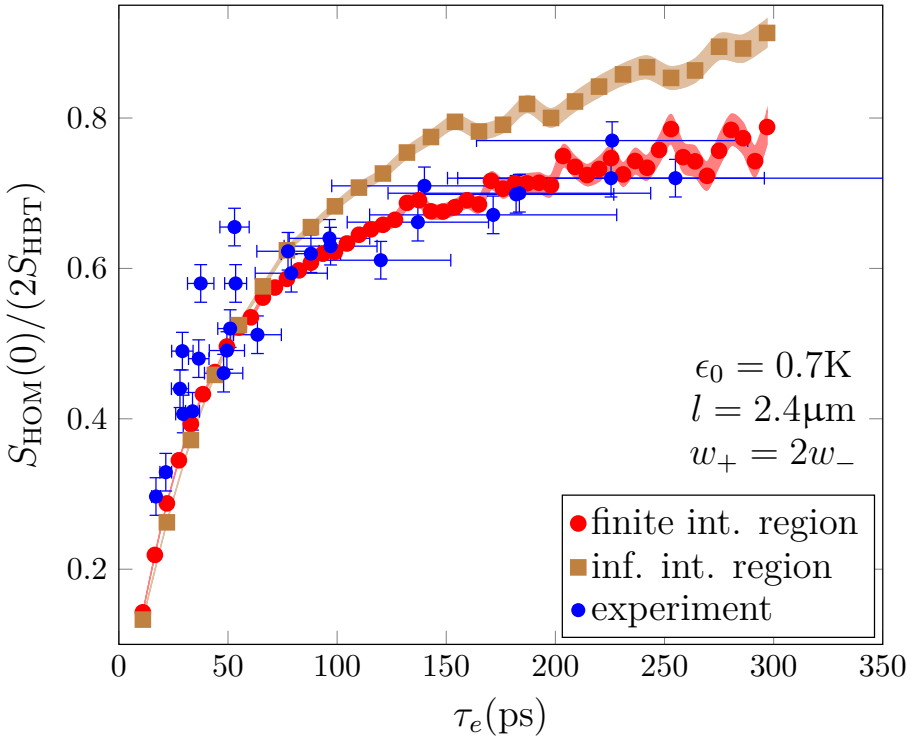

Figure 6.7: Normalized HOM noise at zero-time delay as a function of the escape time of energy-resolved wave-packets, in setup 1. $w_+ = 2w_-$, $l = 2.4\mu\mathrm{m}$ and the injection energy is $\epsilon_0 = 0.7\mathrm{K}$. The finite interaction region model is in excellent agreement with the experimental data. The bottom of the dip rises with the escape time, or equivalently the energy-resolution of the wave-packets. The higher the escape time, the wider the packets in real space, and the more pronounced the difference between the infinite and finite interaction region cases.

central dip.

Nonetheless, side dips are obtained for setup 1, for both kinds of packets. We recover destructive interference for $\oplus/\oplus$ excitations, as previously (see fig. 5.5). For setup 2, side peaks are obtained, which decrease with the energy resolution of the packets, until they become invisible for $\gamma = 8$, like in the infinite interaction region case (see fig. 5.6). As these lateral dips and peaks melt into the central dip, what is observed is a widened HOM dip for setup 1, and a narrowed one for setup 2.

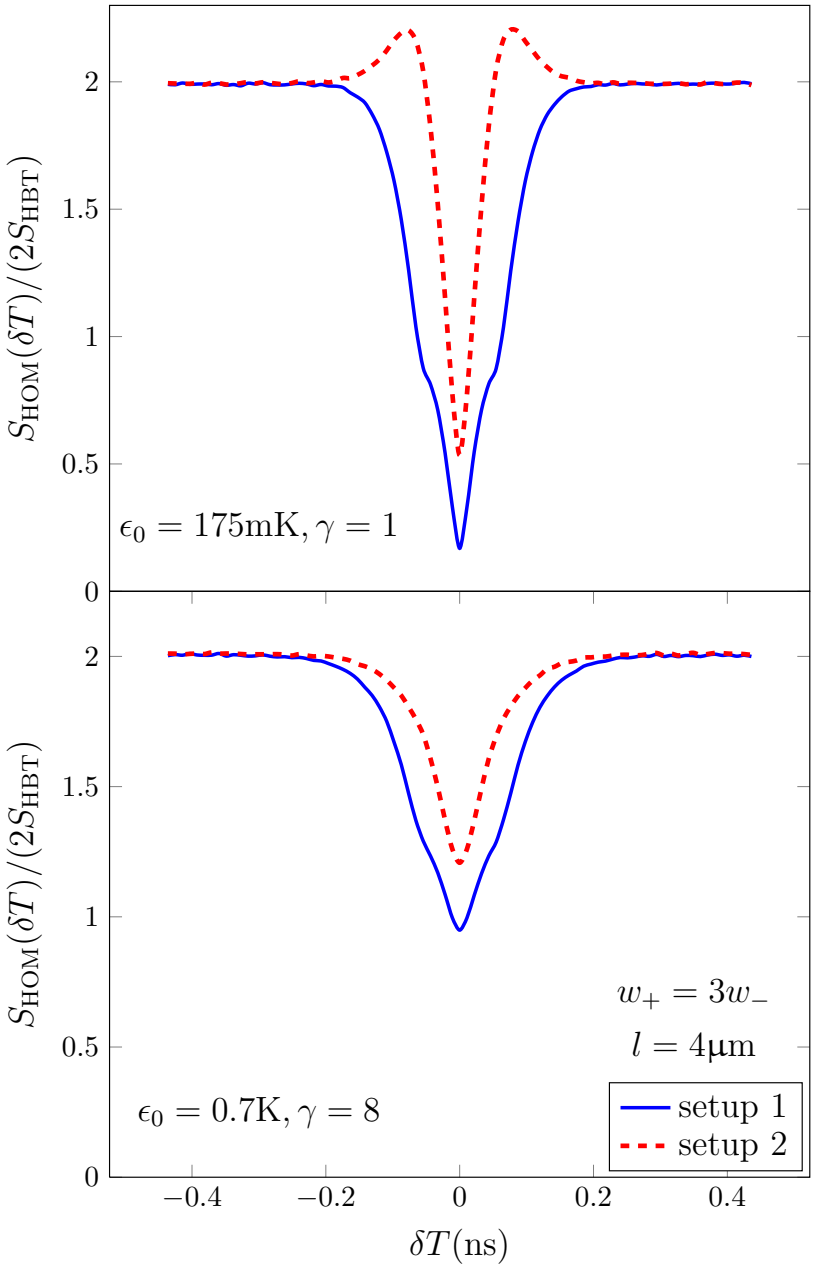

Figure 6.8: Normalized HOM noise as a function of the time delay, for packets large in energy (top panel) and energy-resolved (bottom panel). The plain curves stand for setup 1, and the dashed ones fro setup 2. The dip-dip-dip and peak-dip-peak patterns are recovered for setups 1 and 2 respectively, though the lateral structures melt into the central dip. In the end, a widened dip is observed for setup 1, and a narrowed one for setup 2.

6.5 CONCLUSION

In this chapter, we have considered a quantum Hall bar at filling factor $\nu = 2$, with intra-channel interactions, in order to be closer to the experimental conditions. Also, inter-channel interactions are switched on in a region ranging from $-l$ to l. The purpose of such a model is to get rid of artefacts caused by the model describing electron injection. Indeed, if inter-channel interactions are present in the whole sample, an electron propagating toward the QPC will experience them over a length l at the front of its wave-packet, and over longer length (depending on its width) at its tail. In this new model, any part of the wave-packet is subject to inter-channel interactions over the same length.

Consequently, a charge fractionalizes when entering the interaction region. It splits into a fast charged mode and a slow neutral mode, made out of two $\oplus$-excitations, and one $\oplus$- and one $\ominus$-excitation respectively. A new subtlety, arising from the abrupt change of velocity at the entering of this region, is that the excitations are deformed. The fast ones are spread while the slow ones are narrowed.

When performing the HBT interferometry, a dependence on l is observed, arising from two antagonistic effects: propagation under inter-channel interactions tends to excite electron-hole pairs, but they anti-bunch with thermal excitations. Thus, starting from some length -depending on the inter-channel interaction strength u-, the HBT noise reaches a steady value. In stark contrast with the infinite interaction region case, this value does not depend on u (or equivalently on the ratio of the fast mode velocity over the slow mode velocity). Finally, in the $l = 0$ limit, one recovers the $\nu = 1$ case for setup 1, and zero noise for setup 2 as no excitation can be created on the inner channel.

The main success of this model is that less coherence is lost in the co-propagating channels, compared to the case where inter-channel interactions span all the sample, reproducing very well experimental data. For large wave-packets, the difference between both theoretical models is all the more important, as the propagation length under these interactions can differ drastically for the tail of the packets. The more energy-resolved the wave-packets, the worse the contrast of the HOM dip. Finally, for realistic parameters the observed interference pattern is a dip, whose width depends crucially on the setup. Indeed, the central and lateral structures are recovered, but as the modes velocities are increased by intra-channel interactions, they melt into the central dips. Thus, the expected side dips lead to a wider central dip, for setup1. For setup 2, depending on the energy resolution of the packet, the dip can be narrowed by the occurrence of side peaks.

7

ZERO TEMPERATURE

We now turn back to the initial $\nu = 2$ model, in which intra-channel interactions are switched off -as they change very little the physics but for higher propagation velocities-, and inter-channel interactions span all the sample. Thus, an electron is fractionalized at its injection time (see fig. 5.4). In addition, we consider the zero temperature limit $\Theta = 0$ which cannot be achieved in practice, but shows interesting peculiarities.

7.1 PRELIMINARIES

The model is the same all over the sample, the Green's functions describing electronic transport are thus homogeneous. Consequently, the results derived in chapter 4 can be used directly. One simply has to substitute the generic Green's functions by the new ones to obtain the desired quantities, such as the incoming or outgoing noise, etc.

7.1.1 *Green's functions*

At zero temperature, the retarded bosonic Green's functions of the eigenmodes are given by:

$$\begin{aligned} G_{\pm R}(t;x) &= -\log\left[1+i(v_\pm t - x)\right] \\ G_{\pm L}(t;x) &= -\log\left[1+i(v_\pm t + x)\right] \end{aligned} \tag{7.1}$$

Let us remind here that t and x are dimensionless, and $v_\pm = v_F \pm u = 1 \pm u$ as there are no intra-channel interactions.

7.1.2 *Normalization*

One has to replace the Green's functions by their expression in eq. (4.29). Performing the substitution $y_L - z_L \to y_L$ and computing the integral over z_L, one is left with:

$$\mathcal{N} = \frac{1}{2\pi}\int dy_L e^{-ik_0 y_L - \Gamma|y_L|}\frac{1}{1-iy_L} \tag{7.2}$$

7.1.3 *Charge fractionalization*

One electronic wave-packet is injected on the outer left-moving channel, at position $x = l$ and time $t = 0$. The charge density average on both channels is obtained from eq. (4.6):

$$\begin{aligned} \langle q_{jL}(x,t)\rangle_{\phi_L} = \frac{1}{\mathcal{N}}\frac{e\Gamma}{2i\pi^2 a}\int dy_L dz_L e^{ik_0(z_L-y_L)}e^{-\Gamma(z_L+y_L)}\theta(y_L)\theta(z_L)\frac{1}{1+i(z_L-y_L)} \\ \left[\left(\frac{1}{i+v_+t+x-z_L-L}-\frac{1}{-i+v_+t+x-y_L-L}\right)\right. \\ \left.+\sigma_j\left(\frac{1}{i+v_-t+x-z_L-L}-\frac{1}{-i+v_-t+x-y_L-L}\right)\right] \end{aligned} \tag{7.3}$$

with $\sigma_j = (-1)^{j+1}$. Actually, this equation can be obtained from its analog at finite temperature, eq. (5.4), by taking the limit $\beta = 1/(k_B\Theta) \to \infty$.

One can already see from eq. (7.3) that both the fast and slow excitations carry the same charge on the outer channel, whereas, on the inner channel, the sign of the slow excitation charge is switched.

As depicted inf fig 5.1 (red curves), the electronic wave-packet on the outer edge differs from the exponential function given by eq. (4.27), at the injection time. This effect is caused by the finite cutoff errors, which are more important for more energy-resolved packets (bottom panel). Interestingly, this shape is also sligthly different from the one obtained at finite temperature, $\Theta = 0.1$K.

The phenomenology of charge fractionalization is exactly the same as in the finite temperature case (see section 5.1.3). During propagation, the charge fractionalizes into a fast charged mode and a slow neutral mode, which travel at velocities v_+ and v_- respectively. The fast mode is composed of two $\oplus$-excitations, one on each channel, whereas the slow mode is composed of one $\oplus$-excitation on the outer channel and one $\ominus$-excitation on the inner channel. No charge is transfered between co-propagating channels, as the total charge remains e on the outer channel, and zero on the inner one.

The higher the interaction strength u, the faster the charge mode, and the slower the neutral mode. So the stronger the interaction is, the quicker the two modes split (see fig. 7.1).

7.1.4 *Incoming noise*

Once again, $\mathcal{I}_1$ and $\mathcal{I}_2$, given by eq. (4.37), have to be computed first, in order to obtain the incoming noise.

$$\begin{aligned}\mathcal{I}_j(y_L,z_L) = \frac{1}{2}\int dt\,\partial_x\Big\{ & v_+\Big[\log\left(1+i(-v_+t+z_L+L-x)\right) \\ & -\log\left(1+i(v_+t+x-y_L-L)\right)\Big] \\ + \sigma_j\ & v_-\Big[\log\left(1+i(-v_-t+z_L+L-x)\right) \\ & -\log\left(1+i(v_-t+x-y_L-L)\right)\Big]\Big\} \end{aligned} \tag{7.4}$$

with $\sigma_1 = 1$ and $\sigma_2 = -1$. When performing the substitutions $v_+t \to t$ and $v_-t \to t$ in the first and second terms of the sum respectively, the two contributions add up in the expression for $\mathcal{I}_1$ and one is left with: $\mathcal{I}_1 = 2i\pi$. On the contrary, for $\mathcal{I}_2$, the two terms cancel each other and finally $\mathcal{I}_2 = 0$. As, both $\mathcal{I}_j$ do not depend on y_L and z_L, one directly has that the incoming noises are zero: $S^{LL}_{ij} = 0$.

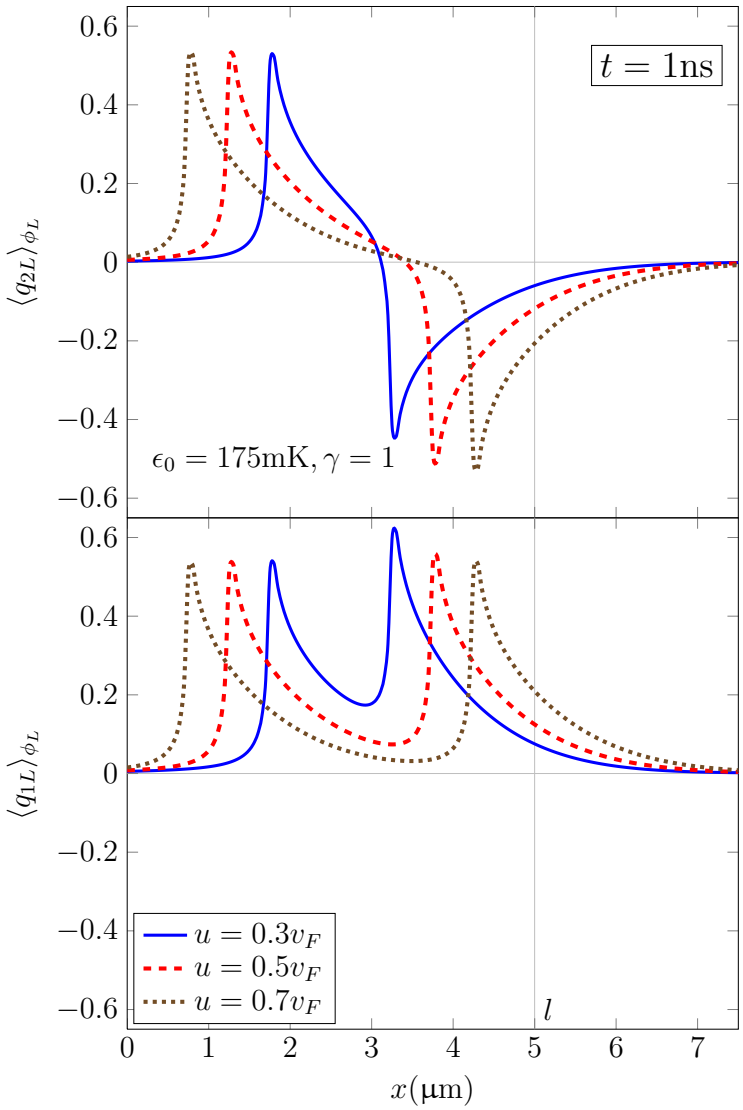

Figure 7.1: Charge density on the outer (bottom panel) and inner (top panel) left-moving channels, after a propagation time $t = 1\text{ns}$, for wide packets in energy, and for different interaction strengths u. The injection position is $l = 5\mu\text{m}$. As the interaction strength between co-propagating channels is increased, the fast excitations travel faster and the slow ones travel slower, leading to an increased spatial splitting between the modes.

7.2 HANBURY BROWN AND TWISS EXPERIMENT

As the incoming noises are zero, only the mixed term contributes to the HBT noise: $S_{\mathrm{HBT}} = (ev_F)^2 \mathcal{R}\mathcal{T}\mathcal{M}$. The mixed term is given by eq. (4.48), in which appear $\mathcal{A}_{\pm L}(-t,-t';z_L+L)$ and $-\mathcal{A}^*_{\pm L}(-t,-t';y_L+L)$, directly computed from their definitions, eq. (4.45). We finally make the substitutions $t \to t+\tau$ and $t' \to t$, and recover eq. (5.8), for setup s , with:

$$g(t,x) = \left[\frac{1}{1+i(v_+t+x)}\frac{1}{1+i(v_-t+x)}\right]^{1/2} \tag{7.5}$$

$$h_s(t;x,y) = \left[\frac{1+i(v_+t-x)}{1-i(v_+t-y)}\right]^{1/2}\left[\frac{1+i(v_-t-x)}{1-i(v_-t-y)}\right]^{3/2-s} \tag{7.6}$$

As obtained at finite temperature, in both the finite and infinite interaction region models, the modulus of the noise increases with the interaction strength u and the energy resolution γ of the packet. This increase is due to the rising number of electron-hole pairs created during the relaxation process of the wave-packet. They are more numerous for a higher interaction strength, as the modes get further apart, and for a more energy-resolved packet as there is more room for it to decohere. As depicted in fig. 7.2, the noise (in absolute value) is higher for energy-resolved wave-packets (top panel) and for greater values of u.

While the eigenmodes are dragged apart when l rises, the number of particle-hole pairs increases and finally diverges as $\log l$ at zero temperature [54], leading to the same divergence in the noise. This $\log l$ divergence of S_{HBT} is a peculiarity of the zero-temperature case. Indeed, at finite temperature, thermal excitations anti-bunch with the low energy particle-hole pairs the wave-packet has collapsed onto during propagation, thus reducing the noise. A steady value is reached, at a length depending on the size of the interaction region and on the inter-channel interaction strength (see fig. 5.3 and 6.5). Here, S_{HBT} is not regularized by the temperature and the low energy excitations keep on proliferating, leading to an infinite noise for $l \to \infty$.

Furthermore, as shown by the logarithmic fits in fig. 7.2 (dotted curves), this log divergence is faster for a stronger interaction. Interestingly enough, the divergence rate of S_{HBT} is independent of the injection parameters. It is only fixed by u.

Finally, the logarithmic behavior of the noise is the same for both setups. Like in the finite temperature cases, the noise depends on the considered

setup for small values of l only, and it is smaller (or equal) for setup 2 than for setup 1, at $l = 0$.

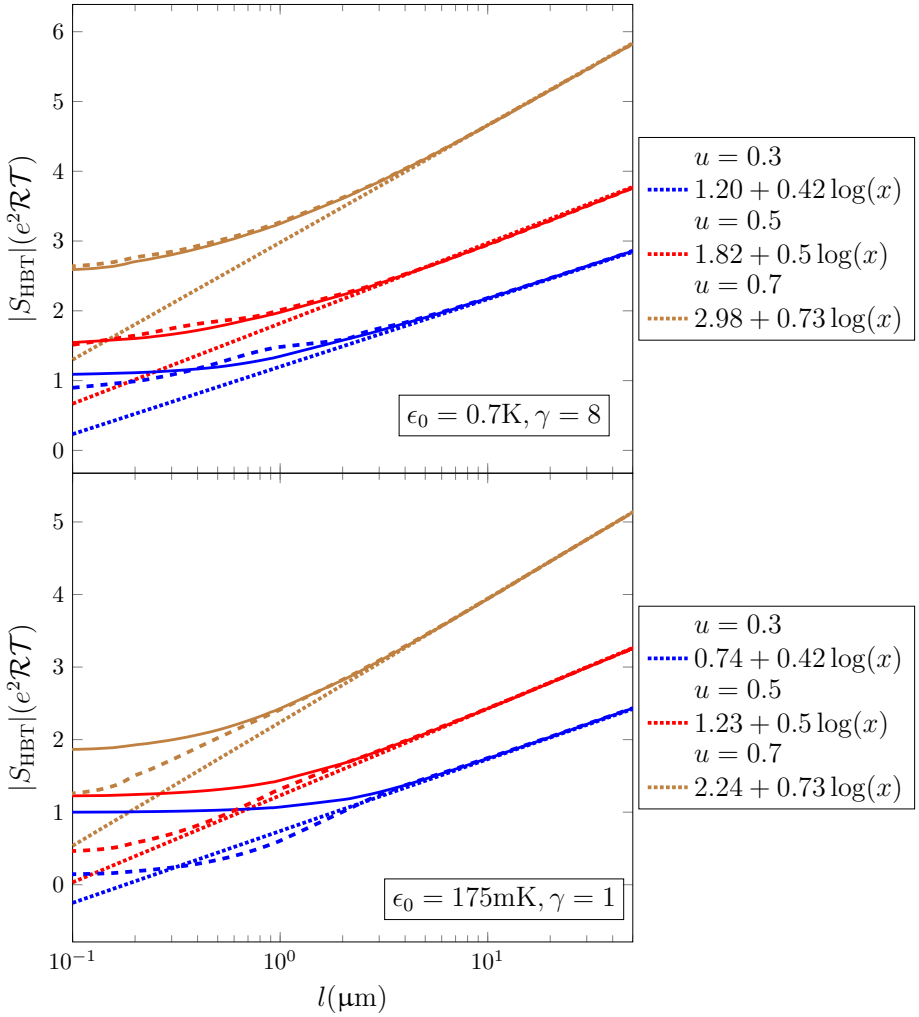

Figure 7.2: Plots of the HBT noise at zero temperature as a function of the propagation length l, for energy-resolved (top panel) and large in energy (bottom panel) exponential wave-packets, for the interaction strengths $u = 0.3v_F, 0.5v_F, 0.7v_F$. The plain curves stand for setup 1, the dashed ones for setup 2, and the dotted ones for the logarithmic fits. The log fits show the divergence of S_{HBT} when $l \to \infty$. The divergence is faster for a higher interaction strength, and does not depend on the parameters of the packets.

7.3 HONG-OU-MANDEL EXPERIMENT

The phenomenology of charge fractionalization is not fundamentally changed at zero temperature, in the sense that an electron still splits into a fast and a slow modes, each made out of two excitations. Thus, the HOM setups give access to many cases of interferometry: the colliding excitations carry the same or opposite charges, and propagate at the same or different velocities. The main difference stems from the missing thermal excitations, and the sharp step of the Fermi distribution. Because of this abruptness at E_F, electron and hole excitations are prevented from overlapping.

As in the finite temperature case, with an infinite interaction region, the HOM noise is given by eq. (5.11), in which the functions g and h_s are defined by eq. (7.5) and (7.6) respectively.

First, the three structure interference pattern of the noise as a function of the time delay is recovered. Away from these structures, S_{HOM} still saturates at twice S_{HBT}, as the incoming excitations are partitioned independently. Here comes the first peculiarity of the HOM interferometry at zero temperature: the dependence on the propagation length of the value of the noise at large δT is never washed out (see fig. 7.4 and 7.5). As l keeps increasing, it diverges as $\log l$, as a consequence of the log divergence of S_{HBT} (see section 7.2).

In stark contrast to the HBT noise, the bottom of the HOM dip is only weakly l dependent at zero temperature, as shown in fig. 7.3. The net result of this effect, combined with the logarithmic divergence of S_{HBT}, is that the contrast of the central dip $\eta = S_{\mathrm{HOM}}(0)/(2S_{\mathrm{HBT}})$ quickly increases as the propagation length is increased. It can even eventually reach $\eta = 1$ for $l \to \infty$. This rather counter-intuitive result of a unity contrast for infinitely long propagation is an artifact arising from the peculiar $\log l$ divergence of the HBT noise, and as such can be viewed as a consequence of the zero temperature limit.

Moreover, for high enough values of l, both the HBT noise and the bottom of this dip are insensitive to the chosen setup (and thus, to the partitioned channel) signaling that the interference between identical excitations is independent of the charge they carry.

Finally, $S_{\mathrm{HOM}}(0)$ is much lower for large wave-packets in energy than for energy resolved ones, as observed in all previous cases. The contrast sinks with the energy resolution of the wave-packet.

Lateral structures, whose positions scale like l, are also recovered at zero temperature (see fig. 7.4 and 7.5). They probe the interference of excitations with different velocities, both $\oplus$-charged for setup 1, and $\oplus$- and $\ominus$-charged for

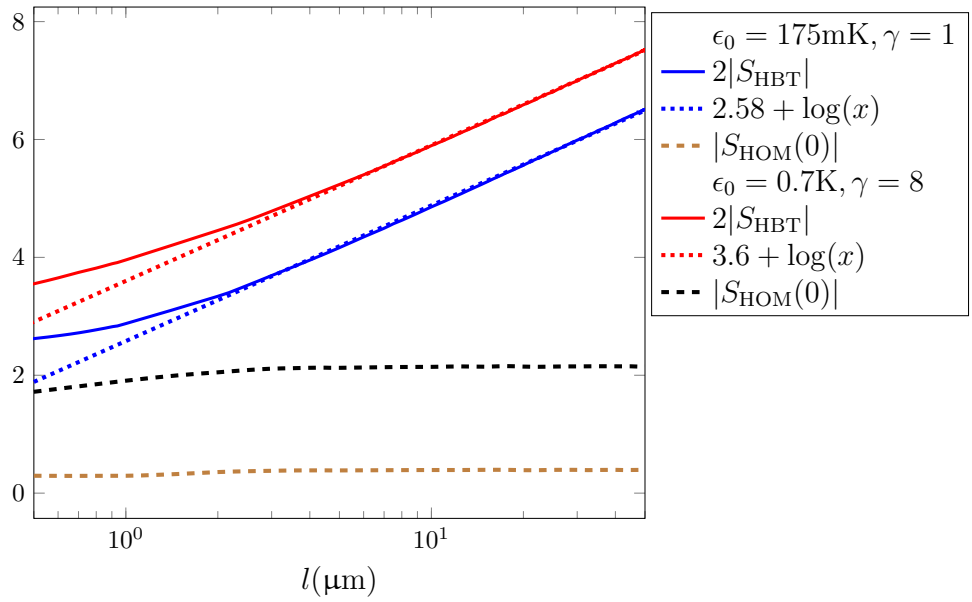

Figure 7.3: Plots of the HBT noise as well as the bottom of the HOM dip at zero temperature as a function of the propagation length l for $u = 0.5v_F$, for a wide packet in energy ($\epsilon_0 = 175mK, \gamma = 1$) and an energy-resolved exponential wave-packet ($\epsilon_0 = 0.7K, \gamma = 8$), for setup 1. The log fits show the divergence of S_{HBT} when $l \to \infty$, while for large enough l, the bottom of the HOM central dip is unchanged when l is increased.

setup 2. The two remaining excitations are partitioned independently at the QPC, and add the contribution S_{HBT} to the noise. Another striking difference with the zero temperature case is that both these scenarii lead to destructive interference.

While lateral dips were expected for setup 1, in agreement with the finite temperature case (see fig. 5.5 and 5.6), the lateral dips obtained as well for setup 2 are surprising. One should recall here electron-hole interferometry case at $\nu = 1$ (section 2.3.2.2). This interference is constructive, producing a peak whose value depends on the overlap of the electron and the hole wave-packets ($\varphi^e(k)\varphi^h(k)^*$), times the Fermi product $f_k(1 - f_k)$. Thus, it is killed at zero temperature. Here, one can guess that constructive interference is forbidden as well by the zero temperature. However, because of inter-channel coupling, both incoming wave-packets have collapsed onto low energy particle-hole pairs, when they reach the QPC. The observed structure is thus a signature of the interference of those pairs. As electrons and holes cannot overlap in energy, electrons anti-bunch with one another, and so do the holes. Consequently the interference is destructive, leading to a dip.

Furthermore, the $\oplus/\ominus$ interference is weaker than the $\oplus/\oplus$ or $\ominus/\ominus$ interference. Indeed, both for the energy-resolved packets and the packets large in energy, the lateral right dip is less deep for setup 2 than for setup 1.

Finally, all these lateral dips are asymmetric as a result of the velocity mismatch between the colliding excitations, as observed at finite temperature (see fig. 5.5 and 5.6).

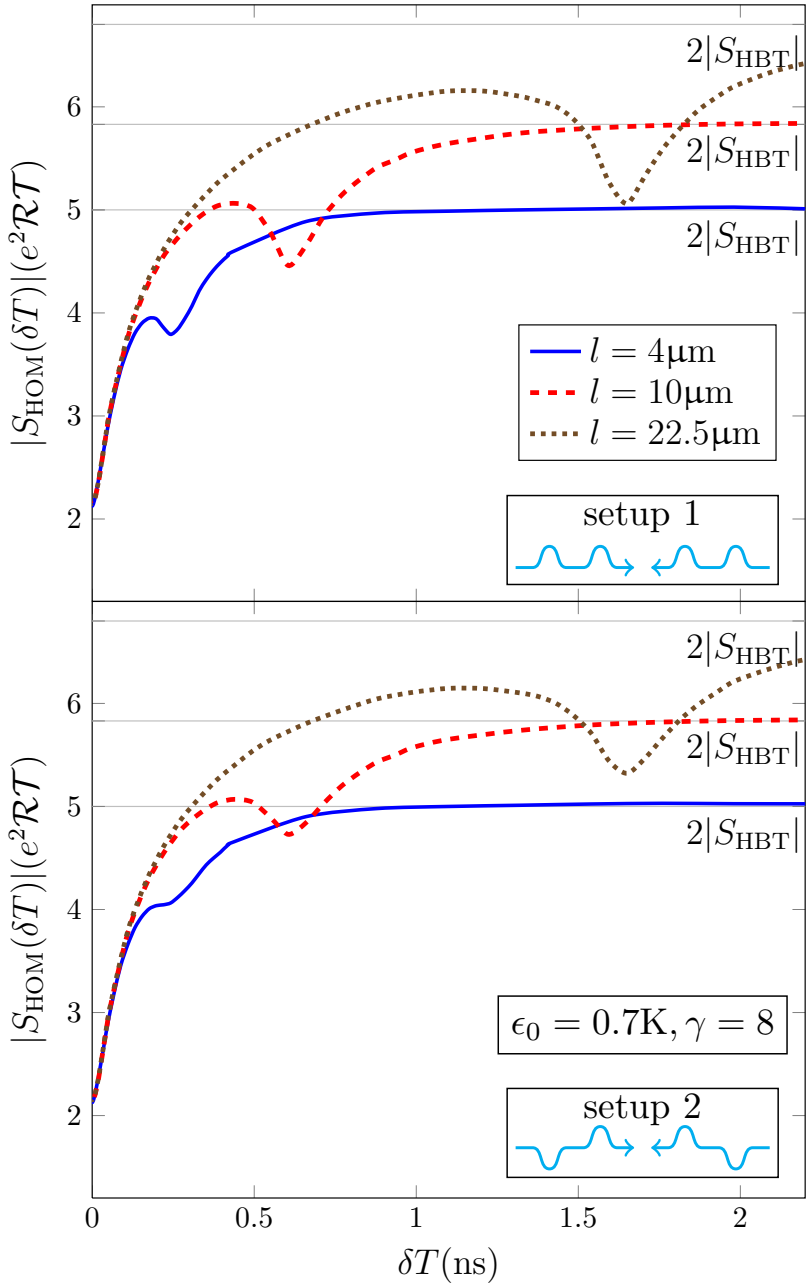

Figure 7.4: Plots of the HOM noise at zero temperature as a function of the time delay δT for energy-resolved wave-packets, and $\delta T \geq 0$ (the figure is symmetric for $\delta T < 0$). The depth of the central dip depends neither on l, nor on the considered setup. For both setups, lateral asymmetric dips are obtained, at a position scaling like l.

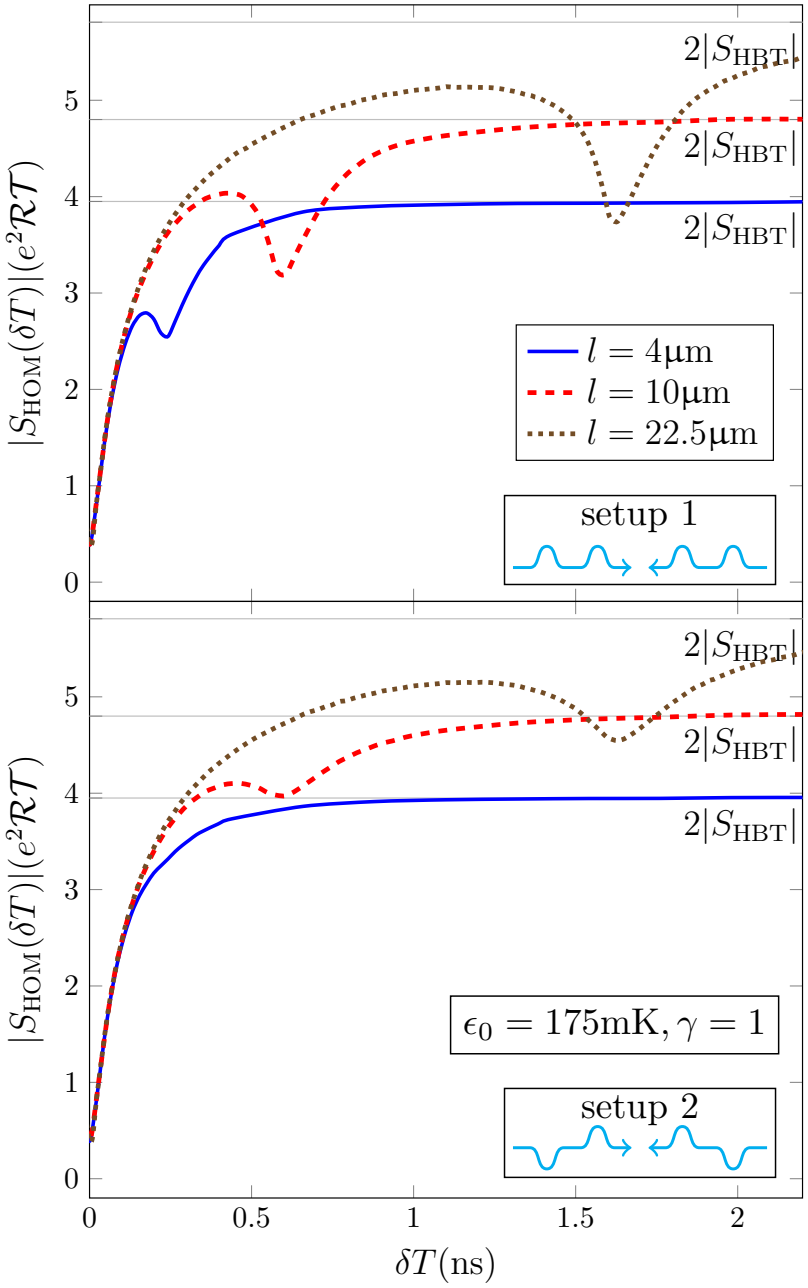

Figure 7.5: Plots of the HOM noise at zero temperature as a function of the time delay δT for wide wave-packets in energy, and $\delta T \geq 0$. The depth of the central dip is l- and setup-independent, and lateral dips are obtained for both setups. The noise is lower than for energy-resolved packets, and the contrast of the central dip is better.

7.4 CONCLUSION

At zero temperature, for an infinite interaction region, the injected electrons are fractionalized like at finite temperature. Only the shape of the excitations is slightly modified. As the fast and slow modes split during propagation, the initial wave-packet relaxes and electron-hole pairs are created near the Fermi energy. The most striking peculiarities stem from the fact that these excitations proliferate as the propagation length l is increased, and their number finally diverges as $\log l$.

As the HBT noise counts the number of excitations partitioned at the QPC it diverges as well logarithmically with l. Contrary to the finite temperature cases, the length dependence is not regularized by temperature, as no excitations are incoming from the conter-propagating arm. The divergence rate increases with the interaction strength, but is insensitive to the packets parameters.

Another peculiarity arising from the zero temperature limit is that the contrast of the HOM central dip increases with l. Indeed, $S_{\mathrm{HOM}}(0)$ quickly becomes independent of l, whereas S_{HBT} diverges, leading to an enhanced contrast.

Three structures are recovered in the HOM noise as the time delay is varied, but three dips are obtained for both setups. This result strongly differs from the previous cases as lateral peaks were obtained for setup 2 previously. This comes from the fact that electrons holes cannot overlap in energy at zero temperature. Thus, the electron-hole pairs incoming from both arms interfere specie by specie: electrons anti-bunch and so do the holes. Consequently, lateral dips are obtained as well for setup 2.

CONCLUSION

8

OUTLOOK

This thesis is a contribution to the very new field of electron quantum optics, in which parallels are made between electron flow and photon beams in quantum optics. In addition, the wave-like character of electrons is fully taken into account in order to probe their interferometry at the mesoscopic scale.

The emergence of electron quantum optics has been motivated by a recent experimental breakthrough: single electron sources are now available. They allow to push forward the parallel between electronic and photonic transport, until the single particle scale. One can thus investigate on the coherence of a single electron wave-packet, and the decoherence phenomena occurring because of its interactions with the environment.

Furthermore, in order to mimic the propagation of light through vacuum, electrons wave guides consisting of quantum edge channels of the IQHE are used. This system bears the advantage that electrons propagate ballistically, with an enhanced coherence length, and suffer very weak backscattering. In this context, we have been focusing on two famous quantum optics setups, transposed to electrons, which shed light upon the importance of many-body correlations in electron interferometry.

8.1 SUMMARY

The single electron emission process is very well understood using a non-interacting theory, which takes advantage of the time periodicity of the source. A single electron, followed half a period later by a single hole, is injected with an exponential shape in real space -or equivalently, a Lorentzian shape in energy space. Both the injection energy and the width of the electronic wave-packet are tuned by adjusting appropriately gate voltages. The path followed by the one-dimensional quantum Hall edge states, along which the particles propagate ballistically, is adjusted by depleting the 2DEG. When the constriction between the two edges of the sample is narrow enough, backscattering between counter-propagating channels is enabled, allowing for the collision of two electrons or of one electron and one hole.

In the non-interacting frame, two electrons emitted exactly in the same way (same injection energies and widths) are perfectly indistinguishable. Thus, when they collide, the Pauli principle forces them to anti-bunch. As they exit in the opposite outgoing channels from the QPC, the random character of partitioning is lost, and the excess current correlations fall down to zero. The maximum contrast obtained for a dip going to zero is a direct consequence of the perfect degree of indistinguishability between the interfering electrons.

If the energy widths of the colliding fermions are detuned, the degree of indistinguishability is reduced, and so is the contrast of the Pauli dip. Such asymmetric injections are realized in practice by tuning the gate voltages of the emitters QPCs in a different way on both edges.

Not only can the degree of indistinguishability of the colliding excitations be extracted from the Pauli dip depth, but additional information about the wave-packets are gained. Indeed, exponential wave-packets produce an exponential dip, whose decay rate is proportional to the energy width of the packets. In case of asymmetric injections, each side of the dip is governed by the width of one wave-packet. Thus, an asymmetric dip is obtained when wave-packets with no mirror symmetry are injected.

The collision of one electron and its symmetric hole, at the location of the QPC, is also considered. Such interferences are constructive, as they produce a peak, which strongly depends on the temperature. In fact, it is killed at zero temperature. The peak is enhanced by increasing the temperature, and also by tuning the excitation voltage drives of the capacitors so that the the particles are emitted near the Fermi energy.

A Pauli dip has indeed been measured as a signature of electron-electron collision. However, this dip does not reach zero, signaling that the degree of indistinguishability is not maximal. The main difference between the previous theoretical results and the experiment is that this latter is performed at filling factor $\nu = 2$. In this regime, electronic transport occurs along two

co-propagating channels on each edge. These edge states are very close by and, consequently, a strong Coulomb repulsion is experienced between the co-propagating charge fluctuations. Using the TLL theory, one can show that these interactions dramatically influence the nature of electronic propagation, leading to charge fractionalization.

Indeed, strong coupling between the co-propagating channels makes an injected electron fractionalize into a fast and a slow mode, each made out of two excitations, propagating with different velocities. On the outer channel, both excitations carry the charge $\oplus$, whereas the fast one is $\oplus$-charged and the slow one is $\ominus$-charged on the inner channel. In the HBT experiment, two such excitations interfere with the FS incoming from the counter-propagating branch. In the HOM experiment, two symmetric sets of excitations interfere with one another. Depending on whether the outer or the inner channel is partitioned, the slow excitation is $\oplus$- or $\ominus$-charged.

At finite temperature, as the wave-packet propagates, it collapses onto low energy electron-hole pairs, whose number is counted by the HBT noise. But this latter is reduced because of anti-bunching with thermal excitations. The intensity of this effect depends on the initial wave-packet energy contents, as the more it overlaps with the FS, the stronger the anti-bunching. In this sense, the finite temperature acts as a low energy cutoff: since the energy range near the Fermi energy is already partially occupied, the electron-hole pairs created during relaxation are prevented from proliferating. Consequently, after some time, the propagation length dependence of the noise is lost. Moreover, the final value of the HBT noise does not depend on the considered setup: the partition noise made by a $\oplus$- and a $\ominus$-excitation is the same.

The main result of chapter 5 is the sensible loss of contrast of the HOM central dip, as observed in the experiment. This reduction effect strongly depends on the energy resolution of the emitted packets and is directly related to decoherence. The higher and the thiner a wave-packet is in energy, the more it has room to decohere. Consequently, a lot of information is lost in the co-propagating channel and the packet is very distinguishable from its symmetric counterpart.

Moreover, fast and slow modes interfere with each other, constructively or destructively, depending on the charge carried by the colliding excitations. Two fast and slow excitations with the same (opposite) charge lead to a small asymmetric dip (peak). These side structures are small because of the reduced degree of indistinguishability between two such excitations, as they propagate with different velocities. The asymmetry is caused by the velocity mismatch, and is reminiscent of the asymmetry obtained for packets with different widths. Furthermore, the lateral dips or peaks positions scale like the propagation length l.

Next, we have considered a quantum Hall bar at filling factor $\nu = 2$, with intra-channel interactions, proven to be consequent in the experiment. Also, inter-channel interactions are switched on in a region ranging from $-l$ to l only. In this model, any part of the wave-packet is subject to inter-channel

interactions over the same length l, whereas previously its tail was interacting over a much longer length, depending on the width of the packet. Consequently, a charge fractionalizes at the entrance the interaction region, and splits into a fast charged mode and a slow neutral mode. A new subtlety, arising from the abrupt change of velocity at the entering of this region, is that the shape of the excitations is modified: the fast ones are spread while the slow ones are narrowed.

When performing the HBT interferometry, a dependence on the interaction region length is observed, arising from same opposing effects as previously. Inter-channel interactions make the initial wave-packet collapse onto electron-hole pairs, but those anti-bunch with thermal excitations. Thus the HBT noise reaches again a steady value. In stark contrast with the infinite interaction region case, this value does not depend on the inter-channel interaction strength. Finally, in the $l = 0$ limit, inter-channel interactions are missing, and one recovers the $\nu = 1$ case.

The main success of this model is that less coherence is lost in the co-propagating channels, compared to the case where inter-channel interactions span all the sample, reproducing very well experimental data. For large wave-packets, the difference between both theoretical models is all the more important, as the propagation length under these interactions can differ drastically for the tail of the packets. The more energy-resolved the wave-packets, the worse the contrast of the HOM dip. Finally, for realistic parameters the side structures in the interference pattern melt into the central dip. Thus, depending on the occurrence of lateral dips or peaks, the central dip is widened or narrowed.

At zero temperature, for an infinite interaction region, the injected electrons are fractionalized like at finite temperature, with a slightly different shape. As the fast and slow modes split during propagation, the initial wave-packet relaxes and electron-hole pairs are created near the Fermi energy. But these excitations proliferate as the propagation length l is increased, and their number finally diverges as $\log l$.

As the HBT noise counts the number of excitations partitioned at the QPC, it diverges as well logarithmically with l. Unlike the finite temperature cases, no low energy cutoff regularizes the propagation length dependence. The divergence rate increases with the interaction strength, but is insensitive to the packets parameters.

Consequently, the contrast of the HOM central dip increases with l. Indeed, $S_{\mathrm{HOM}}(0)$ quickly remains independent of l, whereas S_{HBT} diverges, leading to an enhanced contrast.

No matter the charges of the interfering excitations, three dips are obtained in the HOM noise as the time delay is varied. This result strongly differs from the previous cases as oppositely charged excitations lead to constructive interference, at finite temperature. It is due to the fact that electrons and holes cannot overlap in energy at zero temperature. Thus, electrons anti-bunch with one another and so do the holes.

Finally, one should note the relevance of the described dependencies from a practical point of view. Indeed, the predicted behavior as l is varied could be checked if lateral gates were added to the setup, modifying the propagation path before the QPC. Measurements with different injection energies and packets widths are already being processed.

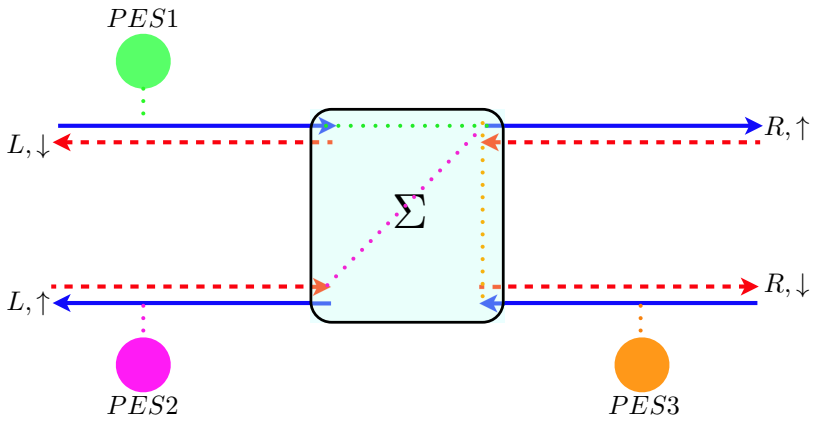

Figure 8.1: Schematic view of a quantum spin Hall bar. Electrons with opposite spin counter-propagate along each edge. Incoming and outgoing channels are connected through a scattering region Σ (shaded yellow square), typically given by a QPC. PESs are placed along the various edges of the sample: PES1 (green) inject excitations in the $(R\uparrow)$ incoming and $(L\downarrow)$ outgoing channels, PES2 (magenta) in the $(R\downarrow)$ incoming and $(L\uparrow)$ outgoing channels and PESS3 (orange) in the $(L\uparrow)$ incoming and $(R\downarrow)$ outgoing channels.

8.2 PERSPECTIVES

8.2.1 *HOM interferometry in a quantum spin Hall bar*

In the last years new states of matter showing a topological structure similar to the one of the IQHE, but in absence of magnetic field, have been realized. In particular the two dimensional realization of these topological insulators is given by the quantum spin Hall effect (QSHE) [38, 80], theoretically predicted and experimentally observed in CdTe/HgTe quantum wells [13, 44] and more recently also in similar structure realized with InAs/GaSb [60, 46, 26]. Because of the strong spin-orbit coupling, electrons with opposite spin propagate in opposite directions along the boundaries of the sample (see fig. 8.1).

The existence of topologically protected helical edge states [25] in the QSHE naturally brings out the question about the possibility to take advantage of their peculiar spin-momentum locking properties, in an electron quantum optics perspective. The analog of the mesoscopic capacitor in such a sample is called a PES, since at each driving period a pair of electrons (holes) with opposite spin orientation is injected into the helical channels. In particular the HOM interferometry brings out a rich phenomenology related to the helicity of the edge channels.

As a first example of HOM interferometry experiments, we can consider the injection of electrons into the $(R,\uparrow)$ and $(L,\uparrow)$ incoming channels. This is realized in the setup of fig. 8.1 when PES1 (green) and PES3 (orange) are on,

while PES2 (magenta) is off. Because we are dealing with electrons with the same spin, this kind of process can be considered as the direct transposition in the QSHE framework of the IQHE case without interaction. Indeed, a dip appears in the noise when the electrons reach the QPC with a delay comparable with the typical extension in time of the wave-packet. This Pauli dip is a consequence of the fermionic statistics of the electron. However, in the case considered here, the amplitude of the dip is reduced compared to the $\nu = 1$ case. This reduced visibility can be interpreted as a direct consequence of the additional channels which are coupled at the QPC. Indeed, more channels for the electrons to scatter into means an increased noise associated with partitioning at the QPC. This increase generally cannot be compensated for by the noise reduction related to the Pauli principle through the HOM contribution, ultimately leading to a reduced dip. This effect can be negligible, with a visibility one, or conversely very relevant, with a zero visibility, and crucially depends on the parameters of the scattering region. In the absence of spin flipping, we recover the result of the IQHE as a consequence of the complete decoupling of the system into two $\nu = 1$-like states with opposite spin orientations.

Due to the helical properties of the edge states, new two-electron interference processes are possible involving particles with opposite spin. This can be achieved with electrons of the same or opposite chirality. Remarkably enough, it leads again to HOM dips. This is not due to the Pauli principle, but to the constraints imposed by time-reversal symmetry (TRS) [28]. The depth of this dip, called $\mathbb{Z}_2$ dip, depends of the involved channels as well as the QPC configuration.

Let us consider finally another configuration which is unique to the QSHE and which can be seen as the electron quantum optics translation of three-photon HOM experiments. Here, all the PESs of fig. 8.1 are switched on, with possible relative delays in the emissions. Note that, for synchronized injections on the three channels, one has a dip reaching down to zero, independently of the characteristics of the QPC. This total suppression of the noise is a very remarkable feature of helical systems and generalizes both the Pauli dip and the $\mathbb{Z}_2$ dip structure. It depends on the extremely peculiar interplay between the fermionic statistics and the TRS in the helical edge states.

For non synchronized injections one obtains an extremely rich phenomenology depending on the QPC microscopic parameters.

8.2.2 *Adding interactions*

Another perspective naturally arising from the previously presented one (section 8.2.1) is to take interactions into account in the QSHE. Indeed, like at filling factor two, the counter-propagating channels on each edge are so close by that Coulomb repulsion must not be negligible. One could thus imagine repeating the task accomplished in this thesis for the IQHE at $\nu = 2$, by including a local capacitive coupling between these edge states. However, a

considerable effort is required as new difficulties will be arising due to the counter-propagating nature of the channels.

Turning back to the IQHE at filling factor two, interactions could be added between the coupled channels at the QPC. This is relevant as backscattering is enabled by the proximity of both edges, which thus enhances Coulomb repulsion. The difficulties encountered will be rough due to the counter-propagating character of the connected channels.

Finally, HOM interferometry could also be performed in the FQHE, in which the collective charge excitations bear fractional charge and statistics. In the weak backscattering regime, these fractional excitations can be partitioned at a QPC, allowing to implement electron quantum optics setups.

From an experimental point of view, the first challenge would be to inject single quasi-particles in an edge state. Instead of the mesoscopic capacitor described in section 2.1.1, an antidot (a hole in the 2DEG) [63] placed in the vicinity of an edge could be used. First, this setup will allow single quasi-particle transfer from the antidot to the edge through a weakly pinched QPC, second, the quasi-particle population of the antidot can be adjusted using metallic gates. A voltage pulse applied to such gates will trigger the injection of quasi-particles.

The single quasi-particle emission process could be modeled using the chiral Luttinger liquid theory to describe the fractional edge excitations. A rigorous description of the antidot [18, 69, 68] requires to take into account the zero modes associated with its finite size [34]. Current and noise would be first computed in the weak coupling limit, at small quasi-particle emission rate compared to the temperature, using a master equation approach for an arbitrary drive: single shot injection (gate voltage pulse) as well as with an AC gate voltage.

As these quasi-particles exist above a vacuum which is not a simple FS, but a complex highly correlated state, the partition noise will certainly have different properties compared to the one obtained for electron partitioning in the IQHE. For the HOM interferometry, while one can expect to observe a dip in the cross-correlation signal when the two quasi-particles arrive simultaneously at the QPC, the contrast and the width of this dip are probably non-trivial, and may depend in a unique way on the quasi-particle properties, on the filling factor of the system, on the temperature, etc.

Part IV

APPENDIX

A

CONVERSION FROM OUR SYSTEM OF ARBITRARY UNITS TO REALITY

In this thesis, when studying setups in the IQHE at filling facto two, calculations are performed with dimensionless parameters (see remark in section 4.3.2). The purpose is to get rid of the cutoff a, and the Fermi velocity v_F, so as to ease the reading. But one has to turn back to real units to interpret the results.

A.1 CONVERSION

The system of arbitrary units we use is consistent, in the sense that one unit (the energy unit $\delta\epsilon$ for example) can be set, and all other units will scale with that value. The conversion is based on experimental values [16].

THE ENERGY UNIT is obtained using the injection energy, known to be $\epsilon_0 = 0.7\text{K}$. Arbitrarily, we choose it to be two in our units: $\epsilon_0 = 2\delta\epsilon$, with $\delta\epsilon$ the energy unit. One immediately has: $\delta\epsilon = 0.35\text{K}$.

THE TIME UNIT δt is easily obtained from the energy unit: $\delta t = \hbar/(k_B\delta\epsilon) = 22\text{ps}$.

THE SPATIAL UNIT δx is also very easily derived, as $\delta x = v\delta t$, with $v = v_F + U$ the propagation velocity without inter-channel coupling. However, depending on whether intra-channel interactions are on or off, the spatial unit is changed in quite a dramatic way. Let us explicit a few cases:

- Without intra-channel interactions: $U = 0$ and $v_F = 2.5\ 10^4\text{m.s}^{-1}$, yielding $\delta x = 0.5\mu\text{m}$.

- With intra-channel interactions such that $w_+ = 2w_-$. The slow mode velocity has been measured to be $w_- = 4.6\ 10^4 \mathrm{m.s}^{-1}$, leading to $v = 6.9\ 10^4 \mathrm{m.s}^{-1}$, and $\delta x = 1.5\mu\mathrm{m}$.
- With intra-channel interactions such that $w_+ = 8w_-$, the propagation velocity is $v = 2.07\ 10^5 \mathrm{m.s}^{-1}$, yielding $\delta x = 4.5\mu\mathrm{m}$.

A.2 RELATION BETWEEN ESCAPE TIME AND ENERGY WIDTH

Experimentally, the escape time τ_e of a wave-packet from the capacitor is measured, rather than its width Γ. Both quantities are equivalent, insofar as they are inversely proportional: $\tau_e = \alpha/\Gamma$, with α to be determined. But this relation has to be precisely derived to allow quantitative comparison with experiments.

We make the assumption that our so-called energy-resolved packets ($\epsilon_0 = 0.7\mathrm{K}$ and $\gamma = 8$) correspond to the escape time $\tau_e = 44\mathrm{ps}$ [14]. Thus, we obtain the proportionality factor: $\alpha = \Gamma\tau_e = (\epsilon_0/\gamma)\tau_e = 3.9\mathrm{ps.K}$.

[6] C. Altimiras, H. le Sueur, U. Gennser, A. Cavanna., D. Mailly, and F. Pierre. Non-equilibrium edge channel spectroscopy in the integer quantum hall regime. *Nat. Phys.*, 6:34, 2009.

[7] M. Büttiker. Scattering theory of current and intensity noise correlations in conductors and wave guides. *Phys. Rev. B*, 46:12485, 1992.

[8] M. Büttiker. Scattering theory of thermal and excess noise in open conductors. *Phys. Rev. Lett.*, 65:2901, 1990.

[9] M. Büttiker. Quantized transmission of a saddle-point constriction. *Phys. Rev. B*, 41:7906, 1990.

[10] M. Büttiker. Absence of backscattering in the quantum hall effect in multiprobe conductors. *Phys. Rev. B*, 38:9375, 1988.

[11] M. Büttiker, Y. Imry, R. Landauer, and S. Pinhas. Generalized many-channel conductance formula with application to small rings. *Phys. Rev. B*, 31:6207, 1985.

[12] E. Berg, Y. Oreg, E.-A. Kim, and F. von Oppen. Fractional charges on an integer quantum hall edge. *Phys. Rev. Lett.*, 102:236402, 2009.

[13] B. A. Bernevig, T. L. Hughes, and S. C. Zhang. Quantum spin hall effect and topological phase transition in hgte quantum wells. *Science*, 314:1757, 2006.

[14] E. Bocquillon. *Electronic quantum optics in quantum Hall edge channels*. PhD thesis, Université Paris VI, 2012.

[15] E. Bocquillon, V. Freulon, J.-M Berroir, P. Degiovanni, B. Plaçais, A. Cavanna, Y. Jin, and G. Fève. Coherence and indistinguishability of single electron wavepackets emitted by independent sources. *Science*, 339(6123):1054–1057, 2013.

[16] E. Bocquillon, V. Freulon, J.-M. Berroir, P. Degiovanni, B. Plaçais, A. Cavanna, Y. Jin, and G. Fève. Separation between neutral and charge modes in one dimensional chiral edge channels. *Nat. Comm.*, 4:1839, 2013.

[17] E. Bocquillon, F.D. Parmentier, C. Grenier, J.-M. Berroir, P. Degiovanni, D.C. Glattli, B. Plaçais, A. Cavanna, Y. Jin, and G. Fève. Electron quantum optics : partitioning electrons one by one. *Phys. Rev. Lett.*, 108:196803, 2012.

[18] A. Braggio, N. Magnoli, M. Merlo, and M. Sassetti. Signatures of fractional hall quasiparticles in moments of current through an antidot. *Phys. Rev. B*, 74:041304(R), 2006.

[19] H. E. van den Brom and J. M. van Ruitenbeek. Quantum suppression of shot noise in atom-size metallic contacts. *Phys. Rev. Lett.*, 82:1526, 1999.

[20] O. Cosme, S. Pádua, Bovino, A. Fabio, A. Mazzei, F. Sciarrino, and F. De Martini. Hong-Ou-Mandel interferometer with one and two photon pairs. *Phys. Rev. A*, 77(5):053822, May 2008.

[21] D. Coster and R. de L. Kronig. New type of auger effect and its influence on the x-ray spectrum. *Physica*, 2:13, 1935.

[22] E. H. Lieb D.C. Mattis. Exact solution of a many-fermion system and its associated boson field. *J. Math. Phys.*, 6:304, 1965.

[23] P. Degiovanni, Ch. Grenier, and G. Fève. Decoherence and relaxation of single-electron excitations in quantum hall edge channels. *Phys. Rev. B*, 80:241307, 2009.

[24] P. Degiovanni, Ch. Grenier, G. Fève, C. Altimiras, H. le Sueur, and F. Pierre. Plasmon scattering approach to energy exchange and high-frequency noise in ν=2 quantum hall edge channels. *Phys. Rev. B*, 81(12):121302, March 2010.

[25] G. Dolcetto, S. Barbarino, D. Ferraro, N. Magnoli, and M. Sassetti. Tunneling between helical edge states through extended contacts. *Phys. Rev. B*, 85:195138, 2012.

[26] L. Du, I. Knez, G. Sullivan, and R.-R. Du. Observation of quantum spin hall states in inas/gasb bilayers under broken time-reversal symmetry. arXiv:1306.1925v1, 2013.

[27] J. Dubois, T. Jullien, C. Grenier. Degiovanni, P. Roulleau, and D. C. Glattli. Integer and fractional charge lorentzian voltage pulses analyzed in the framework of photon-assisted shot noise. *Phys. Rev. B*, 88:085301, 2013.

[28] J. M. Edge, J. Li, P. Delplace, and M. Büttiker. $\mathbb{Z}_2$ peak of noise correlations in a quantum spin hall insulator. *Phys. Rev. Lett.*, 110:246601, 2013.

[29] G. Fève, P. Degiovanni, and Th. Jolicoeur. Quantum detection of electronic flying qubits. *Phys. Rev. B*, 77:035308, 2008.

[30] G. Fève, A. Mahé, J.-M. Berroir, T. Kontos, B. Plaçais, D. C. Glatti, A. Cavanna, B. Etienne, and Y. Jin. An on-demand coherent single-electron source. *Science*, 316:196404, 2007.

[31] S. Feng. *Mesoscopic Phenomena in Solids*. Elsevier, 1991.

[32] M. P. A. Fisher. and I. Glazman. *Mesoscopic Electron Transport*. NATO ASI Series E, 1996.

[33] L. Geerligs, V. Anderegg, and P. Holweg. Frequency-locked turnstile device for single electrons. *Phys. Rev. Lett.*, 64:2691, 1990.

[34] M R Geller and D Loss. Aharonov-bohm effect in the chiral luttinger liquid. *Phys. Rev. B*, 56:9692, 1997.

[35] S.P. Giblin, M. Kataoka, J.D. Fletcher, P. See, T.J.B.M. Janssen, J.P. Griffiths, G.A.C. Jones, I. Farrer, and D.A. Ritchie. Towards a quantum representation of the ampere using single electron pumps. *Nat. Comm.*, 3:930, 2012.

[36] C. Grenier, R. Hervé, E. Bocquillon, F.D. Parmentier, B. Plaçais, J.-M. Berroir, G. Fève, and P. Degiovanni. Single electron quantum tomography in quantum hall edge channels. *New J. of Phys.*, 13:093007, 2011.

[37] F. D. M. Haldane. Luttinger liquid theory of one-dimensional quantum fluids. i. properties of the luttinger model and their extension to the general 1d interacting spinless fermi gas. *J. Phys. C*, 14:2585, 1981.

[38] M. Z. Hasan and C. L. Kane. Colloquium: Topological insulators. *Rev. Mod. Phys.*, 82:3045, 2010.

[39] S. Hermelin, S. Takada, M. Yamamoto, S. Tarucha, A. D. Wieck, L. Saminadayar, C. Bäuerle, and T. Meunier. Electrons surfing on a sound wave as a platform for quantum optics with flying electrons. *Nature*, 477:435–438, 2011.

[40] C. K. Hong, Z. Y. Ou, and L. Mandel. Measurement of subpicosecond time intervals between two photons by interference. *Phys. Rev. Lett.*, 59(18):2044–2046, November 1987.

[41] A. K. Jha, M. N. O'Sullivan, K. W. C. Chan, and R. W. Boyd. Temporal coherence and indistinguishability in two-photon interference effects. *Phys. Rev. A*, 77(2):021801, February 2008.

[42] J. B. Johnson. Thermal agitation of electricity in conductors. *Phys. Rev.*, 32:97, 1928.

[43] T. Jonckheere, T. Stoll, J. Rech, and T. Martin. Real-time simulation of finite-frequency noise from a single-electron emitter. *Phys. Rev. B*, 85:045321, 2012.

[44] M. König, S. Wiedmann, C. Brüne, A. Roth, H. Buhmann, L. W. Molenkamp, X.-L. Qi, and S.-C. Zhang. Quantum spin hall insulator state in hgte quantum wells. *Science*, 318:766, 2007.

[45] K. von Klitzing, G. Dorda, and M. Pepper. New method for high-accuracy determination of the fine-structure constant based on quantized hall resistance. *Phys. Rev. Lett.*, 45:494, 1980.

[46] I. Knez, R.-R. Du, and G. Sullivan. Evidence for helical edge modes in inverted inas/gasb quantum wells. *Phys. Rev. Lett.*, 107:136603, 2011.

[47] S. Kogan. *Electronic Noise and Fluctuations in Solids*. Cambridge University Press, 1996.

[48] D. L. Kovrizhin and J. T. Chalker. Equilibration of integer quantum hall edge states. *Phys. Rev. B*, 84:085105, 2011.

[49] D. L. Kovrizhin and J. T. Chalker. Multiparticle interference in electronic mach-zehnder interferometers. *Phys. Rev. B*, 81:155318, 2010.

[50] A. Kumar, L. Saminadayar, D. C. Glattli, Y. Jin, , and B. Etienne. Experimental test of the quantum shot noise reduction theory. *Phys. Rev. Lett.*, 76:2778, 1996.

[51] L. D. Landau. On the theory of the fermi-liquid. *Sov. Phys. JETP*, 8:70, 1959.

[52] L. D. Landau. Theory of fermi-liquids. *Sov. Phys. JETP*, 3:920, 1957.

[53] R. Landauer. Spatial variation of currents and fields due to localized scatterers in metallic conduction. *IBM J. Res. Develop.*, 1:223, 1957.

[54] H. Lee and L.S. Levitov. Orthogonality catastrophe in a mesoscopic conductor due to a time-dependent flux. arXiv:cond-mat/9312013, 1993.

[55] C. Leicht, P. Mirovsky, B. Kaestner, F. Hohls, V. Kashcheyevs, E. V. Kurganova, U. Zeitler, T. Weimann, K. Pierz, and H. W. Schumacher. Generation of energy selective excitations in quantum hall edge states. *Semicond. Sci. Technol.*, 26:055010, May 2011.

[56] G. B. Lesovik. Excess quantum noise in 2d ballistic point contacts. *JETP Lett.*, 49:592, 1989.

[57] I. P. Levkivskyi and E. V. Sukhorukov. Shot-noise thermometry of the quantum hall edge states. *Phys. Rev. Lett.*, 109:246806, 2012.

[58] I. P. Levkivskyi and E. V. Sukhorukov. Dephasing in the electronic mach-zehnder interferometer at filling factor $\nu = 2$. *Phys. Rev. B*, 78:045322, 2008.

[59] Y. P. Li, D. C. Tsui, J. J. Heremans, J. A. Simmons, and G. W. Weimann. Low-frequency noise in transport through quantum point contacts. *Appl. Phys. Lett.*, 57:774, 1990.

[60] C. Liu, T. D. L. Hughes, X.-L. Qi, K. Wang, and Shou-Cheng Zhang. Quantum spin hall effect in inverted type-ii semiconductors. *Phys. Rev. Lett.*, 100:236601, 2008.

[61] A. M. Lunde, S. E. Nigg, and M. Büttiker. Interaction-induced edge channel equilibration. *Phys. Rev. B*, 81:041311, 2010.

[62] J. M. Luttinger. An exactly soluble model of a many fermion system. *J. Math. Phys.*, 4:1154, 1963.

[63] I. J. Maasilta and V. J. Goldman. Tunneling through a coherent "quantum antidot molecule". *Phys. Rev. Lett.*, 84:1776, 2000.

[64] A. Mahé, F. D. Parmentier, E. Bocquillon, J.-M. Berroir, D. C. Glattli, T. Kontos, B. Plaçais, G. Fève, A. Cavanna, and Y. Jin. Current correlations of an on-demand single-electron emitter. *Phys. Rev. B*, 82(20):201309, November 2010.

[65] G. D. Mahan. *Many-Particle Physics*. Plenum Press, 1990.

[66] T. Martin. Noise in mesoscopic physics. In H. Bouchiat, Y. Gefen, S. Guéron, G. Montambaux, and J. Dalibard, editors, *Nanophysics: Coherence and Transport*, Les Houches, Session LXXXI, page 283. Elsevier, 2004.

[67] Th. Martin and R. Landauer. Wave-packet approach to noise in multichannel mesoscopic systems. *Phys. Rev. B*, 45:1742, 1992.

[68] M. Merlo, A. Braggio, N. Magnoli, and M. Sassetti. Current statistics of an antidot in the fractional hall regime. *Physica E*, 40:1282, 2008.

[69] M. Merlo, A. Braggio, N. Magnoli, and M. Sassetti. Transport of fractional hall quasiparticles through an antidot. *Phys. Rev. B*, 75:195332, 2007.

[70] M. Milletarì and B. Rosenow. Shot noise signatures of charge fractionalization in the $\nu = 2$ quantum hall edge. arXiv:1207.1719, 2012.

[71] M. Moskalets, P. Samuelsson, and M. Büttiker. Quantized dynamics of a coherent capacitor. *Phys. Rev. Lett.*, 100(8):086601, February 2008.

[72] I. Neder. Fractionalization noise in edge channels of integer quantum hall states. *Phys. Rev. Lett.*, 108:186404, 2012.

[73] I. Neder, M. Heiblum, Y. Levinson, D. Mahalu, and V. Umansky. Unexpected behavior in a two-path electron interferometer. *Phys. Rev. Lett.*, 96:016804, 2006.

[74] P. Nozières. *Theory of Interacting Fermi Systems*. W. A. Benjamin Inc., 1964.

[75] H. Nyquist. Thermal agitation of electric charge in conductors. *Phys. Rev.*, 32:110, 1928.

[76] S. Ol'khovskaya, J. Splettstoesser, M. Moskalets, and M. Büttiker. Shot noise of a mesoscopic two-particle collider. *Phys. Rev. Lett.*, 101:166802, 2008.

[77] F. D Parmentier, E. Bocquillon, J. -M Berroir, D. C Glattli, B. Plaçais, G. Fève, M. Albert, C. Flindt, and M. Büttiker. Current noise spectrum of a single particle emitter: theory and experiment. *Phys. Rev. B*, 85:165438, November 2012.

[78] R. B. Patel, A. J. Bennett, K. Cooper, P. Atkinson, C. A. Nicoll, D. A. Ritchie, and A. J. Shields. Quantum interference of electrically generated single photons from a quantum dot. *Nanotechnology*, 21(27):274011, July 2010.

[79] R. de Picciotto, M. Reznikov, M. Heiblum, V. Umansky, G. Bunin, and D. Mahalu. Direct observation of a fractional charge. *Nature*, 389:162, 1997.

[80] X.-L. Qi and S.-C. Zhang. Topological insulators and superconductors. *Rev. Mod. Phys.*, 83:1057, 2011.

[81] M. Reznikov, M. Heiblum, H. Shtrikman, and D. Mahalu. Temporal correlation of electrons: Suppression of shot noise in a ballistic quantum point contact. *Phys. Rev. Lett.*, 75:3340, 1995.

[82] P. Roulleau, F. Portier, D. C. Glattli, P. Roche, A. Cavanna, G. Faini, U. Gennser, and D. Mailly. Finite bias visibility of the electronic mach-zehnder interferometer. *Phys. Rev. B*, 76:161309, 2007.

[83] P. Roulleau, F. Portier, P. Roche, A. Cavanna, G. Faini, U. Gennser, and D. Mailly. Direct measurement of the coherence length of edge states in the integer quantum hall regime. *Phys. Rev. Lett.*, 100:126802, 2008.

[84] M. A. Sagioro, C. Olindo, C. H. Monken, and S. Pádua. Time control of two-photon interference. *Phys. Rev. A*, 69(5):053817, May 2004.

[85] L. Saminadayar, D. C. Glattli, Y. Jin, and B. Etienne. Observation of the $e/3$ fractionally charged laughlin quasiparticle. *Phys. Rev. Lett.*, 79:2526, 1997.

[86] H. J. Schulz. *Mesoscopic Quantum Physics, Les Houches, Session LXI*. Elsevier, 1995.

[87] H. le Sueur, C. Altimiras, U. Gennser, A. Cavanna, D. Mailly, , and F. Pierre. Energy relaxation in the integer quantum hall regime. *Phys. Rev. Lett.*, 105:056803, 2010.

[88] E. V. Sukhorukov and V. V. Cheianov. Resonant dephasing in the electronic mach-zehnder interferometer. *Phys. Rev. Lett.*, 99:156801, 2007.
A. Szafer and A. Douglas Stone. Theory of quantum conduction through a constriction. *Phys. Rev. Lett.*, 62:300, 1989.

[89] S. Tomonaga. Remarks on bloch's method of sound waves applied to many-fermion problems. *Prog. Theor. Phys.*, 5:544, 1950.

[90] M. Vicari, A. Braggio, E. Galleani d'Agliano, and M. Sassetti. Photoconductance of a one-dimensional quantum dot. *Eur. Phys. J. B*, 25:115, 2002.

[91] B. J. van Wees, L. P. Kouwenhoven, H. van Houten, C. W. J. Beenakker, J. E. Mooij, C. T. Foxon, and J. J. Harris. Quantized conductance of magnetoelectric subbands in ballistic point contacts. *Phys. Rev. B*, 38:3625, 1988.

[92] X.G. Wen. Theory of the edge states in fractional quantum hall effects. *Int. J. Mod. Phys. B*, 6:1711, 1992.

[93] D. Yoshioka. *The quantum Hall effect*, volume 133. Springer, 2002.

[94] A. Zavatta, S. Viciani, and M. Bellini. Recurrent fourth-order interference dips and peaks with a comblike two-photon entangled state. *Phys. Rev. A*, 70(2):023806, 2004.